



РОССИЙСКИЙ ГОСУДАРСТВЕННЫЙ ПЕДАГОГИЧЕСКИЙ УНИВЕРСИТЕТ им. А. И. ГЕРЦЕНА
HERZEN STATE PEDAGOGICAL UNIVERSITY of RUSSIA

ISSN 2687-153X

PHYSICS OF COMPLEX SYSTEMS

T. 3 № 4 2022

VOL. 3 No. 4 2022



Herzen State Pedagogical University of Russia

ISSN 2687-153X (online)

physcomsys.ru

<https://www.doi.org/10.33910/2687-153X-2022-3-4>

2022. Vol. 3, no. 4

PHYSICS OF COMPLEX SYSTEMS

Mass Media Registration Certificate El No. FS77-77889, issued by Roskomnadzor on 10 February 2020

Peer-reviewed journal

Open Access

Published since 2020

4 issues per year

Editorial Board

Editor-in-chief Alexander V. Kolobov (Saint Petersburg, Russia)

Deputy Editor-in-chief Andrey K. Belyaev (Saint Petersburg, Russia)

Deputy Editor-in-chief Yuri A. Gorokhovatsky (Saint Petersburg, Russia)

Executive Secretary Alexey A. Kononov (Saint Petersburg, Russia)

Vachagan T. Avanesyan (Saint Petersburg, Russia)

Alexander P. Baraban (Saint Petersburg, Russia)

Sergey P. Gavrilov (Saint Petersburg, Russia)

Dmitry M. Gitman (São Paulo, Brazil)

Vladimir M. Grabov (Saint Petersburg, Russia)

Andrey A. Grib (Saint Petersburg, Russia)

Elisabeth Dalimier (Paris, France)

Alexander Z. Devdariani (Saint Petersburg, Russia)

Vadim K. Ivanov (Saint Petersburg, Russia)

Rene A. Castro Arata (Saint Petersburg, Russia)

Miloš Krbal (Pardubice, the Czech Republic)

Sergey A. Nемов (Saint Petersburg, Russia)

Oleg Yu. Prikhodko (Almaty, Kazakhstan)

Igor P. Pronin (Saint Petersburg, Russia)

Mikhail Yu. Puchkov (Saint Petersburg, Russia)

Alexey E. Romanov (Saint Petersburg, Russia)

Pavel P. Seregin (Saint Petersburg, Russia)

Koichi Shimakawa (Gifu, Japan)

Advisory Board

Gennady A. Bordovsky (Saint Petersburg, Russia)

Alexander V. Ivanchik (Saint Petersburg, Russia)

Vladimir V. Laptev (Saint Petersburg, Russia)

Alexander S. Sigov (Moscow, Russia)

Publishing house of Herzen State Pedagogical University of Russia

48 Moika Emb., Saint Petersburg 191186, Russia

E-mail: izdat@herzen.spb.ru

Phone: +7 (812) 312-17-41

Data size 5,18 Mbyte

Published at 20.12.2022

The contents of this journal may not be used in any way without a reference to the journal "Physics of Complex Systems" and the author(s) of the material in question.

Editors of the English text *M. V. Bumakova, I. A. Nagovitsyna*

Corrector *A. Yu. Gladkova*

Cover design by *O. V. Rudneva*

Layout by *A. M. Khodan, L. N. Kliuchanskaya*



Saint Petersburg, 2022

© Herzen State Pedagogical University of Russia, 2022

CONTENTS

| | |
|---|------------|
| Condensed Matter Physics | 154 |
| <i>Demidov E. V.</i> Extrema positions of charge carrier band spectrum in thin bismuth films | 154 |
| <i>Valeeva A. R., Kaptelov E. Yu., Pronin I. P., Senkevich S. V., Pronin V. P.</i> Mechanical stresses in lead zirconate titanate thin films formed on substrates differing in temperature coefficients of linear expansion | 159 |
| Theoretical Physics | 167 |
| <i>Gavrilov S. P.</i> Reduced integral representations for the probabilities of photon emission in a constant external electric field | 167 |
| <i>Liaptsev A. V.</i> Entropy and dimension of a chaotic attractor depending on the control parameter | 176 |
| <i>Timchenko B. A., Faleeva M. P., Gilev P. A., Blinova I. V., Popov I. Yu.</i> Atmospheric implementation of superdense coding quantum algorithm | 186 |
| Physics of Semiconductors | 202 |
| <i>Ilinskiy A. V., Shadrin E. B., Castro Arata R. A., Popova I. O.</i> Polarization processes in silver iodide films near the superionic phase transition temperature | 202 |
| Summaries in Russian | 214 |



Check for updates

Condensed Matter Physics. Physics of thin
films. Surfaces and interfaces

UDC 538.975

EDN HZBMJW

<https://www.doi.org/10.33910/2687-153X-2022-3-4-154-158>

Extrema positions of charge carrier band spectrum in thin bismuth films

E. V. Demidov^{✉1}

¹ Herzen State Pedagogical University of Russia, 48 Moika Emb., Saint Petersburg 191186, Russia

Author

Evgenii V. Demidov, ORCID: 0000-0002-1190-0376, e-mail: demidov_evg@mail.ru

For citation: Demidov, E. V. (2022) Extrema positions of charge carrier band spectrum in thin bismuth films. *Physics of Complex Systems*, 3 (4), 154–158. <https://www.doi.org/10.33910/2687-153X-2022-3-4-154-158> EDN HZBMJW

Received 4 September 2022; reviewed 2 October 2022; accepted 2 October 2022.

Funding: The research was supported by the Ministry of Education of the Russian Federation (project No. FSZN-2020-0026).

Copyright: © E. V. Demidov (2022). Published by Herzen State Pedagogical University of Russia. Open access under CC BY-NC License 4.0.

Abstract. Many studies report an increase in charge carrier concentration in thin bismuth films as their thickness decreases at low temperatures. These results are obtained on the basis of data on resistivity, magnetoresistance, Hall coefficient, and thermal EMF measured in these films. The calculation is most often carried out within the framework of the two-band approximation assuming the quadraticity of the dispersion law of electrons and holes. Using these approximations, it is possible to estimate the change in the position of energy extremes relative to the chemical potential in these films based on concentration values of charge carriers. This article presents all these calculations and analyses the extrema movement of the charge carrier band spectrum in bismuth films with a change in their thickness.

Keywords: thin films, bismuth, transport phenomena, charge carriers' concentration, band structure

Introduction

For many decades, crystals and low-dimensional objects of bismuth and its alloys with antimony have been of theoretical and practical interest to researchers. This interest is associated with the crystal and energy structure of this class of materials, which determines their unique electronic and thermoelectric properties (Abdelbarey et al. 2020; Grabov et al. 2010; Hirahara et al. 2015; Hsieh et al. 2008; Lenoir et al. 1996; Lv et al. 2010; Singh et al. 2018).

Our several studies (Demidov 2022; Demidov et al. 2018; 2020; 2022; Grabov et al. 2017) calculated the mobility and charge carrier concentration in bismuth films (111) with the thickness up to 15 nm formed on the mica (muscovite) substrate. The calculations were based on the data of resistivity, magnetoresistance, Hall coefficient, and thermoelectric power measured at the temperature of 80 K within the two-band approximation, assuming the dispersion law squareness for electrons and holes, and a number of additional approximations. The increase of charge carrier concentration in the thin bismuth films with the decrease in their thickness was observed in all works. In one study (Demidov 2022), charge carrier concentration was calculated using all the four transfer coefficients. In another study (Demidov et al. 2022), the concentration was calculated for a larger number of films. It should be noted that differences in the obtained results are significant only in films with the thickness less than 50 nm. That is why the results for charge carrier concentration with the thicknesses less than 50 nm were taken from the former mentioned study (Demidov 2022), while those for thicker bismuth films—from the latter (Demidov et al. 2022).

Method of calculating the extrema positions of the charge carrier band spectrum in thin bismuth films

Based on the obtained values of electron (n) and hole (p) concentrations, it is possible to determine the energy extrema positions of the valence and the conduction bands relative to the chemical potential level.

In this case, the dispersion law for L-electrons and T-holes can be approximated by a simple quadratic model.

For electrons:

$$n = 3 * \frac{2(2m_{n1}^* m_{n2}^* m_{n3}^*)^{1/2}}{3\pi^2 \hbar^3} (kT)^{3/2} \times F_{1/2}(\mu_n), \quad (1)$$

where $F_{1/2}(\mu)$ —Fermi integral. For electrons, the Fermi integral is:

$$F_{1/2}(\mu_n) = \frac{1}{\sqrt{\pi}} \int_0^\infty \frac{\varepsilon^{1/2}}{e^{\varepsilon - \mu_n} + 1} d\varepsilon, \quad (2)$$

where $\varepsilon = E/kT$, $\mu_n = E_{Fn}/kT$, E —energy, E_{Fn} —electron Fermi energy, m_{ni}^* —components of electron effective mass, in the coordinate system of the electron ellipsoid axes, where $i = 1, 2, 3$.

For holes:

$$p = \frac{2(2m_{p1}^* m_{p2}^* m_{p3}^*)^{1/2}}{3\pi^2 \hbar^3} (kT)^{3/2} \times F_{1/2}(\mu_p), \quad (3)$$

where

$$F_{1/2}(\mu_p) = \frac{1}{\sqrt{\pi}} \int_0^\infty \frac{\varepsilon^{1/2}}{e^{\varepsilon - \mu_p} + 1} d\varepsilon \quad (4)$$

Similar to electrons, in the case of holes $\mu_p = E_{Fp}/kT$, E_{Fp} —Fermi energy of holes, m_{pi}^* —components of electron effective mass, in the coordinate system of the electron ellipsoid axes, where $i = 1, 2, 3$.

Values of the effective mass components were taken equal to the corresponding values for massive monocrystals from V. M. Grabov's work (Grabov 1998).

By numerically solving equations (1), (2) and (3), (4), knowing the electron and hole concentrations for the thin bismuth film, it is possible to find the positions of energy extremes for the valence and the conduction bands.

Results and discussion

Figure 1 shows the dependence of electron and hole concentration on the thickness of bismuth films determined in previous studies (Demidov 2022; Demidov et al. 2022). In one of them (Demidov et al. 2022), electron and hole concentrations were assumed to be equal. However, in the other study (Demidov 2022), which took into account the thermoelectric coefficient in addition to the galvanomagnetic coefficients, it was possible not to use this approximation and to calculate the concentrations of electrons and holes separately. For thicknesses greater than 50 nm, the results obtained with the help of both approaches turned out to be quite close; however, for thinner films, different concentrations of electrons and holes were obtained (Demidov 2022), and this difference increased as the film thickness decreased.

Based on the values of electron and hole concentrations shown in Fig. 1, the energy extrema positions of the valence and the conduction bands relative to the chemical potential level were calculated. Fig. 2 shows the results of the calculations.

Figs. 1 and 2 show that, in a pure bismuth film, there is an overlap of energy extrema for all thicknesses, and its value increases with the decrease of film thickness. The strongest overlap growth begins in films with the thickness less than 30 nm. Notably, in the thinnest 15 nm film, the top of the valence band and

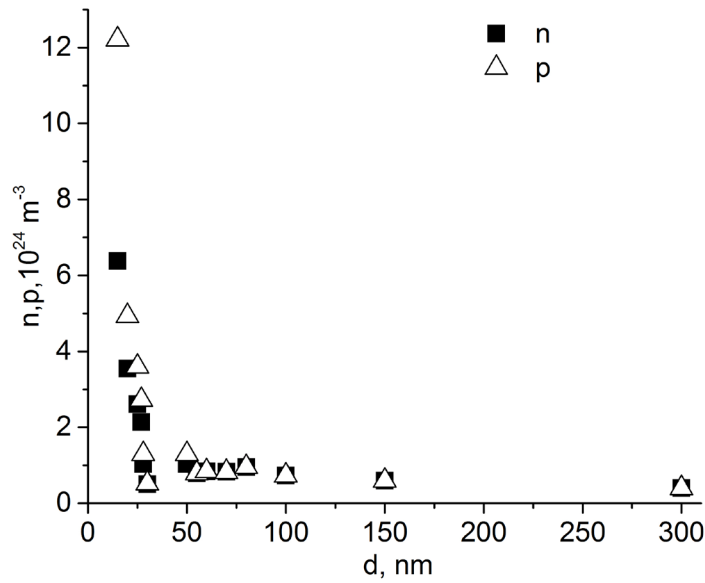


Fig. 1. Dependence of electron and hole concentration on bismuth film thickness at 80 K

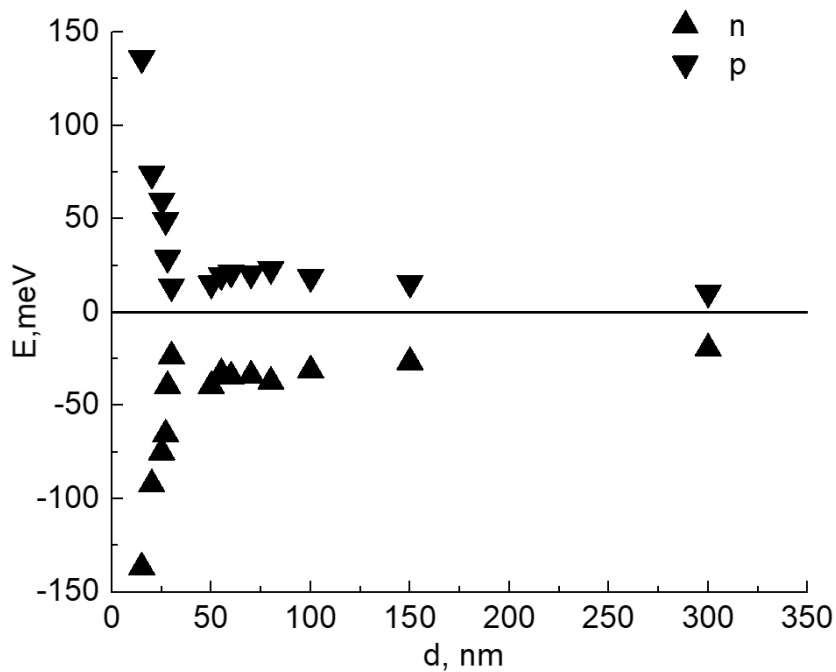


Fig. 2. The energy extrema positions of the valence and the conduction bands relative to the chemical potential level in the bismuth film at 80 K

the bottom of the conduction band are located symmetrically with respect to the chemical potential level.

In bismuth crystals in the massive state, the extrema of the valence and conduction bands with similar energy parameters of charge carriers are the extrema at the L point of the Brillouin zone. Thus, we can assume the actualisation of the hole extremum at point L in ultrathin bismuth films, in contrast to thicker films and bismuth monocrystals, where the valence band extremum at point T of the Brillouin zone is actual. It is possible that the same takes place in solid solution films $\text{Bi}_{95}\text{Sb}_5$ at 77 K, created on various substrates with the temperature expansion coefficient from $1 \times 10^{-6} \text{K}^{-1}$ to $40 \times 10^{-6} \text{K}^{-1}$

and, consequently, in a state of planar stretching or compression (temperature expansion coefficient of bismuth $10,5 \times 10^{-6} \text{ K}^{-1}$) (Suslov et al. 2018). In the case of solid solution films $\text{Bi}_{95}\text{Sb}_5$, the thickness of the samples was 1 μm , while such an effect was not observed in the massive crystal of this material.

For a bismuth film with the thickness 15 nm, the overlap of the valence and conduction bands is almost 300 meV. This corresponds to the increase in the metallic properties of the bismuth surface (111) in relation to its volume. This result was obtained from the first principles calculation of the band structure of the bismuth surface (111) and its study by angular resolution photoelectron spectroscopy (ARPES) (Hofmann 2006). The review (Hofmann 2006) indicates that the surface states structure of the planes (111), (110) and (100) differs significantly from the massive band structure of bismuth. One of the manifestations of these differences can be the observed symmetry of the top of the valence band and the bottom of the conduction band in 15 nm films.

Conclusion

Based on the data on the increase of the charge carrier concentration with the increase of the bismuth film thickness (111) created on a mica substrate, the changes in the energy extrema position of the band structure of thin bismuth films with the thickness from 300 to 15 nm were calculated.

The increase in the overlap of the valence and conduction bands with decreasing film thickness was revealed. In addition, the symmetry of the top of the valence band and the bottom of the conduction band, which occurs in 15 nm films, was found.

Conflict of interest

The author declares that there is no conflict of interest, either existing or potential.

References

- Abdelbarey, D., Koch, J., Mamiyev, Z. et al. (2020) Thickness-dependent electronic transport through epitaxial nontrivial Bi quantum films. *Physical Review B*, 102 (11), article 115409. <https://doi.org/10.1103/PhysRevB.102.115409> (In English)
- Demidov, E. V. (2022) On the problem of calculating the concentration and mobility of charge carriers in thin bismuth films and a bismuth-antimony solid solution. *Journal of Surface Investigation: X-ray, Synchrotron and Neutron Techniques*, 16 (5), 712–719. (In English)
- Demidov, E., Gerega, V., Grabov, V. et al. (2020) Topological insulator's state in bismuth thin films. *AIP Conference Proceedings*, 2308, article 050007. <https://doi.org/10.1063/5.0034335>. (In English)
- Demidov, E. V., Grabov, V. M., Komarov, V. A. et al. (2018) Topological insulator state in thin bismuth films subjected to plane tensile strain. *Physics of the Solid State*, 60 (3), 457–460. <https://doi.org/10.1134/S106378341803006X> (In English)
- Demidov, E. V., Grabov, V. M., Komarov, V. A. et al. (2022) Rost kontsentratsii nositelej zaryada v tonkikh plenkakh vismuta [An increase in the concentration of charge carriers in thin films of bismuth]. *Fizika i tekhnika poluprovodnikov — Physics and Technology of Semiconductors*, 56 (2), 149–155. <https://doi.org/10.21883/FTP.2022.02.51952.19> (In Russian)
- Grabov, V. M. (1998) *Energeticheskij spektr i mekhanizmy relaksatsii nositelej zaryada v legirovannykh kristallakh vismuta, sur'my i splavov vismut-sur'ma [Energy spectrum and relaxation mechanisms of charge carriers in doped crystals of bismuth, antimony and bismuth-antimony alloys]*. PhD dissertation (Physics). Saint Petersburg, Herzen State Pedagogical University of Russia, 603 p. (In Russian)
- Grabov, V. M., Komarov, V. A., Demidov, E. V., Klimantov, M. M. (2010) Yavleniya perenosa v monokristallicheskih plenkakh vismuta [Transport phenomena in monocrystalline bismuth films]. *Izvestia Rossijskogo gosudarstvennogo pedagogicheskogo universiteta im. A. I. Gertsena — Izvestia: Herzen University Journal of Humanities & Sciences*, 122, 22–31. (In Russian)
- Grabov, V. M., Komarov, V. A., Demidov, E. V. et al. (2017) The galvanomagnetic properties of bismuth films with thicknesses of 15–150 nm on mica substrates. *Universitetskij nauchnyj zhurnal — Humanities and Science University Journal*, 27, 56–68. (In English)
- Hirahara, T., Shirai, T., Hajiri, T. et al. (2015) Role of quantum and surface-state effects in the bulk fermi-level position of ultrathin bi films. *Physical Review Letters*, 115 (10), article 106803. <https://doi.org/10.1103/PhysRevLett.115.106803> (In English)
- Hofmann, P. (2006) The surfaces of bismuth: Structural and electronic properties. *Progress in Surface Science*, 81 (5), 191–245. <https://doi.org/10.1016/j.progsurf.2006.03.001> (In English)

- Hsieh, D., Qian, D., Wray, L. et al. (2008) A topological Dirac insulator in a quantum spin Hall phase. *Nature*, 452 (7190), 970–974. <https://doi.org/10.1038/nature06843> (In English)
- Lenoir, B., Cassart, M., Michenaud, J.-P. et al. (1996) Transport properties of Bi-RICH Bi-Sb alloys. *Journal of Physics and Chemistry of Solids*, 57 (1), 89–99. [https://doi.org/10.1016/0022-3697\(95\)00148-4](https://doi.org/10.1016/0022-3697(95)00148-4) (In English)
- Lv, H. Y., Liu, H. J., Pan, L. et al. (2010) Structural, electronic, and thermoelectric properties of BiSb nanotubes. *Journal of Physical Chemistry*, 114 (49), 21234–21239. <https://doi.org/10.1021/jp108231j> (In English)
- Singh, S., Valencia-Jaime, L., Pavlic, O., Romero, A. H. (2018) Effect of spin-orbit coupling on the elastic, mechanical, and thermodynamic properties of Bi-Sb binaries. *Physical Review B*, 97, article 054108. <https://doi.org/10.1103/PhysRevB.97.054108> (In English)
- Suslov, A. V., Grabov, V. M., Komarov, V. A. et al. (2018) The band-structure parameters of $\text{Bi}_{1-x}\text{Sb}_x$ ($0 \leq x \leq 0.15$) Thin films on substrates with different thermal-expansion coefficients. *Semiconductors*, 53 (5), 611–614. <https://doi.org/10.1134/S1063782619050269> (In English)



Check for updates

Condensed Matter Physics. Dielectric Physics

UDC 537.226.4

EDN IWJDKZ

<https://www.doi.org/10.33910/2687-153X-2022-3-4-159-166>

Mechanical stresses in lead zirconate titanate thin films formed on substrates differing in temperature coefficients of linear expansion

A. R. Valeeva^{✉1}, E. Yu. Kaptelov¹, I. P. Pronin¹, S. V. Senkevich^{1,2}, V. P. Pronin²

¹ Ioffe Institute, 26 Politekhnicheskaya Str., Saint Petersburg 194021, Russia

² Herzen State Pedagogical University of Russia, 48 Moika Emb., Saint Petersburg 191186, Russia

Authors

Alsu R. Valeeva, ORCID: [0000-0002-8826-8938](https://orcid.org/0000-0002-8826-8938), e-mail: Valeevaar@mail.ioffe.ru

Evgeny Yu. Kaptelov, ORCID: [0000-0002-7423-6943](https://orcid.org/0000-0002-7423-6943), e-mail: kaptelov@mail.ioffe.ru

Igor P. Pronin, ORCID: [0000-0003-3749-8706](https://orcid.org/0000-0003-3749-8706), e-mail: petrovich@mail.ioffe.ru

Stanislav V. Senkevich, ORCID: [0000-0002-4503-1412](https://orcid.org/0000-0002-4503-1412), e-mail: SenkevichSV@mail.ioffe.ru

Vladimir P. Pronin, ORCID: [0000-0003-0997-1113](https://orcid.org/0000-0003-0997-1113), e-mail: pronin.v.p@yandex.ru

For citation: Valeeva, A. R., Kaptelov, E. Yu., Pronin, I. P., Senkevich, S. V., Pronin, V. P. (2022) Mechanical stresses in lead zirconate titanate thin films formed on substrates differing in temperature coefficients of linear expansion.

Physics of Complex Systems, 3 (4), 159–166. <https://www.doi.org/10.33910/2687-153X-2022-3-4-159-166> EDN IWJDKZ

Received 13 September 2022; reviewed 30 September 2022; accepted 30 September 2022.

Funding: The study did not receive any external funding.

Copyright: © A. R. Valeeva, E. Yu. Kaptelov, I. P. Pronin, S. V. Senkevich, V. P. Pronin (2022). Published by Herzen State Pedagogical University of Russia. Open access under [CC BY-NC License 4.0](https://creativecommons.org/licenses/by-nc/4.0/).

Abstract. The article considers the influence of linear and bending stresses on the magnitude of the internal field and self-polarisation in thin lead zirconate titanate (PZT) films formed on silicon and glass-ceramic ST-50 substrates by radio-frequency magnetron sputtering. PZT composition corresponded to the region of the morphotropic phase boundary. It is assumed that bending stresses in “thin PZT film-substrate” bimorph structures lead to the appearance of an internal electric field caused by the diffusion of charged oxygen vacancies (Gorsky effect in ferroelectrics).

Keywords: thin ferroelectric films, lead zirconate titanate, morphotropic phase boundary, mechanical stresses, internal electric field, self-polarisation, Gorsky effect

Introduction

In the last decade, thin ferroelectric films have been increasingly used in various microelectromechanical systems (MEMS), not only as sensors, actuators, acoustic devices, infrared (IR) sensors (Izyumskaya et al. 2007; Muralt 2001; Polla 1995), but also in magnetoelectric devices, harvesters (energy microstorage), microwave converters, etc. (Bukharaev et al. 2018; Eerenstein et al. 2006; Kang et al. 2016; Ma et al. 2021; Muralt 2008). The vast majority of MEMS application of ferroelectric films (about 95%) is associated with the use of lead zirconate titanate (PZT) thin films, the composition of which corresponds to the morphotropic phase boundary (MPB) region, where the electromechanical, pyroelectric, and other important physical parameters of the films reach extremely high values (Song et al. 2021).

From a technological point of view, it is most efficient to use the so-called self-polarised films, which, as a result of synthesis, are characterised by macroscopic polarisation comparable in magnitude to spontaneous polarisation (Afanasjev et al. 2001; Bruchhaus et al. 1999; Kholkin et al. 1998; Sviridov et al. 1994). However, it is by no means always possible to obtain such films, and the reason for this is

the effect of mechanical stresses on them from the side of the substrate. Since, in practice, the majority of used polycrystalline PZT films are formed on platinised silicon substrates and characterised by one or another growth texture, the appearance of mechanical stresses is usually associated with the difference in the temperature coefficients of linear expansion of the film and the substrate (Bruchhaus et al. 1999; Ogawa et al. 1991; Pronin et al. 2003). In this case, the question of the discrepancy between the lattice parameters of the film and the substrate (or the conducting sublayer) can be excluded from consideration.

Moreover, in a number of works it is assumed that mechanical stresses are the main reasons leading to the formation of microscopic polarisation (Bursian et al. 1969; Delimova et al. 2021; Garten, Trolier-McKinstry 2015; Gruverman et al. 2003; Sviridov et al. 1994; Yudin, Tagantsev 2013). An analysis of the literature discussing the role and influence of mechanical stresses on the properties of thin PZT films showed that, firstly, it is necessary to separate the effect of linear and bending mechanical stresses on the orientation of the ferroelectric polarisation, and, secondly, the degree of their influence can vary depending on the number of factors, such as film deposition temperature, annealing temperature (synthesis temperature of the perovskite phase), degree of film porosity, one or the other growth texture, presence of sublayers used and their thickness, etc. The lack of unambiguity and clarity in assessing the contribution of mechanical stresses to the occurrence and magnitude of self-polarisation in thin PZT films determined the aim of this study.

Objects and methods of study

The comparison of physical properties was carried out on polycrystalline PZT films formed on substrates with different temperature coefficients of linear expansion. Their composition corresponded to the MPB region. Thin films were prepared using a two-stage method. At the first stage, they were deposited on substrates using the method of radio-frequency (RF) magnetron sputtering of a PZT ceramic target; at the second stage, they were annealed in air at temperatures of 550–600 °C (Pronin et al. 2010). Thin wafers of silicon and glass-ceramic ST-50 were used as substrates. At room temperature, the temperature coefficients of linear expansion of these substrates and the investigated PZT solid solution are $2.8 \times 10^{-6} \text{ K}^{-1}$, $5.0 \times 10^{-6} \text{ K}^{-1}$ and $3.0 \times 10^{-6} \text{ K}^{-1}$ respectively.

According to our calculations (Fig. 1), at room temperature, in the “PZT-silicon” bimorph structure tensile stresses act on the thin film from the side of the substrate, while in the “PZT-glass-ceramic” bimorph structure compressive stresses act. The thickness of the studied films was 500–1000 nm. A continuous layer of the lower platinum electrode 100–200 nm thick was formed on the surface of the substrates. To study the ferroelectric properties, contact pads of platinum $200 \times 200 \mu\text{m}$ in size were deposited on the surface of the formed films.

To study the dielectric polarisation (P-V curves), a modified Sawyer-Tower measuring circuit was used. An automated setup based on an E7-20 immittance meter made it possible to measure the reversible dependences of sample capacitances (C-V curves) at bias voltages in the range of $\pm 40 \text{ V}$.

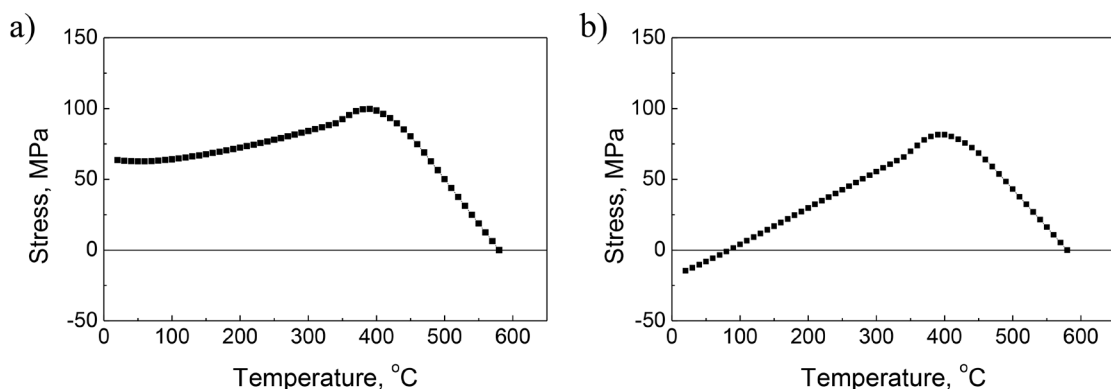


Fig. 1. Calculated temperature dependences of mechanical stresses arising in $\text{PbZr}_{0.5}\text{Ti}_{0.5}\text{O}_3$ (PZT) films deposited on (a) silicon and (b) glass-ceramic substrates (negative stress values correspond to film compression)

Influence of linear mechanical stresses

The nature of mechanical stresses (compressive or tensile) arising in thin polycrystalline (ceramic) films depends on the difference in the temperature coefficients of the thin film (α_p) and the substrate (α_{sub}). In the “PZT-silicon” structure, where the composition of the film corresponds to the MPB region (i. e., with the ratio $\alpha_{PZT} > \alpha_{Si}$), two-dimensional tensile stresses, if they are sufficiently high, orient the spontaneous polarisation vector in the direction as close as possible to the substrate plane (Fig. 1a, Fig. 2a). In the “PZT-glass-ceramic” structure (i. e., at $\alpha_{PZT} < \alpha_{glass}$), compressive stresses reorient the ferroelectric polarisation in a direction close to the normal to the substrate surface (Fig. 1b, Fig. 2b).

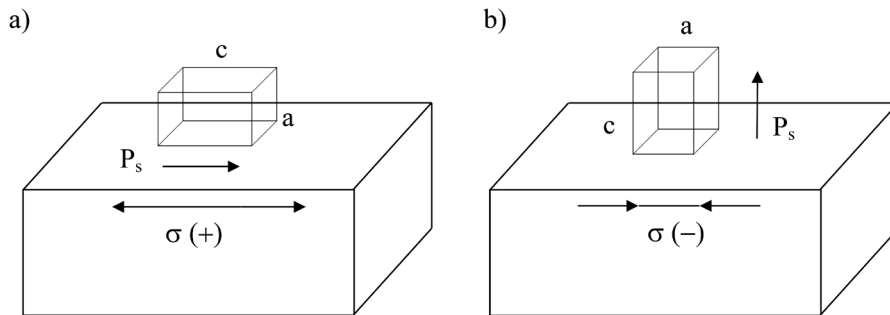


Fig. 2. Diagram illustrating the effects of mechanical tension ($\sigma+$) (a) and compression ($\sigma-$) (b) with sides of the substrate on deformation of the unit cell and the orientation of the polar axis in $\langle 100 \rangle$ -textured tetragonal PZT film

Calculations of the magnitude and sign of mechanical stresses (Pronin et al. 2003) showed that tensile stresses of ~ 60 MPa act on the film from the side of the silicon substrate (Fig. 1a), while small compressive stresses act on the side of the glass-ceramic substrate.

A similar approach can be extended to films that differ in growth texture. Fig. 3 shows the changes in the value of the macroscopic polarisation relative to spontaneous polarisation in PZT films with a change in the lattice symmetry in the MPB region from the tetragonal to the rhombohedral modification under conditions of tension (for the case of a silicon substrate, Fig. 3a) or compression (for the case of a glass-ceramic substrate, Fig. 3b). It is clear that the effect of two-dimensional stresses on the change in macroscopic polarisation differs radically with a change in the growth orientation of a thin film.

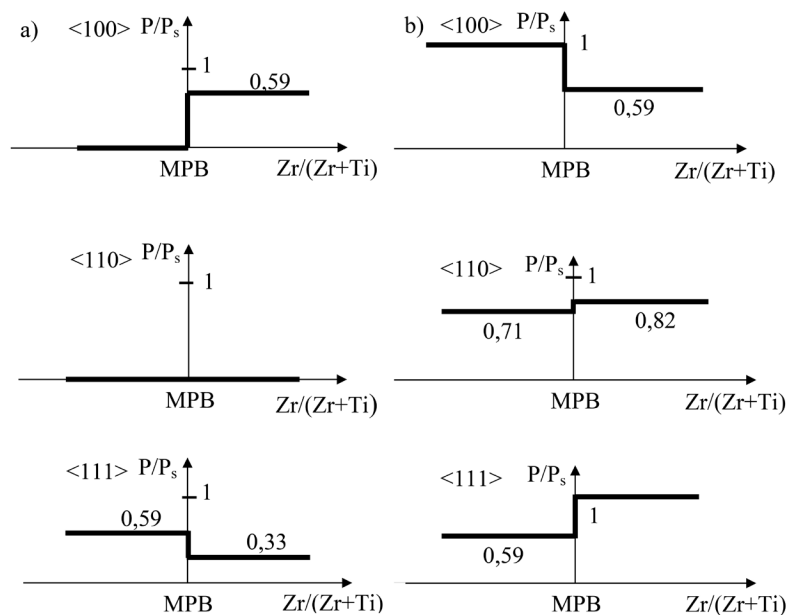


Fig. 3. Diagram of the self-polarised state (in relative units) in the MPB region for $\langle 100 \rangle$, $\langle 110 \rangle$ and $\langle 111 \rangle$ —oriented thin PZT films formed on silicon (under tension) (a) and glass-ceramic (under compression) (b) substrates

In the “PZT-glass-ceramic” structure, a thin film is in a state of compression, and the macroscopic polarisation can reach the value of spontaneous polarisation depending on the growth orientation and the elemental ratio (Zr/Ti), corresponding to the tetragonal (T) or rhombohedral (Rh) modification of the ferroelectric phase. In the “PZT-silicon” structure, tensile mechanical stresses of the order of 60 MPa are quite enough to reorient the polarisation in the direction as close as possible to the plane of the substrate, and a jump corresponds to the transition from the tetragonal to the rhombohedral phase at MPB region, leading to a decrease in the self-polarisation value to unacceptably low values for practical applications in (111)-oriented films (Fig. 3a) (Pronin et al. 2003).

In a real situation, the magnitude and orientation of macroscopic polarisation is determined by the ratio of mechanical and electrical forces acting on a thin film. Fig. 4 shows the hysteresis loops of thin PZT films of composition corresponding to the MPB region formed on silicon and glass-ceramic (Fig. 4b) substrates. It is clear that the asymmetry of the hysteresis loop is more pronounced in the film formed on the glass-ceramic substrate than on the silicon one. While in the second case the value of the internal field was 48 kV/cm and the value of self-polarisation was 0.7 of the value of the spontaneous polarisation, in the first case the internal field reached only 28 kV/cm and the value of self-polarisation did not exceed 0.4 of the spontaneous polarisation. The difference in self-polarisation values reflects the effect of tensile stresses on the film from the side of silicon.

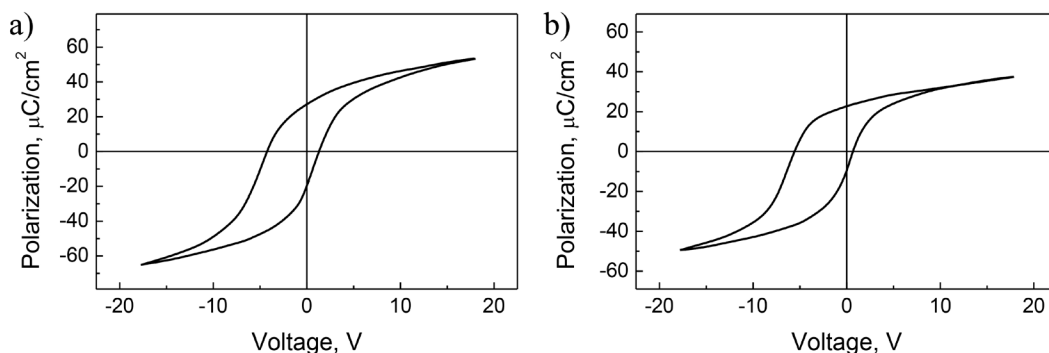


Fig. 4. P-V loops of thin PZT films deposited on (a) silicon and (b) glass-ceramic substrates. Films thickness—500 nm, sintering temperature—550 °C

Influence of bending mechanical stresses

Despite the fact that the main reason for the appearance of internal field and self-polarisation in thin PZT films is considered to be the charging of the lower interface of the thin-film structure (Afanasjev et al. 2001; Kholkin et al. 1998), the effect of bending mechanical stresses cannot be ruled out. It is well known that, under the action of a gradient of mechanical stresses in the crystal lattice, atoms shift relative to each other, where larger atoms are displaced in the direction of extension and small atoms—in the opposite direction, causing the appearance of an internal field and polar dipoles (Bursian et al. 1969). Subsequently, the effect was called the flexoelectric effect (Gruverman et al. 2003; Yudin, Tagantsev 2013).

Experiments revealed that in the case of strong bending stresses (at a curvature radius of ~30 cm) a change in the sign of the mechanical stress gradient leads to a reorientation of the macroscopic polarisation. Such effects were observed on thin plates of barium titanate (BaTiO_3) (Bursian et al. 1969) (Fig. 5) and in thin PZT films (Gruverman et al. 2003). Moreover, a polar state can also arise in thin nonpolar layers (Ehre et al. 2007). In this regard, the flexoelectric effect is still considered one of the probable causes of an internal electric field and the self-polarisation associated with it (Delimova et al. 2021). Estimates of the polarising electric field performed for thin PZT films showed that the magnitude of such fields is several orders of magnitude lower than the coercive field. Therefore, the authors conclude that there is another, stronger contribution to the flexoelectric effect (Gruverman et al. 2003).

One of such possible contributions can be the effect associated with the directed diffusion of charged vacancies, better known in relation to the multidirectional diffusion of atoms in metal alloys as the Gorsky effect (or the upward diffusion effect) (Gorsky 1935). The essence of the effect is that under action

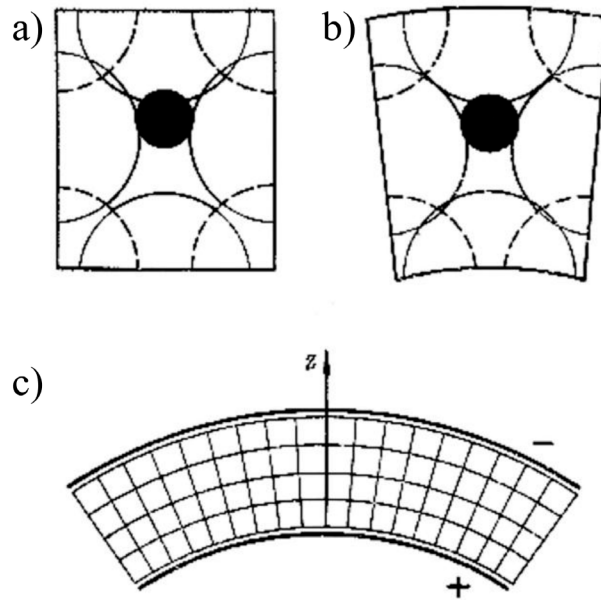


Fig. 5. Distortion of elementary cells of barium titanate under external electric field application (a) in an infinite crystal; (b) and (c) in a thin plate, leading to a flexoelectric effect

of mechanical stresses gradient, atoms with a larger ionic radius move to the region of sample tension, while atoms with a smaller radius move to the region of compression. This effect is reversible: when the external load is removed, the concentration of point defects is equalised over the sample. Subsequently, A. M. Kosevich extended the effect to directed diffusion of vacancies (Kosevich 1975). As applied to thin oxide ferroelectrics, we can talk about the diffusion of charged oxygen vacancies (Barbashov, Komysa 2005; Pronin et al. 2017).

In this connection, a comparative study of the aging of thin PZT films formed on silicon and glass-ceramic substrates was carried out in this work. The studied samples were initially characterised by asymmetry of C-V characteristics and P-V loops, that is, they were characterised by the presence of an internal field and self-polarisation. Then the capacitor thin-film PZT structures were subjected to high-temperature annealing above the Curie temperature (at ~ 400 °C) and then aging within 10^6 s at room temperature.

High-temperature annealing of samples usually leads to symmetrisation of hysteresis loops (P-V), which is associated with a symmetrical redistribution of mobile charge carriers (electrons) between the upper and lower interfaces of the structure (Okamura et al. 1999; Pronin et al. 2002a). The experiments showed that the films formed on the glass-ceramic substrate had practically symmetrical P-V characteristics even after aging (Fig. 6b). The situation was different in a film formed on a silicon substrate. In that case aging led to the appearance of an internal field, the averaged over the film thickness magnitude reached 5–7 kV/cm (Fig. 6a). It corresponded to the appearance of a surface charge of ~ 0.4 $\mu\text{C}/\text{cm}^2$.

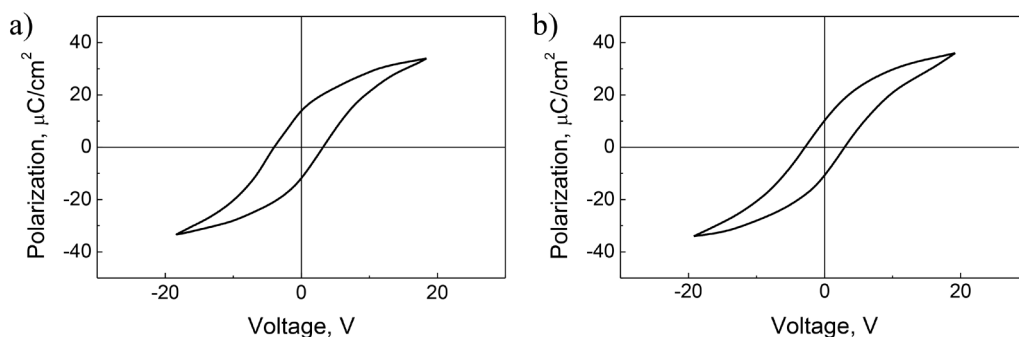


Fig. 6. P-V loops of thin PZT films formed on (a) silicon and (b) glass-ceramic substrates after annealing and subsequent aging

We assumed that the reason for the appearance of the field is the directed diffusion of charged oxygen vacancies towards the upper interface of the structure, which is caused by bending of the “PZT-silicon” bimorph structure due to the difference in the temperature coefficients of linear expansion of the thin film and the silicon substrate (Fig. 7), in contrast to the “PZT-glass-ceramic” structure, in which the action of two-dimensional mechanical stresses on a thin film is insignificant at room temperature. The calculation of the radius curvature of the structure using the Stoney formula (Bruchhaus et al. 1999) showed that its value is several orders of magnitude larger (~ 130 m) than in the case of the flexoelectric effect. With such a bending, the diffusion of oxygen vacancies occurs in the direction of structure compression, i. e., in the direction of the free surface of the film, and the orientation of the internal field occurs in the direction of the substrate.

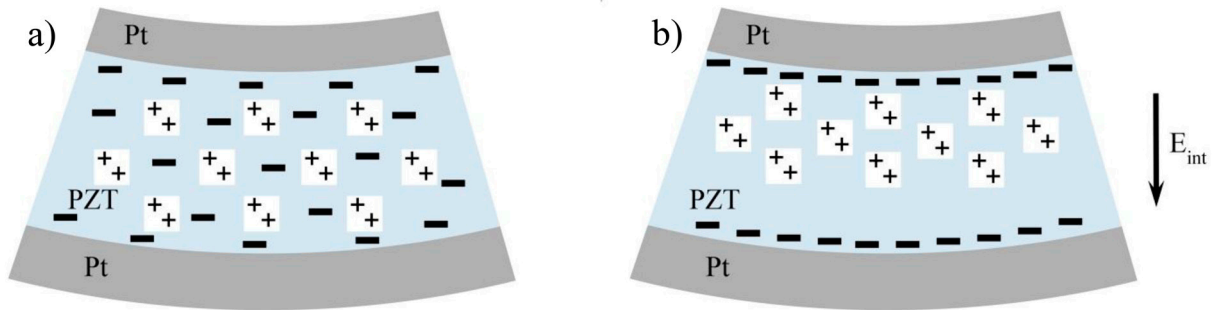


Fig. 7. Schematic representation of the space charges distribution in a thin PZT film after annealing above the Curie temperature (at ~ 400 °C) (a) and aging (b). The arrow shows the orientation of the internal electrical field vector (E_{int})

Assuming the charge is accumulated due to the diffusion of charged oxygen vacancies, the minimum required volume concentration of charged oxygen vacancies in a thin PZT film with a thickness of $1 \mu\text{m}$ should be no less than $\sim 10^{17}/\text{cm}^3$ under the assumption that all the vacancies present in the bulk of the film are concentrated near the upper interface of the structure. Taking into account that the activation energy of oxygen vacancies is ~ 0.22 eV (Pronin et al. 2002b), it is necessary to make a correction for the fraction of charged vacancies, which at room temperature are approximately two orders of magnitude smaller than uncharged vacancies. Taking this into account, the required concentration of vacancies (N^v) must be no less than $\sim 10^{19}/\text{cm}^3$, i. e., a value quite admissible for thin PZT films. Taking into account that the value of the diffusion coefficient of oxygen vacancies in a thin PZT film at room temperature is not so high (its estimates in the literature give the value $D_v \sim 5 \times 10^{-16} \text{ cm}^2/\text{s}$) (Holzlechner et al. 2014), and not all vacancies have time to diffuse during the experiment towards the upper interface, the real value of N^v should be increased by another order of magnitude.

Conclusion

The paper compares the action of linear biaxial mechanical stresses acting on a thin PZT ferroelectric film from the side of substrates, in which the integral temperature coefficient of linear expansion is either higher (glass-ceramic substrate ST-50) or lower than that of thin PZT films (silicon substrate), whose composition corresponds to the MPB region.

It is shown that the use of a silicon wafer as a substrate leads to stretching of the PZT film and partial reorientation of the ferroelectric polarisation vector in the direction as close as possible to the plane of the substrate. At the same time, this leads to bending of the “PZT-silicon” bimorphic structure and creates conditions for the directed diffusion of charged oxygen vacancies and the formation of an internal electric field, i.e., to the Gorsky effect in ferroelectric structures.

It is shown that, at a sufficient concentration of oxygen vacancies in a thin PZT film, bending stresses can lead to formation of an internal field and the resulting self-polarised state.

For a more thorough study of the Gorsky effect and a quantitative assessment of its contribution to the formation of an internal field and self-polarisation in thin-film ferroelectrics, it is necessary to further study the diffusion of oxygen vacancies at temperatures above room temperature and take into account

the contribution to the bending of the “PZT-silicon substrate” structure from such sublayers as silicon dioxide, an adhesive layer of titanium (or titanium oxide), as well as platinum electrodes (lower and upper).

Conflict of interest

The authors declare that there is no conflict of interest, either existing or potential.

Author contributions

The authors have made an equal contribution to the preparation of the text.

References

- Afanasjev, V. P., Petrov, A. A., Pronin, I. P. et al. (2001) Polarization and self-polarization in thin $\text{PbZr}_{1-x}\text{Ti}_x\text{O}_3$ (PZT) films. *Journal of Physics: Condensed Matter*, 13 (39), article 8755. <https://doi.org/10.1088/0953-8984/13/39/304> (In English)
- Barbashov, V. I., Komysa, Yu. A. (2005) Mechanoelectric effect in solid electrolytes. *Physics of the Solid State*, 47 (2), 238–242. <https://doi.org/10.1134/1.1866400> (In English)
- Bruchhaus, R., Pitzer, D., Schreiter, M., Wersing, W. (1999) Optimized PZT thin films for pyroelectric IR detector arrays. *Journal of Electroceramics*, 3 (2), 151–162. <https://doi.org/10.1023/A:1009995126986> (In English)
- Bukharaev, A. A., Zvezdin, A. K., Pyatakov, A. P. et al. (2018) Straintronics: A new trend in micro- and nanoelectronics and materials science. *Physics-Uspexhi*, 61 (12), article 1175. <https://doi.org/10.3367/UFNe.2018.01.038279> (In English)
- Bursian, E. V., Zaikovskii, O. I., Makarov, K. V. (1969) Polyarizatsiya segnetoelektricheskoy plastiny iz gibom [Polarization of a ferroelectric plate by bending]. *Izvestiya akademii nauk SSSR — Bulletin of the Academy of Sciences of the USSR*, 33 (7), 1098–1101. (In Russian)
- Delimova, L. A., Zaitseva, N. V., Ratnikov, V. V. et al. (2021) Comparison of characteristics of thin PZT films on Si-on-Sapphire and Si Substrates. *Physics of the Solid State*, 63 (8), 1145–1152. <https://doi.org/10.1134/S1063783421080060> (In English)
- Eerenstein, W., Mathur, N. D., Scott, J. F. (2006) Multiferroic and magnetoelectric materials. *Nature*, 442, 759–765. <https://doi.org/10.1038/nature05023> (In English)
- Ehre, D., Lyahovitskaya, V., Tagantsev, A., Lubomirsky, I. (2007) Amorphous piezo- and pyroelectric phases of BaZrO_3 and SrTiO_3 . *Advanced Materials*, 19 (11), 1515–1517. <https://doi.org/10.1002/adma.200602149> (In English)
- Garten, L. M., Trolrier-McKinstry, S. (2015) Enhanced flexoelectricity through residual ferroelectricity in barium strontium titanate. *Journal of Applied Physics*, 117 (9), article 094102. <https://doi.org/10.1063/1.4913858> (In English)
- Gorsky, W. S. (1935) Theorie des elastischen Nachwirkung in ungeordneten Mischkristallen (elastische Nachwirkung zweiter Art) [Theory of elastic after-effects in disordered mixed crystals (elastic after-effects of the second kind)]. *Physikalische Zeitschrift der Sowjetunion*, 8, 457–471. (In German)
- Gruverman, A., Rodriguez, B. J., Kingon, A. I., Nemanich, R. J. (2003) Mechanical stress effect on imprint behavior of integrated ferroelectric capacitors. *Applied Physics Letters*, 83 (4), article 728. <https://doi.org/10.1063/1.1593830> (In English)
- Holzlechner, G., Kastner, D., Slouka, C. et al. (2014) Oxygen vacancy redistribution in $\text{PbZr}_x\text{Ti}_{1-x}\text{O}_3$ (PZT) under the influence of an electric field. *Solid State Ionics*, 262, 625–629. <https://doi.org/10.1016/j.ssi.2013.08.027> (In English)
- Izyumskaya, N., Alivov, Y.-I., Cho, S.-J. et al. (2007) Processing, structure, properties, and applications of PZT thin films. *Critical Reviews in Solid State and Materials Sciences*, 32 (3-4), 111–202. <https://doi.org/10.1080/10408430701707347> (In English)
- Kang, M.-G., Jung, W.-S., Kang, Ch.-Y., Yoon, S.-J. (2016) Recent progress on PZT based piezoelectric energy harvesting technologies. *Actuators*, 5 (1), article 5. <https://doi.org/10.3390/act5010005> (In English)
- Kholkin, A. L., Brooks, K. G., Taylor, D. V. et al. (1998) Self-polarization effect in $\text{Pb}(\text{Zr,Ti})\text{O}_3$ thin films. *Integrated Ferroelectrics*, 22 (1-4), 525–533. <https://doi.org/10.1080/10584589808208071> (In English)
- Kosevich, A. M. (1975) How a crystal flows. *Soviet Physics Uspexhi*, 17 (6), 920–930. <https://doi.org/10.1070/PU1975v017n06ABEH004405> (In English)
- Ma, Y., Son, J., Wang, X. et al. (2021) Synthesis, microstructure and properties of magnetron sputtered lead zirconate titanate (PZT) thin film coatings. *Coatings*, 11 (8), article 944. <https://doi.org/10.3390/coatings11080944> (In English)
- Muralt, P. (2001) Micromachined infrared detectors based on pyroelectric thin films. *Reports on Progress in Physics*, 64 (10), 1339–1388. <https://doi.org/10.1088/0034-4885/64/10/203> (In English)

- Muralt, P. (2008) Recent progress in materials issues for piezoelectric MEMS. *Journal of American Ceramic Society*, 91 (5), 1385–1396. <https://doi.org/10.1111/j.1551-2916.2008.02421.x> (In English)
- Ogawa, T., Senda, A., Kasanami, T. (1991) Controlling the crystal orientations of lead titanate thin films. *Japanese Journal of Applied Physics*, 30 (9S), article 2145. <https://doi.org/10.1143/JJAP.30.2145> (In English)
- Okamura, S., Miyata, S., Mizutani, Y. et al. (1999) Conspicuous voltage shift of D-E hysteresis loop and asymmetric depolarization in Pb-based ferroelectric thin films. *Japanese Journal of Applied Physics*, 38 (9S), article 5364. <https://doi.org/10.1143/JJAP.38.5364> (In English)
- Polla, D. L. (1995) Microelectromechanical systems based on ferroelectric thin films. *Microelectronic Engineering*, 29 (1-4), 51–58. [https://doi.org/10.1016/0167-9317\(95\)00114-X](https://doi.org/10.1016/0167-9317(95)00114-X) (In English)
- Pronin, I. P., Kaptelov, E. Yu., Gol'tsev, A. V., Afanas'ev, V. P. (2003) The effect of stresses on self-polarization of thin ferroelectric films. *Physics of the Solid State*, 45 (9), 1768–1773. <https://doi.org/10.1134/1.1611249> (In English)
- Pronin, I. P., Kaptelov, E. Yu., Tarakanov, E. A., Afanas'ev, V. P. (2002a) Effect of annealing on the self-poled state in thin ferroelectric films. *Physics of the Solid State*, 44 (9), 1736–1740. <https://doi.org/10.1134/1.1507258> (In English)
- Pronin, I. P., Kaptelov, E. Yu., Tarakanov, E. A. et al. (2002b) Self-polarization and migratory polarization in thin lead zirconate-titanate films. *Physics of the Solid State*, 44 (4), 769–773. <https://doi.org/10.1134/1.1470574> (In English)
- Pronin, I. P., Kukushkin, S. A., Spirin, V. V. et al. (2017) Formation mechanisms and the orientation of self-polarization in PZT polycrystalline thin films. *Materials Physics and Mechanics*, 30 (1), 20–34. (In English)
- Pronin, V. P., Senkevich, S. V., Kaptelov, E. Yu., Pronin, I. P. (2010) Features of the formation of a perovskite phase in thin polycrystalline Pb(Zr,Ti)O₃ Films. *Journal of Surface Investigation. X-ray, Synchrotron and Neutron Techniques*, 4 (5), 703–708. <https://doi.org/10.1134/S1027451010050010> (In English)
- Song, L., Glinsek, S., Defay, E. (2021) Toward low-temperature processing of lead zirconate titanate thin films: Advances, strategies, and applications. *Applied Physics Reviews*, 8 (4), article 041315. <https://doi.org/10.1063/5.0054004> (In English)
- Sviridov, E., Sem, I., Alyoshin, V. et al. (1994) Ferroelectric film self-polarization. *MRS Online Proceedings Library*, 361, 141–146. <https://doi.org/10.1557/PROC-361-141> (In English)
- Yudin, P. V., Tagantsev, A. K. (2013) Fundamentals of flexoelectricity in solids. *Nanotechnology*, 24 (43), article 432001. <https://doi.org/10.1088/0957-4484/24/43/432001> (In English)



Check for updates

Theoretical physics. Relativistic quantum theory. Quantum theory of field

UDC 530.22

EDN ORISSK

<https://www.doi.org/10.33910/2687-153X-2022-3-4-167-175>

Reduced integral representations for the probabilities of photon emission in a constant external electric field

S. P. Gavrilov^{✉1,2}

¹ Herzen State Pedagogical University of Russia, 48 Moika Emb., Saint Petersburg 191186, Russia

² Tomsk State University, Lenin ave. 36, Tomsk 634050, Russia

Author

Sergey P. Gavrilov, ORCID: [0000-0002-0350-3012](https://orcid.org/0000-0002-0350-3012), e-mail: gavrilovsergeyp@yahoo.com

For citation: Gavrilov, S. P. (2022) Reduced integral representations for the probabilities of photon emission in a constant external electric field. *Physics of Complex Systems*, 3 (4), 167–175. <https://www.doi.org/10.33910/2687-153X-2022-3-4-167-175> EDN ORISSK

Received 26 September 2022; reviewed 10 October 2022; accepted 10 October 2022.

Funding: The work is supported by Russian Science Foundation (Grant No. 19-12-00042).

Copyright: © S. P. Gavrilov (2022). Published by Herzen State Pedagogical University of Russia. Open access under CC BY-NC License 4.0.

Abstract. In the case of an intense external electric field, there exist many transition channels corresponding to the violation of the vacuum stability. It was shown that depending on the setting of a problem there is a number of integral representations for the probabilities of one photon emission due to a constant electric field. These representations are the Fourier transformations of the product of two Weber parabolic cylinder functions that are solutions of the same differential equation. To simplify the study of the probabilities, we expressed such a Fourier transformation via the confluent hypergeometric function.

Keywords: Photon emission, quantum electrodynamics, strong external field, Schwinger effect, Fourier transformation

Introduction

In quantum electrodynamics with strong electric-like external fields (strong-field QED) there exists a vacuum instability due to the effect of real particle creation from the vacuum caused by external fields—the Schwinger effect (Schwinger 1951). A number of publications, reviews, and books are devoted to the effect itself and to developing different calculation methods in theories with unstable vacuum, see Refs. (Birrell, Davies 1982; Fedotov et al. 2022; Fradkin et al. 1991; Gelis, Tanji 2016; Greiner 1985; Grib et al. 1994; Ruffini et al. 2010) for a review. Until recently, problems related to particle creation from the vacuum were of a purely theoretical interest. This is related to the fact that, due to the presence of large gaps between the upper and the lower branches in the spectrum of the electron-positron pair, particle creation effects can be observed only in huge external electric fields of the magnitude of $E_c = m^2/e \approx 10^{16} \text{ V/cm}$. However, recent technological advances in laser science suggest that lasers may be able to reach the nonperturbative regime of pair production in the near future; see, e. g., the review (Fedotov et al. 2022) and references therein. Moreover, the situation has changed completely in recent years regarding applications to condensed matter physics: simulation of particle creation by external fields has become an observable effect in physics of graphene and similar nanostructures (say, in topological insulators and Weyl semimetals); see, e. g., the reviews (Sarma et al. 2011; Vafek, Vishwanath 2014). This is explained by the fact that low-energy single-electron dynamics in graphene monolayers at the charge neutrality point is described by the Dirac model, being a $2 + 1$ dimensional version of mass-

less QED with the Fermi velocity $v_F \approx 10^6$ m/s playing the role of the speed of light in relativistic particle dynamics (the reduced QED_{3,2}).

Due to the recent detection of an optical radiation in the graphene accompanying the creation of electron-hole pairs by a terahertz electric pulse (Oladyshkin et al. 2017), it becomes possible to make a comparison of the corresponding theoretical calculations with experiments. This terahertz pulse can be considered as slowly varying and locally approximated by a constant electric field. We see that the theory of photon emission under the action of a strong constant external electric field is of interest. Processes involving photon emission and annihilation in the presence of the vacuum instability are processes of higher order in radiative corrections. Adequate nonperturbative calculations with respect to the external field can be done using a general approach to QED with strong external fields (Fradkin et al. 1991) (based on the existence of special exact solutions of the Dirac equation with this field). The study of these processes in details is technically complicated. It can be seen from the number of calculations for particular cases: the emission of a photon in the case of a small instability in 3 + 1 QED (Nikishov 1971) and in graphene (Yokomizo 2014) and the probability of one photon emission from a single-electron state in the presence of a strong field in graphene (Aslyamova, Gavrilov 2020; Gavrilov, Gitman 2017). In the case of an intense external field, there exist many transition channels corresponding to the violation of the vacuum stability. By this reason, depending on the setting of a problem there is a number of integral representations for the probabilities of one photon emission due to a constant electric field. All of these representations are Fourier transformations of the product of two Weber parabolic cylinder functions (WPCFs) of some kind. Some of these integral representations with particular WPCFs were studied by A. I. Nikishov (Nikishov 1971). In the case of a strong field, the total probability of radiative processes are of interest. Therefore, integral representations with the number of other pairs of WPCFs for the probabilities are needed; see sections 3 and 4 in the book (Fradkin et al. 1991). In this article we study general properties of these representations that are quite similar in 3 + 1 QED and the reduced QED_{3,2}. Bearing in mind application of the obtained results in the framework of the theory of photon emission in nanostructures, we use representations of the QED_{3,2} in what follows.

Probabilities of emission

Adjustment of the general probability representations (Fradkin et al. 1991) to the reduced QED_{3,2} to describe one species of the Dirac fermions (small mass m and particle charge $q = -e$, $e > 0$ is the absolute value of the electron charge) in the graphene interacting with a constant external electric field $E > 0$ and photons is presented in Ref. (Gavrilov, Gitman 2017). We use notation $\bar{\mathbf{k}} = (\mathbf{k}, k_z)$ for three-dimensional wave vector of a photon. The two-dimensional vector $\mathbf{k} = (k_x, k_y)$ is a projection of $\bar{\mathbf{k}}$ on the graphene plane, $\omega = c|\bar{\mathbf{k}}|$, $\vartheta = 1, 2$ denotes a polarisation index, and ε is the relative permittivity (for the graphene suspended in a vacuum $\varepsilon = 1$).

The probability of one photon emission with given $\bar{\mathbf{k}}$ and ϑ from a single-electron (hole) state with given two-dimensional momentum $\mathbf{p} = (p_x, p_y)$ per unit frequency and solid angle is expressed as follows:

$$\frac{dP(\bar{\mathbf{k}}, \vartheta | \mathbf{p})}{d\omega d\Omega} = \frac{\alpha}{\varepsilon} \left(\frac{v_F}{c} \right)^2 \frac{\omega \Delta t_{st}^2}{(2\pi)^2} \left| M_{\mathbf{p}'\mathbf{p}}^\pm \right|^2 \Big|_{\mathbf{p}' = \mathbf{p} - \hbar \mathbf{k}}, \quad (1)$$

$$M_{\mathbf{p}'\mathbf{p}}^\pm = \mp \frac{S}{\Delta t_{st}} \int_{-\infty}^{\infty} \pm \bar{\psi}_{\mathbf{p}'}(t) \gamma \epsilon_{\bar{\mathbf{k}}\vartheta} \pm \psi_{\mathbf{p}}(t) e^{i\omega t} dt,$$

where $\Delta t_{st} = (|eE| v_F / \hbar)^{-1/2} \gg t_y$ is a big characteristic time scale and t_y is the microscopic time scale, $\epsilon_{\bar{\mathbf{k}}\vartheta}$ are mutual orthogonal unit polarisation vectors transversal to three-dimensional wave vector $\bar{\mathbf{k}}$, and $\gamma = (\gamma^1, \gamma^2)$ are 2×2 the Dirac γ -matrices,
 $\gamma^0 = \sigma^3, \gamma^1 = i\sigma^2, \gamma^2 = -i\sigma^1,$

where the σ^j are Pauli matrices. Solutions of the Dirac equation in 2 + 1 dimensions with a constant field for the case of graphene physics were studied in details in Ref. (Gavrilov, Gitman 1996). It was demonstrated that the corresponding in-set $\{\zeta\psi_n(t, \mathbf{r})\}$ and out-set $\{\bar{\zeta}\psi_n(t, \mathbf{r})\}$ can be chosen in the form:

$$\begin{aligned} \pm\psi_{\mathbf{p}}(t, \mathbf{r}) &= (i\hbar\partial_t + H^{\text{ext}}) \pm\Phi_{\mathbf{p}, \pm 1}(t, \mathbf{r}), \quad \pm\Phi_{\mathbf{p}, \pm 1}(t, \mathbf{r}) = e^{i\mathbf{p}\cdot\mathbf{r}/\hbar} \pm\varphi_{\mathbf{p}, \pm 1}(t)U_{\pm 1}, \\ \pm\bar{\psi}_{\mathbf{p}}(t, \mathbf{r}) &= (i\hbar\partial_t + H^{\text{ext}}) \pm\bar{\Phi}_{\mathbf{p}, \mp 1}(t, \mathbf{r}), \quad \pm\bar{\Phi}_{\mathbf{p}, \mp 1}(t, \mathbf{r}) = e^{i\mathbf{p}\cdot\mathbf{r}/\hbar} \pm\bar{\varphi}_{\mathbf{p}, \mp 1}(t)U_{\mp 1}, \end{aligned} \quad (2)$$

$$H^{\text{ext}} = v_F\gamma^0 (\gamma^1 (p_x - eEt) + \gamma^2 p_y + mv_F),$$

where U_s are constant orthonormalised spinors

$$U_{+1} = \frac{1}{\sqrt{2}} \begin{pmatrix} 1 \\ 1 \end{pmatrix}, \quad U_{-1} = \frac{1}{\sqrt{2}} \begin{pmatrix} 1 \\ -1 \end{pmatrix}.$$

The functions $\pm\varphi_{\mathbf{p}, s}(t)$ and $\pm\bar{\varphi}_{\mathbf{p}, s}(t)$ have the form of the WPCFs:

$$\begin{aligned} \bar{\varphi}_{\mathbf{p}, s}(t) &= CD_{v, -\frac{1+s}{2}} [\pm(1-i)\xi], \quad \varphi_{\mathbf{p}, s}(t) = CD_{-v, -\frac{1-s}{2}} [\pm(1+i)\xi], \quad v = \frac{i\lambda}{2}, \\ \xi &= \sqrt{\frac{v_F}{eE}} (eEt - p_x), \quad \lambda = \frac{v_F p_y^2 + m^2 v_F^3}{eE}, \quad C = (2eE\hbar v_F S)^{-1/2} \exp\left(-\frac{\pi\lambda}{8}\right), \end{aligned} \quad (3)$$

where S is the graphene area. An in-state $\pm\psi_{\mathbf{p}}(t, \mathbf{r})$ describes a particle/hole with a well-defined energy at the distant past. Similarly, an out-state $\pm\bar{\psi}_{\mathbf{p}}(t, \mathbf{r})$ describes a particle/hole with a well-defined energy at the distant future.

The probability of the one-photon emission with given $\bar{\mathbf{k}}$ and ϑ , which accompanies the production from the initial vacuum state of pairs of charged species with a given momentum \mathbf{p} per unit frequency and solid angle reads:

$$\frac{dP(\mathbf{p}; \mathbf{K}, \vartheta | 0)}{d\omega d\Omega} = \frac{\alpha}{\varepsilon} \left(\frac{v_F}{c}\right)^2 \frac{\omega \Delta t_{st}^2}{(2\pi)^2} |M_{\mathbf{p}'\mathbf{p}}^0|^2 \Big|_{\mathbf{p}' = \mathbf{p} - \hbar\mathbf{k}}, \quad (4)$$

$$M_{\mathbf{p}'\mathbf{p}}^0 = -\frac{S}{\Delta t_{st}} \int_{t_1}^{t_2} +\bar{\Psi}_{\mathbf{p}'}(t) \gamma \epsilon_{\mathbf{K}\vartheta} -\Psi_{\mathbf{p}}(t) e^{i\omega t} dt.$$

By inserting equation (3) into equation (2) and explicitly taking derivatives, we find that both $M_{\mathbf{p}'\mathbf{p}}^{\pm}$ and $M_{\mathbf{p}'\mathbf{p}}^0$ consist of the superposition of the following integrals:

$$\begin{aligned} Y_{j'j} &= \int_{-\infty}^{\infty} D_{-v'-j'} [-(1+i)(u - u_x/2)] D_{v-j} [-(1-i)(u + u_x/2)] e^{iu_0 u} du, \\ \tilde{Y}_{j'j} &= \int_{-\infty}^{\infty} D_{-v'-j'} [-(1+i)(u - u_x/2)] D_{-v-j} [-(1+i)(u + u_x/2)] e^{iu_0 u} du, \end{aligned} \quad (5)$$

where

$$u = \sqrt{\frac{v_F}{eE\hbar}} \left[eEt - \frac{1}{2}(p_x + p'_x) \right], \tag{6}$$

$$u_x = \sqrt{\frac{v_F}{eE\hbar}} (p'_x - p_x), \quad u_0 = \Delta t_{st} \omega .$$

Note that the probabilities of one-photon emission and absorption in any initial or final state can be expressed in similar representations with a pair of appropriate spinors $_{\pm} \psi_p(t, \mathbf{r})$ and $^{\pm} \psi_p(t, \mathbf{r})$.

Reduced integral representation

Integrals (5) can be simplified using the hyperbolic coordinates ρ and ϕ ,

$$\rho = \sqrt{|u_0^2 - u_x^2|}, \quad \tanh\phi = \frac{u_x}{u_0} \text{ if } u_0^2 - u_x^2 > 0 , \tag{7}$$

$$\tanh\phi = \frac{u_0}{u_x} \text{ if } u_0^2 - u_x^2 < 0 .$$

By applying Nikishov's approach (Nikishov 1971) we consider a more general case. Note that integrals (5) represent particular cases of the more general integrals

$$J_{\Lambda' \Lambda}^{\zeta' \zeta}(\rho, \phi) = \int_{-\infty}^{+\infty} du f_{\Lambda'}^{\zeta'}(u - u_x/2) f_{\Lambda}^{\zeta}(u + u_x/2) e^{iu_0 u} , \tag{8}$$

where $f_{\Lambda}^{\zeta}(z)$ are WPCFs satisfying the differential equation

$$\left(\frac{d^2}{dz^2} + z^2 + \Lambda \right) f_{\Lambda}^{\zeta}(z) = 0 , \tag{9}$$

and u_0 and u_x , defined by equation (6), are:

$$u_0 = \rho \cosh\phi, \quad u_x = \rho \sinh\phi \text{ if } u_0^2 > u_x^2,$$

$$u_0 = \rho \sinh\phi, \quad u_x = \rho \cosh\phi \text{ if } u_0^2 < u_x^2 \text{ and } u_x > 0, \tag{10}$$

$$u_0 = -\rho \sinh\phi, \quad u_x = -\rho \cosh\phi \text{ if } u_0^2 < u_x^2 \text{ and } u_x < 0.$$

The functions $f_{\Lambda}^{\zeta}(z)$ with different values of $\zeta = \pm$ are two linearly independent solutions of equation (9) with some complex parameters Λ . In particular,

$$J_{\Lambda' \Lambda}^{-+}(\rho, \phi) = Y_{j'j}, \quad \Lambda = \lambda + i(2j - 1), \quad \Lambda' = \lambda' + i(1 - 2j'),$$

$$J_{\Lambda' \Lambda}^{--}(\rho, \phi) = \tilde{Y}_{j'j}, \quad \Lambda = \lambda + i(1 - 2j), \quad \Lambda' = \lambda' + i(1 - 2j'). \tag{11}$$

Calculating the derivative of integral (8) with respect to the hyperbolic angle ϕ , we find:

$$\frac{\partial J_{\Lambda' \Lambda}^{\zeta \zeta}(\rho, \varphi)}{\partial \varphi} = W + \int_{-\infty}^{+\infty} i u_x f_{\Lambda'}^{\zeta'}(u - u_x / 2) f_{\Lambda}^{\zeta}(u + u_x / 2) e^{i u_0 u} du ,$$

$$W = \frac{u_0}{2} \int_{-\infty}^{+\infty} \left[f_{\Lambda'}^{\zeta'}(u - u_x / 2) \frac{\partial f_{\Lambda}^{\zeta}(z)}{\partial z} \Big|_{z=u+u_x/2} - \frac{\partial f_{\Lambda'}^{\zeta'}(z)}{\partial z} \Big|_{z=u-u_x/2} f_{\Lambda}^{\zeta}(u + u_x / 2) \right] e^{i u_0 u} du , \quad u_x = \frac{\partial u_0}{\partial \varphi} , \quad u_0 = \frac{\partial u_x}{\partial \varphi} .$$

Integrating by parts and neglecting boundary terms, we can transform W into the following form:

$$W = \frac{i}{2} \int_{-\infty}^{+\infty} \left[f_{\Lambda'}^{\zeta'}(u - u_x / 2) \frac{\partial^2 f_{\Lambda}^{\zeta}(z)}{\partial z^2} \Big|_{z=u+u_x/2} - \frac{\partial^2 f_{\Lambda'}^{\zeta'}(z)}{\partial z^2} \Big|_{z=u-u_x/2} f_{\Lambda}^{\zeta}(u + u_x / 2) \right] e^{i u_0 u} du . \tag{12}$$

Using equation (9) in integral (12), we find:

$$\frac{\partial J_{\Lambda' \Lambda}^{\zeta \zeta}(\rho, \varphi)}{\partial \varphi} = \frac{i}{2} (\Lambda' - \Lambda) J_{\Lambda' \Lambda}^{\zeta \zeta}(\rho, \varphi). \tag{13}$$

Solutions of this equation are:

$$J_{\Lambda' \Lambda}^{\zeta \zeta}(\rho, \varphi) = e^{\frac{i}{2}(\Lambda' - \Lambda)(\varphi - \varphi_0)} J_{\Lambda' \Lambda}^{\zeta \zeta}(\rho, \varphi_0), \tag{14}$$

where $\varphi_0 = 0$ if $u_0^2 > u_x^2$ and we choose an appropriate value for φ_0 (sign of φ_0 is the same with u_x) if $u_0^2 < u_x^2$. The φ dependence of integrals (8) can be factorised with the help of equation (14). In a more interesting case, $u_0^2 > u_x^2$, we get:

$$Y_{j'j} = \exp \left[\left(i \frac{\lambda' - \lambda}{2} + j' + j - 1 \right) \varphi \right] J_{j',j}(\rho), \tag{15}$$

$$J_{j',j}(\rho) = \int_{-\infty}^{\infty} D_{-v'-j'} [-(1+i)u] D_{v-j} [-(1-i)u] e^{i \rho u} du;$$

$$\tilde{Y}_{j'j} = \exp \left[\left(i \frac{\lambda' - \lambda}{2} + j' - j \right) \varphi \right] \tilde{J}_{j',j}(\rho), \tag{16}$$

$$\tilde{J}_{j',j}(\rho) = \int_{-\infty}^{\infty} D_{-v'-j'} [-(1+i)u] D_{-v-j} [-(1+i)u] e^{i \rho u} du.$$

If $u_0^2 > u_x^2$, we assume that $\varphi_0=0$ and use the notation $J_{\Lambda' \Lambda}^{\zeta \zeta}(\rho) = J_{\Lambda' \Lambda}^{\zeta \zeta}(\rho, 0)$ in what follows. This function satisfies the differential equation (Nikishov 1971)

$$\left[\frac{d^2}{d\rho^2} + \frac{1}{\rho} \frac{d}{d\rho} + \frac{(\Lambda - \Lambda')^2}{4\rho^2} + \frac{\rho^2}{4} - \frac{\Lambda + \Lambda'}{2} \right] J_{\Lambda' \Lambda}^{\zeta \zeta}(\rho) = 0 . \tag{17}$$

This fact can be verified by performing integrations by parts taking into account equation (9). The differential equation (17) can be reduced to a confluent hypergeometric equation. Using two linearly independent solutions of such an equation, we find general solution of the differential equation (17)

$$J_{\Lambda'\Lambda}^{\zeta\zeta}(\rho) = e^{-\eta/2} \left[C_1 \eta^{i\beta} \Phi\left(\frac{i\Lambda}{2} + \frac{1}{2}, 1 + 2i\beta; \eta\right) + C_2 \eta^{-i\beta} \Phi\left(\frac{i\Lambda'}{2} + \frac{1}{2}, 1 - 2i\beta; \eta\right) \right], \tag{18}$$

$$\eta = -i\rho^2/2, \quad \beta = (\Lambda - \Lambda')/4,$$

where the C_1 and C_2 are some undetermined coefficients, which must be fixed by appropriate boundary conditions so that solution (18) corresponds to the original integral (8).

The confluent hypergeometric function $\Phi(a, c; \eta)$ is entire in η and a , and is a meromorphic function of c . Note that $\Phi(a, c; 0) = 1$. WPCFs are entire functions of Λ and Λ' . We can see that the integrals $J_{\Lambda'\Lambda}^{\zeta\zeta}(\rho)$ are entire functions of Λ and Λ' and meromorphic functions of $\Lambda - \Lambda'$. Then we can find a boundary condition $J_{\Lambda'\Lambda}^{\zeta\zeta}(\rho)$ at $\rho \rightarrow 0$ for some convenient values of j and j' . The remaining integrals $J_{\Lambda'\Lambda}^{\zeta\zeta}(\rho)$ can be obtained by extending domains of Λ and Λ' by an analytic continuation.

Let us start with $\tilde{J}_{0,0}(\rho)$ given by equation (16). This integral can be represented as a solution of equation (17) where $\Lambda' = \lambda' + i$ and $\Lambda = \lambda + i$. The coefficients C_1 and C_2 in equation (18) can be fixed by a comparison with the $\rho \rightarrow 0$ limit of integral (16). Let us first represent this integral as follows:

$$\begin{aligned} \tilde{J}_{0,0}(\rho) &= F^0 + F^+ + F^-, \quad F^+ = \int_0^\infty f^+(u) e^{i\rho u} du, \quad F^- = \int_{-\infty}^0 f^-(u) e^{i\rho u} du, \\ F^0 &= \int_0^\infty f(u) [f(u) - f^+(u)] e^{i\rho u} du + \int_{-\infty}^0 f(u) [f(u) - f^-(u)] e^{i\rho u} du, \end{aligned} \tag{19}$$

$$f(u) = D_{-v'}[-(1+i)u] D_{-v}[-(1+i)u],$$

where $f^\pm(u) = f(u)|_{u \rightarrow \pm\infty}$. It can be seen that function (18) is reduced to the oscillations $C_1 \eta^{i\beta} + C_2 \eta^{-i\beta}$ as $\rho \rightarrow 0$. Then ρ -independent terms do not contribute to the integrals F^0 and F^\pm . Taking into account that $\lim_{\rho \rightarrow 0} F^0$ and $\lim_{\rho \rightarrow 0} F^\pm$ do not depend on ρ , we see that the oscillation terms of F^\pm are only essential. Using Bateman's relations (8.2.(7)) and (8.4.(1)) (Bateman 1953), we find:

$$\begin{aligned} \tilde{J}_{0,0}(\rho) &= \sqrt{\pi} e^{i\pi(v+v'-1)/4} \left[e^{i\pi v/2} \frac{\Gamma(v-v')}{\Gamma(v)} \left(\frac{\rho}{\sqrt{2}}\right)^{v-v} \right. \\ &\quad \left. + e^{i\pi v'/2} \frac{\Gamma(v'-v)}{\Gamma(v')} \left(\frac{\rho}{\sqrt{2}}\right)^{v-v'} \text{ as } \rho \rightarrow 0 \right]. \end{aligned} \tag{20}$$

Comparing equations (18) and (20), we obtain:

$$C_1 = \sqrt{\pi} e^{i\pi(v+v'-1/2)/2} \frac{\Gamma(v'-v)}{\Gamma(v')}, \quad C_2 = \sqrt{\pi} e^{i\pi(v+v'-1/2)/2} \frac{\Gamma(v-v')}{\Gamma(v)}. \tag{21}$$

Using Bateman's relation (6.5.(7)) (Bateman 1953), we represent the function given by equations (18) and (21) as

$$\tilde{J}_{0,0}(\rho) = \sqrt{\pi} e^{i\pi(v+v'-1/2)/2} e^{-\eta/2} \eta^{(v-v')/2} \Psi(v, 1 + v - v'; \eta), \tag{22}$$

where $\Psi(v, 1 + v - v'; \eta)$ is the confluent hypergeometric function,

$$\Psi(v, 1+v-v'; \eta) = \frac{\Gamma(v'-v)}{\Gamma(v')} \Phi(v, 1+v-v'; \eta) + \frac{\Gamma(v-v')}{\Gamma(v)} \eta^{v'-v} \Phi(v', 1+v'-v; \eta). \quad (23)$$

Using the transformation $v \rightarrow v+j$ and $v' \rightarrow v'+j'$ in equation (22), we obtain the final form

$$\tilde{J}_{j',j}(\rho) = e^{i\pi(v+v'+j+j')/2} I_{j',j}(\rho), \quad (24)$$

$$I_{j',j}(\rho) = \sqrt{\pi} \exp \left[\left(\ln \frac{\rho}{\sqrt{2}} - \frac{i\pi}{4} \right) (v-v'+j-j') + i \frac{\rho^2}{2} - \frac{i\pi}{4} \right] \times \Psi \left(v+j, 1+v-v'+j-j'; -i \frac{\rho^2}{2} \right). \quad (25)$$

The integral $J_{j',j}(\rho)$ given by equation (15) can be represented as the solution of equation (17) where $\Lambda' = \lambda' + i(1-2j')$ and $\Lambda = \lambda + i(2j-1)$. Using Bateman's relation (8.2.(6)) (Bateman 1953), we transform one of the WPCFs in equation (15) to obtain convenient representations:

$$J_{j',j}(\rho) = \frac{\Gamma(v-j+1)}{\sqrt{2\pi}} \left[e^{i\pi(v-j)/2} \tilde{J}_{j',1-j}(\rho) + e^{-i\pi(v-j)/2} J'_{j',1-j}(\rho) \right], \quad (26)$$

$$J'_{j',1-j}(\rho) = \int_{-\infty}^{\infty} D_{-v'-j'} \left[-(1+i)u \right] D_{-v+j-1} \left[(1+i)u \right] e^{i\rho u} du, \quad (27)$$

where $\tilde{J}_{j',1-j}(\rho)$ is given by equation (24). The integral $J_{j',1-j}(\rho)$ is represented by function (18) where some coefficients C'_1 and C'_2 can be fixed by the comparison with $\rho \rightarrow 0$ limit of the integral $J_{j',1-j}(\rho)$.

Let us start with $J_{0,0}(\rho)$, where $\Lambda' = \lambda' + i$ and $\Lambda = \lambda + i$. In this case, function (18) takes the form $C'_1 \eta^{i\beta} + C'_2 \eta^{-i\beta}$ as $\rho \rightarrow 0$. Hence all ρ -independent terms of $J_{0,0}(\rho)$ given by equation (27) can be ignored at $\rho \rightarrow 0$ limit and only the oscillation terms of the following integrals

$$G^+ = \int_0^{\infty} g^+(u) e^{i\rho u} du, \quad F^- = \int_{-\infty}^0 g^-(u) e^{i\rho u} du, \quad g^{\pm}(u) = g(u) \Big|_{u \rightarrow \pm\infty}, \quad (28)$$

$$g(u) = D_{-v'} \left[-(1+i)u \right] D_{-v} \left[(1+i)u \right]$$

are essential. Using Bateman's relations (8.2.(7)) and (8.4.(1)) (Bateman 1953), we find:

$$J'_{0,0}(\rho) = \sqrt{\pi} e^{i\pi(v'-v-1/2)/2} \left[e^{i\pi(v-v')/4} \frac{\Gamma(v-v')}{\Gamma(v)} \left(\frac{\rho}{\sqrt{2}} \right)^{v'-v} + e^{-i\pi(v-v')/4} \frac{\Gamma(v'-v)}{\Gamma(v')} \left(\frac{\rho}{\sqrt{2}} \right)^{v-v'} \text{ as } \rho \rightarrow 0 \right]. \quad (29)$$

Comparing equations (18) and (29), we obtain:

$$C'_1 = \sqrt{\pi} e^{i\pi(v'-v-1/2)/2} \frac{\Gamma(v'-v)}{\Gamma(v')}, \quad C'_2 = \sqrt{\pi} e^{i\pi(v'-v-1/2)/2} \frac{\Gamma(v-v')}{\Gamma(v)}. \quad (30)$$

Using Bateman's relation (6.5.(7)) (Bateman 1953), the function given by equations (18) and (30) can be represented as:

$$J'_{0,0}(\rho) = \sqrt{\pi} e^{i\pi(v'-v-1/2)/2} e^{-\eta/2} \eta^{(v-v')/2} \Psi(v, 1+v-v'; \eta). \quad (31)$$

Using the transformations $v \rightarrow v+1-j$ and $v' \rightarrow v'+j$ in equation (31), we obtain the following representation for integral (27):

$$J'_{j',1-j}(\rho) = e^{-i\pi(v-v'+1-j-j')/2} I_{j',1-j}(\rho), \quad (32)$$

where $I_{j',j}(\rho)$ is given by equation (25). Substituting representations (24) and (32) into equation (26), we find the final form:

$$J_{j',j}(\rho) = (-1)^j \sqrt{\frac{2}{\pi}} \Gamma(v-j+1) \exp[i\pi(v'+j-1)/2] \sinh \frac{\pi\lambda}{2} I_{j',1-j}(\rho), \quad (33)$$

where Γ is the gamma-function.

Conclusion

It was shown that integral representations for the probabilities of one photon emission due to a constant electric field are presented as Fourier transformations of the product of two WPCFs of some kind. We have expressed such a Fourier transformation by the confluent hypergeometric function. It helps greatly in studies of the probabilities of one photon emission that will be presented in a following publication elsewhere.

Conflict of Interest

The author declares that there is no conflict of interest, either existing or potential.

References

- Aslyamova, I. N., Gavrilov, S. P. (2020) Characteristics of high-frequency emission of an electron in graphene in a constant electric field. *Physics of Complex Systems*, 1 (2), 78–84. <https://doi.org/10.33910/2687-153X-2020-1-2-78-84> (In English)
- Birrell, N. D., Davies, P. C. W. (1982) *Quantum fields in curved space*. Cambridge: Cambridge University Press, 352 p. (In English)
- Bateman, H. (1953) *Higher transcendental functions. Vol. I–II* New York: McGraw-Hill Publ., 297 p. (In English)
- Fedotov, A., Ilderton, A., Karbstein, F. et al. (2022) *Advances in QED with intense background fields*. [Online]. Available at: <https://doi.org/10.48550/arXiv.2203.00019> (accessed 28.02.2022). (In English)
- Fradkin, E. S., Gitman, D. M., Shvartsman, S. M. (1991) *Quantum electrodynamics with unstable vacuum*. Berlin: Springer-Verlag, 288 p. (In English)
- Gavrilov, S. P. Gitman, D. M. (1996) Vacuum instability in external fields. *Physical Review D*, 53 (12), 7162–7175. <https://doi.org/10.1103/PhysRevD.53.7162> (In English)
- Gavrilov, S. P. Gitman, D. M. (2017) Radiative processes in graphene and similar nanostructures at strong electric fields. *Russian Physics Journal*, 59 (11), 1870–1874. <https://doi.org/10.1007/s11182-017-0989-7> (In English)
- Gelis, F., Tanji, N. (2016) Schwinger mechanism revisited. *Progress in Particle and Nuclear Physics*, 87, 1–49. <https://doi.org/10.1016/j.pnpnp.2015.11.001> (In English)
- Greiner, W. (1985) *Quantum electrodynamics of strong fields*. Berlin: Springer-Verlag, 594 p. https://doi.org/10.1007/3-540-15653-4_3 (In English)
- Grib, A. A., Mostepanenko, V. M., Mamaev, S. G. (1994) *Vacuum quantum effects in strong fields*. Saint Petersburg: Friedmann Laboratory Publ., 362 p. (In English)
- Nikishov, A. I. (1971) Quantum processes in a constant electric fields. *Soviet Physics JETP*, 32 (4), 690–694. (In English)
- Oladyshkin, I. V., Bodrov, S. B., Sergeev, Yu. A. et al. (2017) Optical emission of graphene and electron-hole pair production induced by a strong terahertz field. *Physical Review B*, 96 (15), article 155401. <https://doi.org/10.1103/PhysRevB.96.155401> (In English)
- Ruffini, R., Vereshchagin, G., Xue, S. (2010) Electron–positron pairs in physics and astrophysics: from heavy nuclei to black holes. *Physics Reports*, 487 (1-4), 1–140. <https://doi.org/10.1016/j.physrep.2009.10.004> (In English)

- Sarma, S. D., Adam, S., Hwang, E. H., Rossi, E. (2011) Electronic transport in two-dimensional graphene. *Reviews of Modern Physics*, 83 (2), 407–470. <https://doi.org/10.1103/RevModPhys.83.407> (In English)
- Schwinger, J. (1951) On gauge invariance and vacuum and vacuum polarization. *Physical Review*, 82 (5), 664–679. (In English)
- Vafek, O., Vishwanath, A. (2014) Dirac fermions in solids: From High- T_c cuprates and graphene to topological insulators and Weyl semimetals. *Annual Reviews of Condensed Matter Physics*, 5, 83–112. <https://doi.org/10.1146/annurev-conmatphys-031113-133841> (In English)
- Yokomizo, N. (2014) Radiation from electrons in graphene in strong electric field. *Annals of Physics*, 351, 166–199. <https://doi.org/10.1016/j.aop.2014.08.024> (In English)



Check for updates

Theoretical physics.
Physics of atoms and molecules

UDC 530.182

EDN JFBHQD

<https://www.doi.org/10.33910/2687-153X-2022-3-4-176-185>

Entropy and dimension of a chaotic attractor depending on the control parameter

A. V. Liaptsev^{✉1}

¹ Herzen State Pedagogical University of Russia, 48 Moika Emb., Saint Petersburg 191186, Russia

Author

Alexander V. Liaptsev, ORCID: [0000-0002-8702-9062](https://orcid.org/0000-0002-8702-9062), e-mail: Lav@herzen.spb.ru

For citation: Liaptsev, A. V. (2022) Entropy and dimension of a chaotic attractor depending on the control parameter. *Physics of Complex Systems*, 3 (4), 176–185. <https://www.doi.org/10.33910/2687-153X-2022-3-4-176-185> EDN JFBHQD

Received 2 September 2022; reviewed 30 September 2022; accepted 30 September 2022.

Funding: The study did not receive any external funding.

Copyright: © A. V. Liaptsev (2022). Published by Herzen State Pedagogical University of Russia. Open access under [CC BY-NC License 4.0](https://creativecommons.org/licenses/by-nc/4.0/).

Abstract. The dependence of the entropy and dimension of the chaotic attractor on the control parameter is investigated by the numerical experiment. Calculations are carried out for one of the simplest systems described by nonlinear equations of dynamics—a rotator driven by an external periodic field. Here, regular and chaotic solutions alternate when the control parameter changes. The numerical experiment shows that the dimension of the chaotic attractor and, as a consequence, its entropy change significantly when the control parameter is in the ranges where, due to intermittency, the transition from chaotic motion to regular motion occurs.

Keywords: nonlinear dynamics, strange attractor, chaotic attractor, probability density, chaos, intermittency, rotator

Introduction

In systems described by equations of nonlinear dynamics, in the presence of dissipation, both regular and chaotic movements are possible (Gonchenko et al. 2017; Schuster, Just 2005). In the case of regular movements, the trajectory of the system in phase space is a closed line, or degenerates into a point. Such sets of points are attractors. In the case of chaotic motion, the trajectory of motion is an infinite non-intersecting line. At the same time, the region in the phase space that restricts the movement of the system is constantly narrowing over time, which means that the phase trajectory also tends to a certain attractor, which is called a chaotic or strange attractor. In this case, the state of the system can be described in terms of probability. It means that one can define a probability density that determines the probability of finding the system in some given region of space, similarly to the probability density in systems described by statistical physics or quantum mechanics (Kuznetsov 2006; Liapzev 2019).

A distinctive feature of the chaotic attractor is that it irregularly fills the region of phase space. The correct definition of the chaotic attractor shows that it has a fractional dimension and it is smaller than the dimension of the phase space (Malinetsky, Potapov 2000). A salient aspect of the nonlinear dynamic systems in question is the dependence of the character of motion on some parameters of the problem, which are called control parameters. In particular, with an adiabatic change of any of these parameters, the system can jump from chaotic to regular motion and vice versa. Since in the case of regular motion the attractor is a closed line, its dimension is equal to one. This means that, generally speaking, a change in the control parameter leads to a change in the dimension of the attractor.

Since the measure of chaos is entropy, it is possible to correctly define the concept of entropy for a system whose motion is described by a chaotic attractor (see, for example, (Malinetsky, Potapov 2000)). At the same time, it is natural to assume that the regular movement of the system should manifest itself, at least entropy. It follows from the above that the entropy of the system described by the chaotic attractor should also depend on the control parameters.

It is unlikely that analytical research methods alone are sufficient for the general study of the dependence of the dimension and entropy of chaotic attractors. This makes a numerical experiment useful, at least, for the simplest dynamical systems. One of such systems is a rotator (a system with one-dimensional rotational motion), driven by an external periodic field. The control parameter for such a system is the amplitude of the external field. The purpose of this article is to use numerical methods to investigate the dependence of the entropy and dimension of a chaotic attractor on the control parameters in such systems.

Problem statement. Equation of motion

Consider an electric dipole that can make a one-dimensional rotation (Fig. 1). Such a real system consists of two oppositely charged balls of the same mass connected by a non-conducting rod fixed on a hinge.

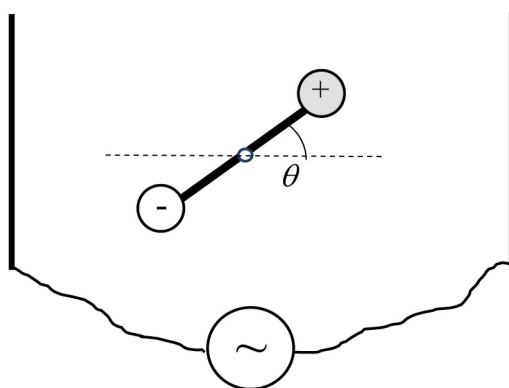


Fig. 1. Rotator scheme

The effect of an external harmonic field can be taken into account by placing such a system between the plates of the capacitor to which the alternating voltage is applied. Note that a similar model can be used to describe the rotational motion of a molecule in a microwave field, since the rotational motion in a good approximation can be described in the framework of a quasi-classical approximation.

We also assume that the rotation is decelerated with the viscous friction force, which is proportional to the angular velocity of rotation. Then the dynamic equation describing the motion has the form:

$$I \ddot{\theta} = qE_0 \sin \theta \cos(\omega t) - \lambda \dot{\theta},$$

where I is the moment of inertia of the dipole, q is the absolute value of charge of the balls, E_0 and ω is the intensity and frequency of the external field, λ is the coefficient of proportionality between the moment of friction and the angular velocity. Here and further the point denotes the derivative of the variable t . To simplify the equation, we perform a large-scale transformation of the time variable. $t' = \omega t$. Then the equation of motion takes the form:

$$\ddot{\theta} + \gamma \dot{\theta} = f \theta \cos t \quad (1)$$

where $\gamma = \frac{\lambda}{I\omega}$, $f = \frac{qE_0}{I\omega^2}$ (for simplicity, in what follows t will be used instead of t'). Note that this equation and the corresponding Poincaré cross section pattern were considered in the monograph (Sagdeev et al. 1988), and the formulation of similar quantum mechanical problem in the absence

of dissipation is considered in (Stockmann 1999), where, in particular, it was noted that “systems with harmonic dependence on time are not too popular among theorists”.

The differential equation of the second order (1) is reduced to an autonomous system of three differential equations of the first order:

$$\begin{aligned} \dot{\theta} &= p, \\ \dot{p} &= f \sin \theta \cos \tau - \gamma p, \\ \dot{\tau} &= 1. \end{aligned} \tag{2}$$

The variables θ, p and τ form a three-dimensional phase space. This is the minimum value of dimension for which the trajectory can tend to a chaotic attractor, similar to the Lorenz attractor (see, for example, (Grinchenko et al. 2007)). At the same time, depending on the control parameter f , the solution can be both regular and chaotic. Parameter γ characterizing the dissipation, is usually assumed to be small. However, namely its difference from zero determines the tendency of the trajectory in the phase space to the attractor. Unlike the time variable, the variable τ can be considered as periodic with a period of 2π . Taking into account the periodicity of the variable θ , it is convenient to consider the trajectory in the phase space as a line “wound” on the torus (Fig. 2).

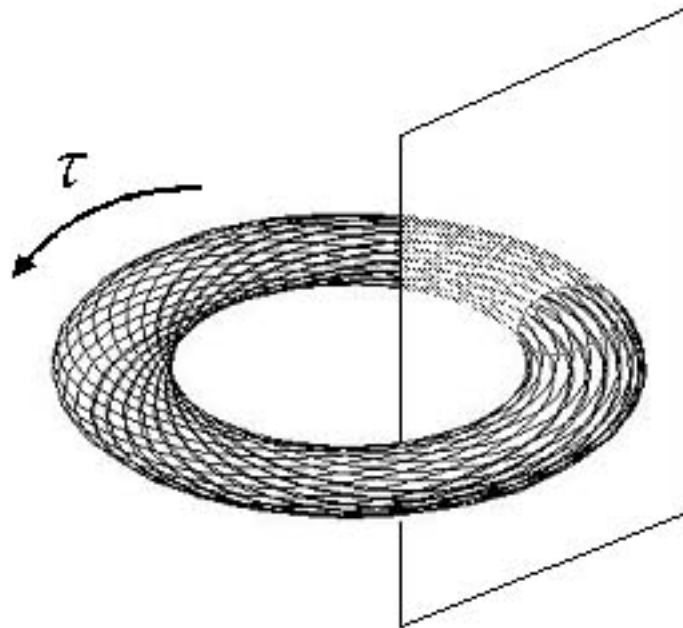


Fig. 2. The trajectory of motion in phase space

The cross section of such a torus by a plane is a Poincaré cross section; the corresponding set of points is a fractal.

The control parameter in equation (1), or in the system of equations (2) is the parameter f . Depending on the values of this parameter, the solution can be regular, in which the trajectory of motion in phase space is a closed line taking into account the periodicity of the variables θ and τ , or chaotic, in which the trajectory is an infinite open line. In the first case, the attractor is a limit cycle, and in the second, a chaotic (“strange” in Lorenz’s terminology) attractor.

Probabilistic approach

In the case of chaotic motion, the state of the system can be described in the language of probability, for which it is possible to introduce the concept of probability density (Liapzev 2019). Let us define a density probability distribution $\rho(\tau, \theta, p)$ as follows: for a given value τ , the value $\Delta w = \rho(\tau, \theta, p) \Delta\tau \Delta\theta \Delta p$ is

equal to the probability that the trajectory of the system passes in the region $[\tau, \tau = \Delta\tau; \theta, \theta = \Delta\theta; p, p + \Delta p]$ and the normalization condition is set:

$$\int_0^{2\pi} d\theta \int_{-\infty}^{\infty} dp \rho(\tau, \theta, p) = 1, \quad \forall \tau. \tag{3}$$

As shown in (Liaptsev 2019) (see also (Kuznetsov 2006)), the probability density satisfies the partial differential equation of the first order. In particular, for the system considered in this paper, the equation has the form:

$$\frac{\partial \rho}{\partial \tau} + p \frac{\partial \rho}{\partial \theta} + f \sin \theta \cos \tau \frac{\partial \rho}{\partial p} - \gamma \frac{\partial \rho}{\partial p} = 0. \tag{4}$$

Note that the density of the probability distribution can be approximately obtained by a numerical experiment. To do this, note that the variables τ and θ are limited to the range $[0, 2\pi]$. It is not difficult to show (Liaptsev 2019) that for any parameter values, the variable p is limited to a certain range $[-p_{\max}, p_{\max}]$. To calculate the probability density, each of the variable intervals can be divided into identical cells. Denote the corresponding numbers of cells by N_τ, N_θ and N_p . As a result, the entire region of the phase space is divided into $N_\theta N_p N_\tau$ identical cells. Let τ_i be the values of the variable τ , lying in the middle of each of the N_τ intervals. To numerically find the probability density, some initial values $\theta(0)$ and $p(0)$ are selected and then numerical solutions $\theta(t_j), p(t_j)$ are found, where the values of t_j lie in the interval $[0, dT]$ and are equal in modulus 2π to the values of τ_i . For each of the t_j values, a cell in the phase space is determined, into which the values $\theta(t_j), p(t_j)$ and τ_i fall, as a result of which the values of the numbers of points in each of the cells are calculated. Next, the values $\theta(dT)$ and $p(dT)$ are chosen as the initial ones, and solutions $\theta(t_j), p(t_j)$ are found, where the values of t_j lie in the interval $[dT, 2dT]$, as a result of which the numbers of points in each of the cells are supplemented. After repeating such iterations many times and after normalization to one, the probability density is found in the form of an array $\rho(\tau_p, \theta_p, p_k)$.

Calculation of the dimension and entropy of a chaotic attractor

To calculate entropy, we use the formula (for details, see, for example, (Malinetsky, Potapov 2000)):

$$S = -\sum_i w_i \ln(w_i), \tag{5}$$

where the index i is the cell number, w_i is the probability that the system will be in the region of the phase space bounded by the i -th cell. The entropy determined this way depends on the size of the cells, and, when these sizes tend to zero, (the number of cells tends to infinity) it has no finite limit. Indeed, the probability of finding a system in cell i is expressed in terms of probability density:

$$w_i = \rho_i \Delta V,$$

where ρ_i is the probability density for the i^{th} cell and ΔV is the volume of the cell. If the characteristic cell size (in one dimension) is ε , then with the dimension of the phase space n , the cell volume is $\Delta V \approx \varepsilon^n$ and for entropy we obtain the expression:

$$S \cong -\sum_i \rho_i \Delta V (\ln \rho_i + \ln \Delta V) = -\sum_i w_i \ln \rho_i - \sum_i p_i \ln(\varepsilon^n) = -\langle \ln \rho \rangle - n \ln \varepsilon.$$

The first term has a finite limit at $\varepsilon \rightarrow 0$, let us denote it by S_0 ; the second term increases as a logarithm. Thus, for small values of ε , the expression for entropy can be written as:

$$S \approx S_0 - n \ln \varepsilon. \tag{6}$$

Expression (6) also turns out to be valid in the case when the dimension of the set n , in which the phase trajectory lies, turns out to be fractional, which occurs when the state of the system tends to a chaotic attractor.

Note that in numerical calculations, the tendency of $\varepsilon \rightarrow 0$ is provided by the tendency of a number of cells to infinity. In particular, in the case we are considering, we can put $N_\theta = N_p = N_\tau = N$. Then the dependence ε on N can be represented as: $\varepsilon = \varepsilon_0/N$, where ε_0 is a constant. As a result, the expression for entropy can be written as:

$$S(N) \approx S_0 - n \ln \varepsilon_0 + n \ln N. \tag{7}$$

Expression (7) can be used to numerically determine the dimension of a chaotic attractor. For a given value of N , the probability p_i can be defined as the number of points in i cell relative to the number of points in all cells. Using formula (5) we obtain the entropy $S(N)$. By varying the value of N , one can get the dependence $S(\ln N)$. For large values of N , the graph should approach a straight line, the tangent of the inclination angle of which is equal to the dimension of the attractor n .

Note that definition (5) for the entropy of the attractor can be extended to the case of regular motion, when the attractor is a limit cycle. The trajectory in phase space is a line, a point on which can be characterized by the value τ (Fig. 1). The period of regular movement is a multiple of the period of external influence. Now let the entire phase space be divided into N^3 cells (N in each dimension). With a multiplicity equal to q , each value of τ_i corresponds to q cells through which the phase trajectory passes. Thus, for one period, Nq cells are filled with one point, and for M periods, each of these cells will be filled with M points. The probability that the system is located at one of these points is equal to $w = \frac{M}{MNq} = \frac{1}{Nq}$. The probability of being at any other point is zero. Thus,

$$S(N) = - \sum_{i=1}^{Nq} \frac{1}{Nq} \ln \left(\frac{1}{Nq} \right) = \ln q + \ln N .$$

This expression coincides with expression (7), if we take into account that the dimension of the attractor is $n=1$ and put:

$$S_0 - n \ln \varepsilon_0 = \ln q. \tag{8}$$

In this paper, the dimension of the chaotic attractor was calculated as follows. In each dimension (variables τ , θ and p), the range of acceptable values was divided into $N = 90$ identical intervals. Thus, the phase space was divided into 729.000 cells. The time intervals at which the system of equations (2) was solved were chosen equal to $dT = 20\pi$, that is, 10 periods of external influence. At each interval, a three-dimensional array $\rho(N, \tau_p, \theta_p, p_k)$ with a dimension of $90 \times 90 \times 90$ was filled. The calculation was carried out over 10,000 dT intervals. At the same time, by combining 8 nearest cells (2 in each dimension), an array $\rho(N/2, \tau_p, \theta_p, p_k)$ with dimension $45 \times 45 \times 45$ was calculated and by combining 9 nearest cells of the array $\rho(N, \tau_p, \theta_p, p_k)$ (3 in each dimension), an array was calculated $\rho(N/3, \tau_p, \theta_p, p_k)$ with dimension $30 \times 30 \times 30$. Further, using these arrays, the entropies $S(N)$, $S(N/2)$, $S(N/3)$ were calculated using formula (5). The calculation shows that the linear dependence of entropy on \ln (formula (7)) is performed in a good approximation. On the $S(\ln N)$ graph, the points lie almost on the same straight line, and the values of the slope angle tangents calculated from the points with $N = 90$ and $N = 45$ differ from the values calculated from the points with $N = 90$ and $N = 30$ by about 1%. In this paper, the calculation was carried out for a parameter characterizing the dissipation of $\gamma = 0.1$ in the range of values of the control parameter $f \in [2.159, 22.61]$, for a value of $N = 90$. In the case of chaotic motion, the average values of $S(90)$ and n were approximately equal to 12 and 2.5, respectively. However, in some areas of the values of f , significant deviations from these average values were observed, which made it possible to calculate the values of the parameters S_0 and ε_0 that are included into expression (7).

Dependence of the entropy and dimension of the attractor on the control parameter

As mentioned above, the areas of values of the control parameter, at which chaotic motion is realized, alternate with areas of regular motion. In the case of a regular solution, the numerical calculation of entropy is fully consistent with expression (8). The results of the calculation in one of the regions of chaotic motion $f \in [2.159, 11.28]$ are shown in Fig. 3.

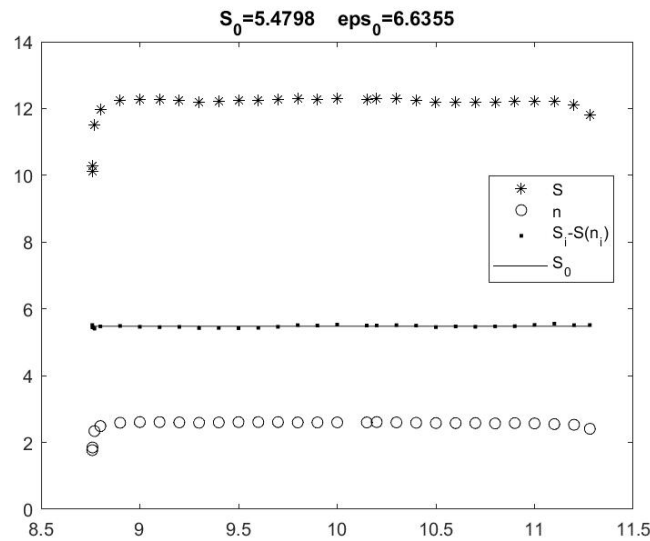


Fig. 3. Calculated values of entropy (upper graph) and dimension of the attractor (lower graph) depending on the control parameter

As can be seen from the figure, significant (up to 30%) changes in the values of S and n are observed at the border of the plot (upper and lower graphs). These changes are due to the fact that at the borders there is a transition from chaotic movement to regular movement through intermittency. This means that during sufficiently large time intervals (hundreds of periods of external influence), the movement is periodic, after which there is a transition to chaotic movement. Similar transitions between order and chaos are observed in various nonlinear systems (Grinchenko et al. 2017). A simultaneous decrease in the values of n and S at the boundary of the interval suggests that a decrease in entropy is due to a decrease in the dimension of the attractor in accordance with expression (7). This means that the values of $\{F_i, S_i, n_i\}$ obtained as a result of the numerical experiment can be approximated by the expression:

$$S_i = S_0 - n_i \ln(\epsilon_0) + n_i \ln N, \tag{9}$$

where the i index numbers the points on the graph (Fig. 3), and according to the calculations $N = 90$. Using the least squares method, it is possible to find the parameters S_0 and ϵ_0 , at which the results of the numerical experiment are best described by expression (9). The least squares method also allows one to estimate the error with which the parameters are calculated. The results of such calculations for several ranges of values of f , within which the movement is chaotic, are shown in Table 1.

Table 1. Estimation of the parameters ϵ_0 and S_0 (formula 9) based on the results of a numerical experiment

| Range | | S_0 | δS_0 (%) | ϵ_0 | $\delta \epsilon_0$ (%) |
|------------|------------|-------|------------------|--------------|-------------------------|
| f_{\min} | f_{\max} | | | | |
| 2.165 | 3.76 | 3.4 | 15 | 3.1 | 38 |
| 7.471 | 8.32 | 5.8 | 5 | 6.9 | 6 |
| 8.77 | 11.28 | 5.5 | 5 | 6.8 | 6 |
| 16.875 | 18.794 | 5.5 | 9 | 6.7 | 11 |
| 19.35 | 22.61 | 5.9 | 6 | 7.8 | 7 |

The results of such an approximation for the range $f \in [2.159, 11.28]$ are clearly shown in Fig. 3. Expression (9) can be represented as: $S_0 = S_i + n_i \ln(\varepsilon_0) - n_i \ln N$. The points on the middle graph correspond to the values $S_i + n_i \ln(\varepsilon_0) - n_i \ln N$ for the calculated value ε_0 , and the straight line near which the points are located corresponds to the calculated value S_0 .

Discussion of the results

As follows from Table 1, the values S_0 and ε_0 increase with an increase in the control parameter f . Despite the fact that, in our opinion no rigorous theory that allows calculating the values of S_0 and ε_0 can be constructed, there can be some theoretical estimates that explain the tendency of these values to increase and give values close to the values of the numerical experiment.

The value S_0 , in the sense of its definition, should not depend on the properties of the fractal inherent in the chaotic attractor, but should be determined by some integral characteristics of the probability density for the chaotic attractor. To determine these properties, one can try to refer to the systems studied by statistical physics (see, for example, (Landau, Lifshitz 1980)). For such systems, entropy can be defined by the expression:

$$S = \ln \Delta \Gamma. \tag{10}$$

In this expression, $\Delta \Gamma$ is a statistical weight, the meaning of which is that it characterizes the size of the region of the phase space in which this system spends almost all the time. Since the definition of entropy should not depend on the units of measurement, the dimensions of the specified area of space should be calculated relative to some dimensional quantity taken as a unit of measurement. The quasi-classical limit gives as such a value of the Planck constant h , and for $\Delta \Gamma$ the value:

$$\Delta \Gamma = \frac{\prod_{i=1}^s \Delta q_i \Delta p_i}{h^s}, \tag{11}$$

where s is the number of degrees of freedom of the system, q_i and p_i are the generalized coordinates and impulses of the system.

Without pretending to be a strict justification, we generalize the above formulas for our case. We define the part of entropy that does not depend on the dimension of the chaotic attractor by the expression:

$$S_0 = \ln \Delta \Gamma. \tag{12}$$

Taking into account the large-scale time transformations carried out, the variables τ , θ and p are already measured in relative units. Taking expression (11) as a basis, we define the statistical weight by the expression:

$$\Delta \Gamma = \Delta \tau \Delta \theta \Delta p, \tag{13}$$

where $\Delta \tau$, $\Delta \theta$, Δp are the characteristic sizes of the regions of the corresponding variables in which the system is located most of the time. Obviously, $\Delta \tau = \Delta \theta = 1$ for any value of the control parameter f . As for the value Δp , then, as the calculation shows, it increases with an increase in the parameter f , since, in general, the movement becomes more intense. It is hardly possible to propose an analytical estimate of the dependence $\Delta p(f)$, however, using numerical results for the probability density of this system, it is possible to obtain numerical estimates which will be given below.

To estimate the value of ε_0 , we note that in the sense of this value, it must be associated with a region of the phase space in which the values of τ , θ and p change. But for any value of the control parameter f corresponding to chaotic motion, the values τ and θ always lie in the range $[0, 2\pi]$. Only the region of the variable p , as the numerical experiment shows, increases with the increasing f .

To get an approximate estimate of ε_0 , the unit orths $\{e_\theta, e_p, e_\tau\}$ should be reduced to one scale so that $e'_\theta = e'_p = e'_\tau = \varepsilon_0$. When choosing a scale, it is advisable, in accordance with formula (8), in the case of the simplest regular motion, to put $S_0 = 0$ and, consequently, $\varepsilon_0 = 1$. Since in this case the variable τ takes a value in the range $[0, 2\pi]$, the scale transformation has the form:

$$e'_\tau = \pi e_\tau \tag{14}$$

It is reasonable to assume that such a transformation persists in chaotic motion, and is also true for the variable θ , which takes values in the interval $[0, 2\pi]$ in chaotic motion:

$$e'_\theta = \pi e_\theta. \tag{15}$$

But, since the variables θ, p and τ are connected by a system of equations (2), the scale transformations (14) and (15) result in a scale transformation for the variable p :

$$e'_p = e_p.$$

From these arguments it follows that to estimate the value of ε_0 , one can take half of the range of changes in the value of p in chaotic motion. As mentioned above, for any value of the control parameter f , the area of change of p is limited by some interval $[-p_{\max}, p_{\max}]$. Thus, to estimate the value of ε_0 , we can put:

$$\varepsilon_0 = p_{\max}. \tag{16}$$

Numerical estimates of the values Δp and p_{\max} can be obtained using the calculated array $\rho(N, \tau, \theta, p_k)$. To do this, we average the probability density $\rho(N, \tau, \theta, p_k)$ over the variables τ and θ :

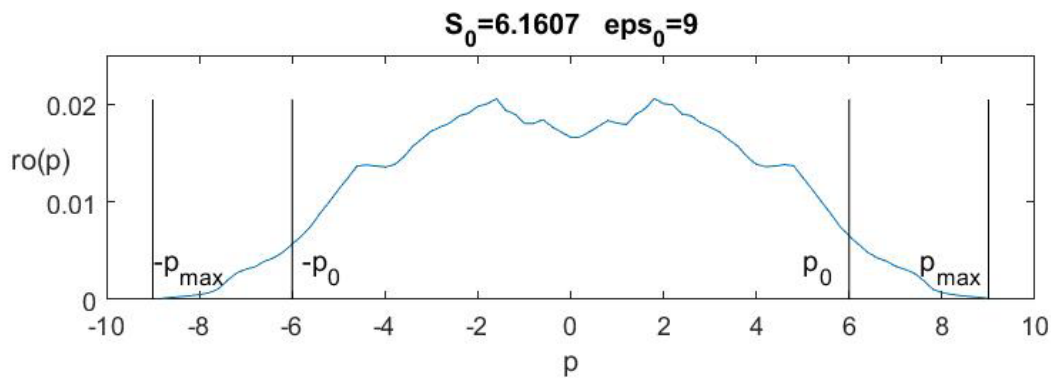


Fig. 4. Graph of the averaged probability density $\rho(N, p_k)$

From the definition of probability density, the area under the graph is equal to one. Let us define $\Delta p = 2p_0$, where p_0 is chosen so that the area under the graph between the values $-p_0$ and p_0 is approximately 0.9. Approximately, we can assume that the system spends almost all the time in the region $[-p_0, p_0]$.

The comparison of the results obtained by the numerical experiment (Table 1) and estimates according to formulas (13) and (16) are clearly shown in Fig. 5. Estimates are obtained for the values of the control parameter f lying in the middle of the corresponding range.

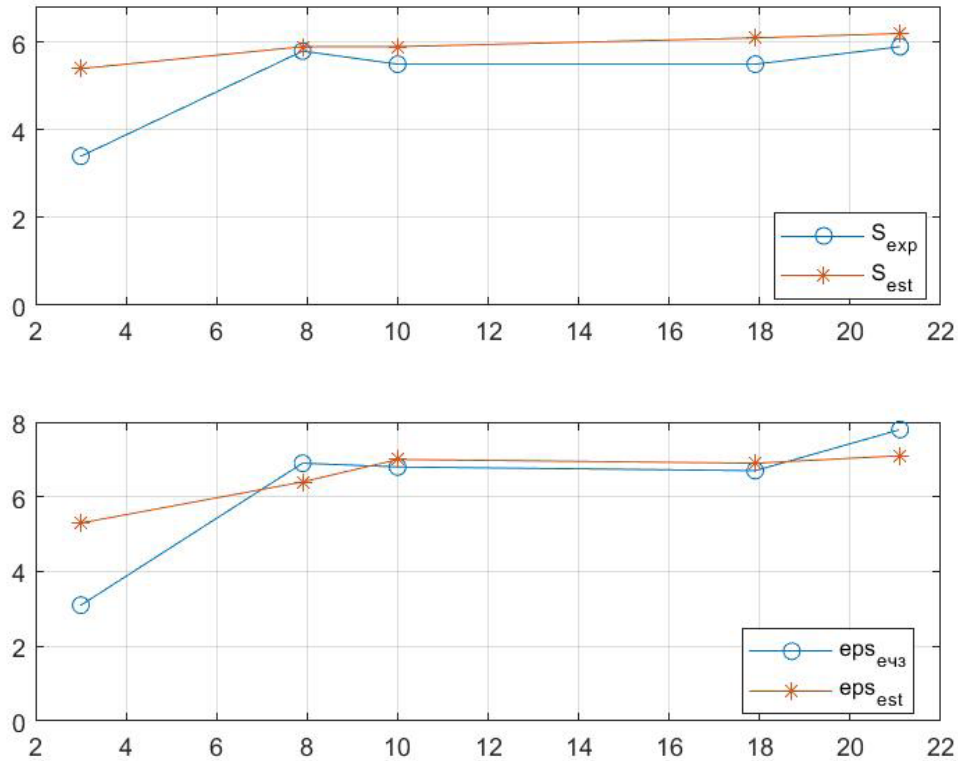


Fig. 5. Comparison of the results of the numerical experiment and the estimates obtained by formulas (13) and (16) for the parameters S_0 and ϵ_0

As can be seen from the figure, with sufficiently large values of the control parameter, rough estimates turn out to be close to the values obtained by the numerical experiment.

Conflict of interest

The author declares that there is no conflict of interest, either existing or potential.

References

Gonchenko, A. S., Gonchenko, S. V., Kazakov, A. O., Kozlov, A. D. (2017) Matematicheskaya teoriya dinamicheskogo khaosa i ee prilozheniya: Obzor. Ch. 1. Pseudogiperbolicheskie attraktory [Mathematical theory of dynamical chaos and its applications: Review. Pt. 1. Pseudohyperbolic attractors]. *Izvestiya Vysshikh uchebnykh zavedenij. Prikladnaya nelinejnaya dinamika — Izvestiya VUZ. Applied Nonlinear Dynamics*, 25 (2), 4–36. (In Russian)

Grinchenko, V. T., Matsipura, V. T., Snarskij, A. A. (2007) *Vvedenie v nelinejnyu dinamiku. Khaos i fractaly [Introduction to nonlinear dynamics. Chaos and fractals]*. 2nd ed. Moscow: URSS Publ., 284 p. (In Russian)

Kuznetsov, S. P. (2006) *Dinamicheskij khaos: kurs leksij [Dynamic chaos: A course of lectures]*. 2nd ed. Moscow: Fizmatlit Publ., 356 p. (In Russian)

Landau, L. D., Lifshitz, E. M. (1980) *Course of theoretical physics series. Vol. 5. Statistical physics. Pt. 1*. 3rd ed. Oxford: Butterworth–Heinemann Publ., 564 p. (In English)

Liapzev, A. V. (2019) The calculation of the probability density in phase space of a chaotic system on the example of rotator in the harmonic field. *Computer Aassisted Mathematics*, 1, 55–65. (In English)

Malinetsky, G. G., Potapov, A. B. (2000) *Sovremennyye problemy nelinejnoj dinamiki [Modern problems of nonlinear dynamics]*. Moscow: URSS Publ., 336 p. (In Russian)

Sagdeev, R. Z., Usikov, D. A., Zaslavsky, G. M. (1988) *Nonlinear physics: From the pendulum to turbulence and chaos*. New York: Harwood Academic Publ., 675 p. (In English)

- Schuster, G. H., Just, W. (2005) *Deterministic chaos. An introduction*. 4th ed. Weinheim: Wiley-VCH Publ., 283 p. (In English)
- Stockmann, H. J. (1999) *Quantum chaos: An introduction*. Cambridge: Cambridge University Press, 368 p. <https://doi.org/10.1017/CBO9780511524622> (In English)



Check for updates

Theoretical Physics. Quantum Mechanics

UDC 517.938

EDN KZISPS

<https://www.doi.org/10.33910/2687-153X-2022-3-4-186-201>

Atmospheric implementation of superdense coding quantum algorithm

B. A. Timchenko¹, M. P. Faleeva¹, P. A. Gilev¹, I. V. Blinova¹, I. Yu. Popov^{✉1}

¹ ITMO University, 49 Kronverksky Ave., Saint Petersburg 197101, Russia

Authors

Bogdan A. Timchenko, e-mail: bogdantimchenko@yandex.ru

Maria P. Faleeva, e-mail: faleeva.masha@gmail.com

Pavel A. Gilev, e-mail: grandarchtemplar@gmail.com

Irina V. Blinova, e-mail: irin-a@yandex.ru

Igor Yu. Popov, ORCID: [0000-0002-5251-5327](https://orcid.org/0000-0002-5251-5327), e-mail: popov1955@gmail.com

For citation: Timchenko, B. A., Faleeva, M. P., Gilev, P. A., Blinova, I. V., Popov, I. Yu. (2022) Atmospheric implementation of superdense coding quantum algorithm. *Physics of Complex Systems*, 3 (4), 186–201. <https://www.doi.org/10.33910/2687-153X-2022-3-4-186-201> EDN KZISPS

Received 12 September 2022; reviewed 2 October 2022; accepted 2 October 2022.

Funding: The work was partially supported by grant No. 19-31-90154 of the Russian Foundation for Basic Research.

Copyright: © B. A. Timchenko, M. P. Faleeva, P. A. Gilev, I. V. Blinova, I. Yu. Popov (2022). Published by Herzen State Pedagogical University of Russia. Open access under [CC BY-NC License 4.0](https://creativecommons.org/licenses/by-nc/4.0/).

Abstract. We consider the properties of a quantum communication channel in open space using the superdense coding algorithm as an example. We studied the theoretical model of the installation that implements this algorithm, and identified the main factors affecting the quality of the model. Among them is the atmospheric transmittance, the efficiency of detectors, and the average value of the number of noise counts caused by background radiation and dark counts. We made a complete calculation of the installation model and obtained explicit results. These results were analyzed using realistic parameters of detectors and the atmosphere. It was found that the atmospheric turbulence instability, detectors efficiency and the average value of noise counts have the greatest influence on the results.

Keywords: quantum channel, dense coding, entanglement, atmosphere, model

Introduction

At the moment, processors with 10 nm manufacturing technology are already widespread, which corresponds to literally several tens of silicon atoms. These sizes are so small that fundamental difficulties are already appearing that introduce quantum effects. A possible solution to this problem is the transition to another computing paradigm. Recently, the quantum theory of information, which provides a similar paradigm, has been central to many studies. However, there still is a number of unresolved issues related, in particular, to network interaction between processors of quantum information. Networking is one of the most important components of computing systems that allows for scalable growth. This role is preserved in quantum networks. Of course, the functional elements that provide communication between nodes change. From examples of use, we can distinguish distributed quantum computing and the quantum distribution of keys used in cryptography. The possibility of implementing the latter using quantum communication channels formed by polarized photons in open space was recently shown experimentally (Elser et al. 2009; Fedrizzi et al. 2009; Ursin et al. 2007). This raises the question of preserving the nonclassical properties of light as it passes through fluctuating media. Generated by Kolmogorov's theory of turbulence, the theory of classical light transmission through the atmosphere

has been studied for a long time (Ishimaru 1978; Tatarskii 1971). Compared to it, the theory of transmission of quantum light in random media is less developed. A theoretical model of light passing through a turbulent atmosphere and processed by homodyne detection has recently been proposed (Semenov et al. 2008; 2009). It describes random media and fluctuating loss channels that introduce additional noise into the quantum states of light in comparison with standard channels. Such noise was discovered in (Dong et al. 2008; Heersink et al. 2006). In this paper, we study the transfer of entanglement by photons through a turbulent atmosphere using fluctuating loss channels. The relevance of this issue lies in the fact that quantum networks are attracting an increasing interest, and theoretical noise estimates can give a more realistic forecast of experimental data (Adam et al. 2022, Fedrizzi et al. 2009; Gilev, Popov 2019; Herbst et al. 2015). The object of the study was a scheme that implements a superdense coding algorithm. The choice is due to the fact that this scheme uses quantum communication channels to achieve the results that have no analogue using classical channels. In addition, the results of the scheme work can be presented in a simpler form. These results are the subject of research, namely, the probability of postselective detection of various pairs of bits depending on the transmitted pair. The aim of the work is to investigate the dependence of the probabilities defined above on the parameters of a turbulent atmosphere.

The work is structured as follows. Section 2 provides an overview of the superdense coding algorithm, its physical implementation, and analysis of factors that impact the final result. In section 3, we calculate the matrix of the density of states of the system at all stages, detect the resulting state on a linear Bell state meter and obtain the probabilities indicated in the purpose of this study.

Theoretical background

Device description

Superdense coding is an algorithm that allows you to transfer two bits of classical information by sending only one qubit, under the assumption that Alice and Bob prepared and shared an entangled state. The transmission of two bits is possible due to the quantum intricacies of the qubits. It was developed by (Bennett, Wiesner 1992) and experimentally implemented in 1996 (Mattle et al. 1996).

The algorithm can be described by the circuit shown in Figure 1. Logically, it consists of three parts. The sender (Alice) wants to send two classical bits of information (00, 01, 10, or 11) to the recipient (Bob) using qubits (instead of classical bits). To do this, she prepares a pair of entangled qubits in the state $|\psi^+\rangle = \frac{1}{\sqrt{2}}(|10\rangle + |01\rangle)$, which is a Bell state using the Hadamard element and CNOT.

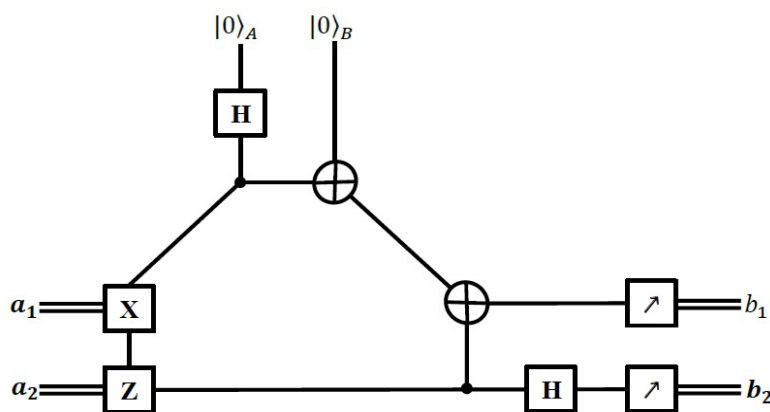


Fig. 1. Quantum circuit for the implementation of superdense coding algorithm

On the left side of the circuit, the first qubit is encoded by Alice by applying the elements X and/or Z . Depending on the transmitted pair of bits, the system of two qubits goes into one of the states:

$$\begin{aligned}
 00: |\psi^+\rangle &\rightarrow |\psi^+\rangle = \frac{1}{\sqrt{2}}(|01\rangle + |10\rangle), \\
 01: |\psi^+\rangle &\rightarrow |\phi^+\rangle = \frac{1}{\sqrt{2}}(|00\rangle + |11\rangle), \\
 10: |\psi^+\rangle &\rightarrow |\psi^-\rangle = \frac{1}{\sqrt{2}}(|01\rangle - |10\rangle), \\
 11: |\psi^+\rangle &\rightarrow |\phi^-\rangle = \frac{1}{\sqrt{2}}(|00\rangle - |11\rangle).
 \end{aligned}$$

These four states are called Bell states, and they form an orthonormal basis, which means that they can be uniquely distinguished by a suitable measurement. After sending the qubits to Bob (by different paths), this measurement is performed on the right side of the circuit using the Hadamard element, CNOT and measuring instruments. All the mentioned quantum elements are described in (Nielsen, Chuang 2010).

The circuit described above works correctly under the condition that there is no noise affecting the state of the system. However, in experimental implementation (Dong et al. 2008; Heersink et al. 2006), noise is inevitable, and errors appear in the operation of the algorithm. This must be considered when using it.

Model background

General remarks

When assessing the effect of noise on the quality of the algorithm, it is necessary to design a model of the installation that executes this algorithm, and note the places where the noise appears and its nature. When modeling quantum circuits, first, it is necessary to solve the question of the carrier of quantum information. In this work, the polarization of a photon is used for qubit coding (Mandel, Wolf 1995), since photons propagate relatively freely in the atmosphere. Note that for atmospheric quantum channels, modes of Gaussian beam can be used for qubit coding (Faleeva, Popov 2020a; 2020b; 2022). As it is known, when coding by polarization states (Semenov, Vogel 2010) a qubit is noted by $\alpha|H\rangle + \beta|V\rangle$ where $|H\rangle$ state means that a photon is in the horizontal mode, $|V\rangle$ state means that a photon is in the vertical mode. This notation is identical to the notation

$$|\psi^+\rangle = \frac{1}{\sqrt{2}}(|1\rangle_{H_A} |0\rangle_{V_A} |0\rangle_{H_B} |1\rangle_{V_B} + |0\rangle_{H_A} |1\rangle_{V_A} |1\rangle_{H_B} |0\rangle_{V_B}),$$

which will be written in simpler form:

$$|\psi^+\rangle = \frac{1}{\sqrt{2}}(|1001\rangle + |0110\rangle). \tag{1}$$

Analogously, the other Bell states for the polarization of photons are as follows:

$$|\phi^+\rangle = \frac{1}{\sqrt{2}}(|1010\rangle + |0101\rangle),$$

$$|\psi^-\rangle = \frac{1}{\sqrt{2}}(|1001\rangle - |0110\rangle),$$

$$|\phi^-\rangle = \frac{1}{\sqrt{2}}(|1010\rangle - |0101\rangle),$$

where the states are presented in the Fock basis and correspond to modes H_A, V_A, H_B and V_B . We take (1) as the initial state.

Alice's part

To model coding at the Alice's part, one should present physical implementation of elements X and Z . Element X performs the operation $\{|0\rangle \rightarrow |1\rangle, |1\rangle \rightarrow |0\rangle\}$. In terms of the annihilation operators it looks as follows $\{\hat{a}_H^{out} = \hat{a}_V^{in}, \hat{a}_V^{out} = \hat{a}_H^{in}\}$. A half-wavelength plate (HWP) can be a model of element X . The Jones matrix for it has the form (Peters et al. 2003):

$$O_{HWP}(\theta) = \begin{pmatrix} -\cos 2\theta & -\sin 2\theta \\ -\sin 2\theta & \cos 2\theta \end{pmatrix},$$

where θ is the angle between the optical axis and the horizontal mode. One has for $\theta = -\frac{\pi}{4}$:

$$O_{HWP}\left(-\frac{\pi}{4}\right) = \begin{pmatrix} 0 & 1 \\ 1 & 0 \end{pmatrix},$$

which corresponds to proper transformation: $\{\hat{a}_H^{out} = \hat{a}_H^{in}, \hat{a}_V^{out} = -\hat{a}_V^{in}\}$.

Element Z performs the transformation $\{|0\rangle \rightarrow |0\rangle, |1\rangle \rightarrow -|1\rangle\} \Leftrightarrow \{\hat{a}_H^{out} = \hat{a}_H^{in}, \hat{a}_V^{out} = -\hat{a}_V^{in}\}$. One can take two 1/4-wavelength plates (QWP) for Z . The corresponding Jones matrix is as follows (Peters et al. 2003):

$$O_{QWP}(\theta) = \begin{pmatrix} 1 - (1+i)\cos^2\theta & -(1+i)\sin\theta\cos\theta \\ -(1+i)\sin\theta\cos\theta & 1 - (1+i)\sin^2\theta \end{pmatrix}.$$

For $\theta = -\frac{\pi}{2}$, one gets:

$$O_{QWP}\left(-\frac{\pi}{2}\right) = \begin{pmatrix} 1 & 0 \\ 0 & -i \end{pmatrix}.$$

For two plates, one has the square of QWP Jones matrix corresponding to proper transformation.

As a result, in a relation with the transmitted bits, the transformations of the annihilation operators at the Alice's side are as follows:

$$\begin{aligned} 00: & \{\hat{a}_H^{out} = \hat{a}_H^{in}, \hat{a}_V^{out} = \hat{a}_V^{in}\}, \\ 01: & \{\hat{a}_H^{out} = \hat{a}_V^{in}, \hat{a}_V^{out} = \hat{a}_H^{in}\}, \\ 10: & \{\hat{a}_H^{out} = \hat{a}_H^{in}, \hat{a}_V^{out} = -\hat{a}_V^{in}\}, \\ 11: & \{\hat{a}_H^{out} = -\hat{a}_V^{in}, \hat{a}_V^{out} = \hat{a}_H^{in}\}. \end{aligned} \tag{2}$$

Bob's part

An implementation of the Bell side is the Bell meter shown in Figure 2.

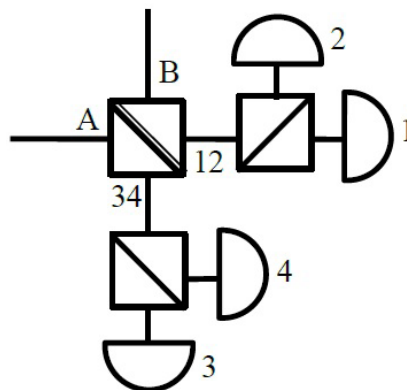


Fig. 2. Copenhagen circuit for Bell measurement

It is important to consider that this model is not perfect, which will be shown below. An alternative is the Kerr medium for photon interaction (Nielsen, Chuang 2010) or the use of photon hyper-entanglement, as was done in 2001 (Williams et al. 2018), to unambiguously distinguish Bell states. The main elements of this measuring device are as follows: a symmetric beam splitter, two polarizing beam splitters and four detectors operating in the photon counting mode. The role of the symmetric beam splitter in this measurement is the interference of the photons of the incoming modes A and B . In fact, this means that the sum and the difference of the two fields are formed at the outputs. Relations between the operators at the input and output are as follows (Schleich 2001):

$$\hat{a}_1 = \frac{1}{\sqrt{2}}(\hat{a}_{HA} + \hat{a}_{HB}), \quad \hat{a}_2 = \frac{1}{\sqrt{2}}(\hat{a}_{VA} + \hat{a}_{VB}),$$

$$\hat{a}_3 = \frac{1}{\sqrt{2}}(-\hat{a}_{HA} + \hat{a}_{HB}), \quad \hat{a}_4 = \frac{1}{\sqrt{2}}(-\hat{a}_{VA} + \hat{a}_{VB}).$$

Polarization beam splitters allow one to separate photons with horizontal and vertical polarization and position of photon each group in a separate detector. In accordance with the photodetection theory (Soderholm et al. 2012), the probability of detecting n_1, n_2, n_3, n_4 photons on detectors 1, 2, 3, 4, respectively, is determined by the formula:

$$P_{n_1, n_2, n_3, n_4} = Tr\left(\hat{\Pi}_1^{(n_1)}\hat{\Pi}_2^{(n_2)}\hat{\Pi}_3^{(n_3)}\hat{\Pi}_4^{(n_4)}\hat{\rho}\right), \tag{3}$$

where $\hat{\rho}$ is the density operator of the light before the detection,

$$\hat{\Pi}_x^{(n)} =: \left| \frac{(\eta_x \hat{n}_x + N_x)^n}{n!} \exp(-\eta_x \hat{n}_x - N_x) \right|: \tag{4}$$

is the measurement operator for detector x , where η_x is the detector efficiency, \hat{n}_x is the photon number operator at the input of the detector x , means normal ordering, and N_x is the number of wrong counts related to the dark counts and the background radiation.

Model of the atmospheric influence

One of the main objectives of this work is to describe the passage of light through a turbulent atmosphere (sections A and B in the diagram in Figure 3). Similarly to the approach used by (Bohmann et al. 2016; Semenov, Vogel 2009; Vasylyev et al. 2016), who studied a similar problem, we consider the atmosphere as a system with damped oscillations.

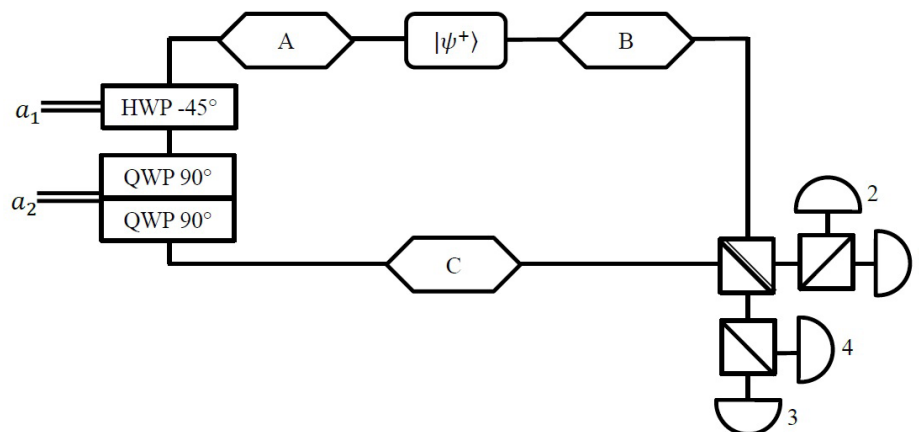


Fig. 3. Theoretical model of the device

The equations connecting the annihilation operators before and after passing through the atmosphere are as follows

$$\begin{aligned}\hat{a}_H^{out} &= T_H \hat{a}_H^{in} + T_{HV} \hat{a}_V^{in} + R_H \hat{c}_H^{in}, \\ \hat{a}_V^{out} &= T_V \hat{a}_V^{in} + T_{VH} \hat{a}_H^{in} + R_V \hat{c}_V^{in},\end{aligned}\tag{5}$$

where T_H and T_V are the transmission coefficients for the horizontal and the vertical modes, T_{HV} and T_{VH} are the depolarization coefficients, R_H and R_V are coefficients related to losses due to the reflection and the absorption described by operators \hat{c}_H^{in} and \hat{c}_V^{in} , respectively. It was shown by (Semenov, Vogel 2009) that the depolarizing effect of the atmosphere is very small. Hence, it is possible to assume that, $T_{HV} \approx 0$, $T_H \approx T_V \equiv T$. This allows one to simplify (5):

$$\hat{a}_H^{out} = T \hat{a}_H^{in} + R_H \hat{c}_H^{in}, \quad \hat{a}_V^{out} = T \hat{a}_V^{in} + R_V \hat{c}_V^{in}.\tag{6}$$

Normalization leads to the relation

$$|T|^2 + |R_{H(V)}|^2 = 1.\tag{7}$$

The atmosphere is random media so it can be considered as a quantum channel characterized by fluctuating transmission properties. Therefore, the turbulence can be modeled by introducing probability distribution function of transmission coefficient, which should correspond with turbulence condition. It was shown by (Gumberidze et al. 2016) that, depending on turbulence case, different functions would approximate the transmission coefficient distribution. We consider the case of strong turbulence only.

Model

Bell states transmission through atmosphere

We deal with the following initial state

$$|\psi^+\rangle = \frac{1}{\sqrt{2}} (|1001\rangle + |0110\rangle).\tag{8}$$

The density operator of the photons state $|\psi^+\rangle$ is

$$\hat{\rho}_{in} = |\psi^+\rangle \langle \psi^+|.$$

Let us calculate density operators after Alice's coding described by (2):

$$\hat{\rho}_{Alice}^{00} = \hat{\rho}_{in},\tag{9}$$

$$\hat{\rho}_{Alice}^{01} = \hat{\rho}_{\phi^+} = |\phi^+\rangle \langle \phi^+|,\tag{10}$$

$$\hat{\rho}_{Alice}^{10} = \hat{\rho}_{\psi^-} = |\psi^-\rangle \langle \psi^-|,\tag{11}$$

$$\hat{\rho}_{Alice}^{11} = \hat{\rho}_{\phi^-} = |\phi^-\rangle \langle \phi^-|.\tag{12}$$

To obtain the density operator for the state after the light transmission of paths A and B, we will use the approach of the input-output relations in terms of the Glauber–Sudarshan P-function. This approach was applied for deriving the output density matrices of the transmitted light in turbulent atmosphere by (Semenov, Vogel 2010).

Well-known Glauber–Sudarshan P-function is defined by determining the form of the density operator $\hat{\rho}$ in the basis of coherent states $\{|\alpha\rangle\}$:

$$\hat{\rho} = \int P(\alpha) |\alpha\rangle \langle \alpha| d^2\alpha.\tag{13}$$

The next formula for the P-function is more important for the practical calculations:

$$P(\alpha) = \frac{1}{\pi^2} \int_{-\infty}^{+\infty} \chi(\beta) \exp(\alpha\beta^* - \alpha^*\beta) d^2\beta. \quad (14)$$

Here, $\chi(\beta) = \text{Tr}[\hat{\rho} \exp(\hat{a}^+\beta) \exp(-\hat{a}\beta^*)]$ is the characteristic function; \hat{a} , \hat{a}^+ are the annihilation and creation operators.

Relations for the above functions between the input state and the transmitted state are given by the following expressions:

$$\hat{\rho}_{out} = \int P_{out}(\alpha) |\alpha\rangle\langle\alpha| d^2\alpha, \quad (15)$$

$$P_{out}(\alpha) = \frac{1}{T^2} P_{in}\left(\frac{\alpha}{T}\right), \quad (16)$$

$$\chi_{out}(\beta) = \chi_{in}(T\beta). \quad (17)$$

Formulas (13)–(17) allow one to derive the expression for the output density operator of the states (9)–(12) when the qubit coded by Alice is sent by path A and another qubit is sent by path B:

$$\begin{aligned} \hat{\rho}_{AB} &= (1-|T_A|^2)(1-|T_B|^2) \hat{\rho}_{vac} + \frac{1}{2}(1-|T_B|^2)|T_A|^2 \hat{\rho}_{H_A} + \frac{1}{2}(1-|T_B|^2)|T_A|^2 \hat{\rho}_{V_A} + \\ &+ \frac{1}{2}(1-|T_A|^2)|T_B|^2 \hat{\rho}_{H_B} + \frac{1}{2}(1-|T_A|^2)|T_B|^2 \hat{\rho}_{V_B} + |T_A|^2|T_B|^2 \hat{\rho}_{in}, \end{aligned}$$

$$\begin{aligned} \hat{\rho}_{AB} &= (1-|T_A|^2)(1-|T_B|^2) \hat{\rho}_{vac} + \frac{1}{2}(1-|T_B|^2)|T_A|^2 \hat{\rho}_{H_A} + \frac{1}{2}(1-|T_B|^2)|T_A|^2 \hat{\rho}_{V_A} + \\ &+ \frac{1}{2}(1-|T_A|^2)|T_B|^2 \hat{\rho}_{H_B} + \frac{1}{2}(1-|T_A|^2)|T_B|^2 \hat{\rho}_{V_B} + |T_A|^2|T_B|^2 \hat{\rho}_{\phi^+}, \end{aligned}$$

$$\begin{aligned} \hat{\rho}_{AB} &= (1-|T_A|^2)(1-|T_B|^2) \hat{\rho}_{vac} + \frac{1}{2}(1-|T_B|^2)|T_A|^2 \hat{\rho}_{H_A} + \frac{1}{2}(1-|T_B|^2)|T_A|^2 \hat{\rho}_{V_A} + \\ &+ \frac{1}{2}(1-|T_A|^2)|T_B|^2 \hat{\rho}_{H_B} + \frac{1}{2}(1-|T_A|^2)|T_B|^2 \hat{\rho}_{V_B} + |T_A|^2|T_B|^2 \hat{\rho}_{\psi^-}, \end{aligned}$$

$$\begin{aligned} \hat{\rho}_{AB} &= (1-|T_A|^2)(1-|T_B|^2) \hat{\rho}_{vac} + \frac{1}{2}(1-|T_B|^2)|T_A|^2 \hat{\rho}_{H_A} + \frac{1}{2}(1-|T_B|^2)|T_A|^2 \hat{\rho}_{V_A} + \\ &+ \frac{1}{2}(1-|T_A|^2)|T_B|^2 \hat{\rho}_{H_B} + \frac{1}{2}(1-|T_A|^2)|T_B|^2 \hat{\rho}_{V_B} + |T_A|^2|T_B|^2 \hat{\rho}_{\phi^-}, \end{aligned}$$

where $T_{A,B}$ are random transmission coefficients in the direction of the A(B) paths respectively; $\hat{\rho}_{vac}$ is the density operator of vacuum state, $\hat{\rho}_{H_{A,B}}$ and $\hat{\rho}_{V_{A,B}}$ are the density operators of one photon states, $\hat{\rho}_{in}$ is the density operator of the initial Bell state.

According to these results, it can be seen that either the zero-photon, or one of the eight different single-photon states, or a specific two-photon state, which depends only on the coding on the Alice's side, comes to the input of the beam splitter with the corresponding probabilities. For further calculation, it is necessary to express the annihilation operators of incoming modes through the outgoing operators:

$$\hat{a}_{H_A} = \frac{1}{\sqrt{2}}(\hat{a}_1 - \hat{a}_3), \quad (18)$$

$$\hat{a}_{V_A} = \frac{1}{\sqrt{2}}(\hat{a}_2 - \hat{a}_4), \quad (19)$$

$$\hat{a}_{H_B} = \frac{1}{\sqrt{2}}(\hat{a}_1 + \hat{a}_3), \quad (20)$$

$$\hat{a}_{V_B} = \frac{1}{\sqrt{2}}(\hat{a}_2 + \hat{a}_4). \quad (21)$$

The transformation of the single-photon states and the Bell states during the passage of the beam splitter is as follows:

$$|\gamma\rangle_{1D} = |1000\rangle = \hat{a}_{H_A}^\dagger |0000\rangle = (\hat{a}_1^\dagger - \hat{a}_3^\dagger) |0000\rangle = (|1\rangle_1 |0\rangle_2 |0\rangle_3 |0\rangle_4 - |0\rangle_1 |0\rangle_2 |1\rangle_3 |0\rangle_4), \quad (22)$$

$$|\gamma\rangle_{2D} = |0100\rangle = \hat{a}_{V_A}^\dagger |0000\rangle = (\hat{a}_2^\dagger - \hat{a}_4^\dagger) |0000\rangle = (|0\rangle_1 |1\rangle_2 |0\rangle_3 |0\rangle_4 - |0\rangle_1 |0\rangle_2 |0\rangle_3 |1\rangle_4), \quad (23)$$

$$|\gamma\rangle_{3D} = |0010\rangle = \hat{a}_{H_B}^\dagger |0000\rangle = (\hat{a}_1^\dagger + \hat{a}_3^\dagger) |0000\rangle = (|1\rangle_1 |0\rangle_2 |0\rangle_3 |0\rangle_4 + |0\rangle_1 |0\rangle_2 |1\rangle_3 |0\rangle_4), \quad (24)$$

$$|\gamma\rangle_{4D} = |0001\rangle = \hat{a}_{V_B}^\dagger |0000\rangle = (\hat{a}_2^\dagger + \hat{a}_4^\dagger) |0000\rangle = (|0\rangle_1 |1\rangle_2 |0\rangle_3 |0\rangle_4 + |0\rangle_1 |0\rangle_2 |0\rangle_3 |1\rangle_4), \quad (25)$$

$$|\psi^+\rangle_D = \frac{1}{\sqrt{2}}(|1001\rangle + |0110\rangle) = \frac{1}{\sqrt{2}}(\hat{a}_{H_A}^\dagger \hat{a}_{V_B}^\dagger + \hat{a}_{V_A}^\dagger \hat{a}_{H_B}^\dagger) |0000\rangle = \frac{1}{2\sqrt{2}}((\hat{a}_1^\dagger - \hat{a}_3^\dagger)(\hat{a}_2^\dagger + \hat{a}_4^\dagger) + (\hat{a}_2^\dagger - \hat{a}_4^\dagger)(\hat{a}_1^\dagger + \hat{a}_3^\dagger)) |0000\rangle = \quad (26)$$

$$\frac{1}{2\sqrt{2}}(2\hat{a}_1^\dagger \hat{a}_2^\dagger - 2\hat{a}_3^\dagger \hat{a}_4^\dagger) |0000\rangle = \frac{1}{\sqrt{2}}(|1\rangle_1 |1\rangle_2 |0\rangle_3 |0\rangle_4 - |0\rangle_1 |0\rangle_2 |1\rangle_3 |1\rangle_4),$$

$$|\phi^+\rangle_D = \frac{1}{\sqrt{2}}(|0101\rangle + |1010\rangle) = \frac{1}{\sqrt{2}}(\hat{a}_{H_A}^\dagger \hat{a}_{H_B}^\dagger + \hat{a}_{V_A}^\dagger \hat{a}_{V_B}^\dagger) |0000\rangle =$$

$$\frac{1}{2\sqrt{2}}((\hat{a}_1^\dagger - \hat{a}_3^\dagger)(\hat{a}_1^\dagger + \hat{a}_3^\dagger) + (\hat{a}_2^\dagger - \hat{a}_4^\dagger)(\hat{a}_2^\dagger + \hat{a}_4^\dagger)) |0000\rangle = \quad (27)$$

$$\frac{1}{2\sqrt{2}}((\hat{a}_1^\dagger)^2 - (\hat{a}_3^\dagger)^2 + (\hat{a}_2^\dagger)^2 - (\hat{a}_4^\dagger)^2) |0000\rangle =$$

$$\frac{1}{2}(|2\rangle_1 |0\rangle_2 |0\rangle_3 |0\rangle_4 + |0\rangle_1 |2\rangle_2 |0\rangle_3 |0\rangle_4 - |0\rangle_1 |0\rangle_2 |2\rangle_3 |0\rangle_4 - |0\rangle_1 |0\rangle_2 |0\rangle_3 |2\rangle_4)$$

Analogously, for states $|\psi^-\rangle$ and $|\phi^-\rangle$:

$$|\psi^-\rangle_D = \frac{1}{\sqrt{2}}(|1\rangle_1 |0\rangle_2 |0\rangle_3 |1\rangle_4 - |0\rangle_1 |1\rangle_2 |1\rangle_3 |0\rangle_4). \quad (28)$$

$$|\phi^-\rangle_D = \frac{1}{2}(|2\rangle_1 |0\rangle_2 |0\rangle_3 |0\rangle_4 - |0\rangle_1 |2\rangle_2 |0\rangle_3 |0\rangle_4 - |0\rangle_1 |0\rangle_2 |2\rangle_3 |0\rangle_4 + |0\rangle_1 |0\rangle_2 |0\rangle_3 |2\rangle_4) \quad (29)$$

Thus, the density operator for photons before the detection has the form:

$$\hat{P}_{out} = P_{vac} \hat{P}_{(vac)} + P_A \hat{P}_{(A)} + P_B \hat{P}_{(B)} + P_{Bell} \hat{P}_{(Bell)}, \quad (30)$$

where the transmission probabilities of different numbers of photons are as follows

$$p_{vac} = (1 - |T_A|^2)(1 - |T_B|^2), \tag{31}$$

$$p_A = p_{H_A} = p_{V_A} = \frac{1}{2}|T_A|^2(1 - |T_B|^2), \tag{32}$$

$$p_B = p_{H_B} = p_{V_B} = \frac{1}{2}|T_B|^2(1 - |T_A|^2), \tag{33}$$

$$p_2 = |T_A|^2|T_B|^2. \tag{34}$$

Here $\hat{\rho}_{(vac)}$ is a vacuum state,

$$\hat{\rho}_{(A)} = |\gamma\rangle_{1D}\langle\gamma| + |\gamma\rangle_{2D}\langle\gamma|,$$

$$\hat{\rho}_{(B)} = |\gamma\rangle_{3D}\langle\gamma| + |\gamma\rangle_{4D}\langle\gamma|$$

are single-photon density operators observed by one detector, $\hat{\rho}_{(Bell)}$ is a two-photon state of different forms depending on the sent qubits: $\hat{\rho}_{00} = |\psi^+\rangle_D\langle\psi^+|$, or $\hat{\rho}_{01} = |\varphi^+\rangle_D\langle\varphi^+|$, or $\hat{\rho}_{10} = |\psi^-\rangle_D\langle\psi^-|$, or $\hat{\rho}_{11} = |\varphi^-\rangle_D\langle\varphi^-|$.

Bell states detection

As in (30) one term only depends on sent qubits ($\hat{\rho}_{Bell}$), one should take the following expressions (based on (26)-(29)) as probabilities of distinguishing qubit pairs:

$$P_{00} = Tr(\hat{\Pi}_1^{(1)}\hat{\Pi}_2^{(1)}\hat{\Pi}_3^{(0)}\hat{\Pi}_4^{(0)}\hat{\rho}) + Tr(\hat{\Pi}_1^{(0)}\hat{\Pi}_2^{(0)}\hat{\Pi}_3^{(1)}\hat{\Pi}_4^{(1)}\hat{\rho}), \tag{35}$$

$$P_{10} = Tr(\hat{\Pi}_1^{(1)}\hat{\Pi}_2^{(0)}\hat{\Pi}_3^{(0)}\hat{\Pi}_4^{(1)}\hat{\rho}) + Tr(\hat{\Pi}_1^{(0)}\hat{\Pi}_2^{(1)}\hat{\Pi}_3^{(1)}\hat{\Pi}_4^{(0)}\hat{\rho}), \tag{36}$$

$$P_{01} = P_{11} = \frac{1}{2} (Tr(\hat{\Pi}_1^{(2)}\hat{\Pi}_2^{(0)}\hat{\Pi}_3^{(0)}\hat{\Pi}_4^{(0)}\hat{\rho}) + Tr(\hat{\Pi}_1^{(0)}\hat{\Pi}_2^{(2)}\hat{\Pi}_3^{(0)}\hat{\Pi}_4^{(0)}\hat{\rho})) + Tr(\hat{\Pi}_1^{(0)}\hat{\Pi}_2^{(0)}\hat{\Pi}_3^{(2)}\hat{\Pi}_4^{(0)}\hat{\rho}) + Tr(\hat{\Pi}_1^{(0)}\hat{\Pi}_2^{(0)}\hat{\Pi}_3^{(0)}\hat{\Pi}_4^{(2)}\hat{\rho}). \tag{37}$$

The general form of the measurement operator is given in (4). Let us calculate the images of different states under the action of this operator.

$$\begin{aligned} \hat{\Pi}_x^{(0)}|0\rangle_x\langle 0| &= e^{(-\eta_x\hat{n}_x - N_x)}|0\rangle_x\langle 0| = \\ e^{-N_x} \left(\sum_{k=0}^{\infty} \frac{(-1)^k}{k!} \eta_x^k \hat{n}_x^k \right) |0\rangle_x\langle 0| &= \\ = e^{-N_x} |0\rangle_x\langle 0|, \end{aligned} \tag{38}$$

$$\begin{aligned} \hat{\Pi}_x^{(0)}|1\rangle_x\langle 1| &= e^{-N_x} \left(1 - \eta_x\hat{n}_x + \sum_{k=2}^{\infty} \frac{(-1)^k}{k!} \eta_x^k \hat{n}_x^k \right) |1\rangle_x\langle 1| = \\ (1 - \eta_x) e^{-N_x} |1\rangle_x\langle 1|, \end{aligned} \tag{39}$$

$$\begin{aligned} \hat{\Pi}_x^{(0)}|2\rangle_x\langle 2| &= e^{-N_x} \left(1 - \eta_x\hat{n}_x + \frac{1}{2}\eta_x^2\hat{n}_x^2 + \sum_{k=3}^{\infty} \frac{(-1)^k}{k!} \eta_x^k \hat{n}_x^k \right) |2\rangle_x\langle 2| = \\ (1 - 2\eta_x + \eta_x^2) e^{-N_x} |2\rangle_x\langle 2| = (1 - \eta_x)^2 e^{-N_x} |2\rangle_x\langle 2|, \end{aligned} \tag{40}$$

$$\begin{aligned} \hat{\Pi}_x^{(1)}|0\rangle_x\langle 0| &= \left((\eta_x \hat{n}_x + N_x) e^{(-\eta_x \hat{n}_x - N_x)} \right) |0\rangle_x\langle 0| = \\ e^{-N_x} \left((\eta_x \hat{n}_x + N_x) \left(1 + \sum_{k=1}^{\infty} \frac{(-1)^k}{k!} \eta_x^k \hat{n}_x^k \right) \right) |0\rangle_x\langle 0| &= \\ N_x e^{-N_x} |0\rangle_x\langle 0|, \end{aligned} \quad (41)$$

$$\begin{aligned} \hat{\Pi}_x^{(1)}|1\rangle_x\langle 1| &= e^{-N_x} \left((\eta_x \hat{n}_x + N_x) \left(1 - \eta_x \hat{n}_x + \sum_{k=2}^{\infty} \frac{(-1)^k}{k!} \eta_x^k \hat{n}_x^k \right) \right) \\ |1\rangle_x\langle 1| &= (\eta_x + N_x (1 - \eta_x)) e^{-N_x} |1\rangle_x\langle 1|, \end{aligned} \quad (42)$$

$$\begin{aligned} \hat{\Pi}_x^{(1)}|2\rangle_x\langle 2| &= e^{-N_x} (\eta_x \hat{n}_x + N_x) \left(1 - \eta_x \hat{n}_x + \frac{1}{2} \eta_x^2 \hat{n}_x^2 + \right. \\ \left. \sum_{k=3}^{\infty} \frac{(-1)^k}{k!} \eta_x^k \hat{n}_x^k \right) |2\rangle_x\langle 2| &= (2\eta_x - 2\eta_x^2 + N_x (1 - 2\eta_x + \eta_x^2)) \\ e^{-N_x} |2\rangle_x\langle 2| &= (1 - \eta_x) (2\eta_x + N_x (1 - \eta_x)) e^{-N_x} |2\rangle_x\langle 2|, \end{aligned} \quad (43)$$

$$\begin{aligned} \hat{\Pi}_x^{(2)}|0\rangle_x\langle 0| &= \left(\frac{1}{2} (\eta_x^2 \hat{n}_x^2 + 2N_x \eta_x \hat{n}_x + N_x^2) e^{(-\eta_x \hat{n}_x - N_x)} \right) |0\rangle_x\langle 0| = \\ \frac{1}{2} e^{-N_x} \left((\eta_x^2 \hat{n}_x^2 + 2N_x \eta_x \hat{n}_x + N_x^2) \left(1 + \sum_{k=1}^{\infty} \frac{(-1)^k}{k!} \eta_x^k \hat{n}_x^k \right) \right) |0\rangle_x\langle 0| &= \\ \frac{1}{2} N_x^2 e^{-N_x} |0\rangle_x\langle 0|, \end{aligned} \quad (44)$$

$$\begin{aligned} \hat{\Pi}_x^{(2)}|1\rangle_x\langle 1| &= \frac{1}{2} e^{-N_x} \left((\eta_x^2 \hat{n}_x^2 + 2N_x \eta_x \hat{n}_x + N_x^2) (1 - \eta_x \hat{n}_x + \right. \\ \left. \sum_{k=2}^{\infty} \frac{(-1)^k}{k!} \eta_x^k \hat{n}_x^k) \right) |1\rangle_x\langle 1| &= \frac{1}{2} (2N_x \eta_x + N_x^2 (1 - \eta_x)) e^{-N_x} |1\rangle_x\langle 1| = \\ N_x \left(\eta_x + \frac{1}{2} N_x (1 - \eta_x) \right) e^{-N_x} |1\rangle_x\langle 1|, \end{aligned} \quad (45)$$

$$\begin{aligned} \hat{\Pi}_x^{(2)}|2\rangle_x\langle 2| &= \frac{1}{2} e^{-N_x} \left((\eta_x^2 \hat{n}_x^2 + 2N_x \eta_x \hat{n}_x + N_x^2) (1 - \eta_x \hat{n}_x + \frac{1}{2} \eta_x^2 \hat{n}_x^2 + \right. \\ \left. + N_x^2 (1 - \eta_x)^2) e^{-N_x} |2\rangle_x\langle 2| &= \left(\eta_x^2 + 2\eta_x N_x (1 - \eta_x) + \frac{1}{2} N_x^2 (1 - \eta_x)^2 \right) e^{-N_x} |2\rangle_x\langle 2|. \end{aligned} \quad (46)$$

Let us consider the situation with identical detectors and identical values of the background noise. We will reveal the dependencies between the model parameters and the probabilities (35)–(37). In this case $\eta_x = \eta_D$ and $N_x = N_D$ for all $x \in \{1, 2, 3, 4\}$.

Trace is a linear operator. Correspondingly, one can calculate the probabilities separately for density operators $\hat{\rho}_{vac}, \hat{\rho}_A, \hat{\rho}_B, \hat{\rho}_{Bell}$ and obtain the result as a linear combination with coefficients (31)–(34). Particularly, for $\hat{\rho}_{(vac)}$ one has:

$$P_{00}(\hat{\rho}_{vac}) = P_{10}(\hat{\rho}_{vac}) = 2 \text{Tr} \left(N_D^2 e^{-4N_D} \hat{\rho}_{vac} \right) = 2 N_D^2 e^{-4N_D}, \quad (47)$$

$$P_{01}(\hat{\rho}_{vac}) = P_{11}(\hat{\rho}_{vac}) = \frac{1}{2} \cdot 4 \text{Tr} \left(\frac{1}{2} N_D^2 e^{-4N_D} \hat{\rho}_{vac} \right) = N_D^2 e^{-4N_D}. \quad (48)$$

Before calculating $\hat{\rho}_A, \hat{\rho}_B$, let us consider

$$Tr\left(\hat{\Pi}_1^1 \hat{\Pi}_2^1 \hat{\Pi}_3^0 \hat{\Pi}_4^0 \hat{\rho}_A\right)$$

and

$$Tr\left(\hat{\Pi}_1^2 \hat{\Pi}_2^0 \hat{\Pi}_3^0 \hat{\Pi}_4^0 \hat{\rho}_A\right).$$

$$\begin{aligned} Tr\left(\hat{\Pi}_1^1 \hat{\Pi}_2^1 \hat{\Pi}_3^0 \hat{\Pi}_4^0 \hat{\rho}_A\right) &= Tr\left(\hat{\Pi}_1^1 \hat{\Pi}_2^1 \hat{\Pi}_3^0 \hat{\Pi}_4^0 (|\gamma\rangle_{1D} \langle \gamma|_{1D} + |\gamma\rangle_{2D} \langle \gamma|_{2D})\right) = \\ &= Tr\left(\hat{\Pi}_1^1 \hat{\Pi}_2^1 \hat{\Pi}_3^0 \hat{\Pi}_4^0 (|1000\rangle \langle 1000| - |0010\rangle \langle 1000| - |1000\rangle \langle 0010| + |0010\rangle \langle 0010| + \right. \\ &\quad \left. + |0100\rangle \langle 0100| - |0100\rangle \langle 0001| - |0001\rangle \langle 0100| + |0001\rangle \langle 0001|\right), \end{aligned}$$

$$\begin{aligned} Tr\left(\hat{\Pi}_1^1 \hat{\Pi}_2^1 \hat{\Pi}_3^0 \hat{\Pi}_4^0 \hat{\rho}_B\right) &= Tr\left(\hat{\Pi}_1^1 \hat{\Pi}_2^1 \hat{\Pi}_3^0 \hat{\Pi}_4^0 (|\gamma\rangle_{3D} \langle \gamma|_{3D} + |\gamma\rangle_{4D} \langle \gamma|_{4D})\right) = \\ &= Tr\left(\hat{\Pi}_1^1 \hat{\Pi}_2^1 \hat{\Pi}_3^0 \hat{\Pi}_4^0 (|1000\rangle \langle 1000| + |0010\rangle \langle 1000| + |1000\rangle \langle 0010| + |0010\rangle \langle 0010| + \right. \\ &\quad \left. + |0100\rangle \langle 0100| + |0100\rangle \langle 0001| + |0001\rangle \langle 0100| + |0001\rangle \langle 0001|\right). \end{aligned}$$

To find a trace, one is interested in diagonal elements only. Hence,

$$Tr\left(\hat{\Pi}_1^{x1} \hat{\Pi}_2^{x2} \hat{\Pi}_3^{x3} \hat{\Pi}_4^{x4} \hat{\rho}_A\right) = Tr\left(\hat{\Pi}_1^{x1} \hat{\Pi}_2^{x2} \hat{\Pi}_3^{x3} \hat{\Pi}_4^{x4} \hat{\rho}_B\right).$$

Consequently,

$$\begin{aligned} Tr\left(\hat{\Pi}_1^1 \hat{\Pi}_2^1 \hat{\Pi}_3^0 \hat{\Pi}_4^0 \hat{\rho}_A\right) &= Tr\left(\hat{\Pi}_1^1 \hat{\Pi}_2^1 \hat{\Pi}_3^0 \hat{\Pi}_4^0 \hat{\rho}_B\right) = 2(\eta_D + N_D(1 - \eta_D)) N_D e^{-4N_D} + \\ &2(1 - \eta_D) N_D^2 e^{-4N_D} = 2N_D \left((\eta_D + 2N_D(1 - \eta_D)) \right) e^{-4N_D}, \end{aligned} \tag{49}$$

$$\begin{aligned} Tr\left(\hat{\Pi}_1^2 \hat{\Pi}_2^0 \hat{\Pi}_3^0 \hat{\Pi}_4^0 \hat{\rho}_A\right) &= Tr\left(\hat{\Pi}_1^2 \hat{\Pi}_2^0 \hat{\Pi}_3^0 \hat{\Pi}_4^0 \hat{\rho}_B\right) = \left(\eta_D + \frac{1}{2} N_D (1 - \eta_D) \right) N_D e^{-4N_D} + \\ &+ \frac{3}{2} (1 - \eta_D) N_D^2 e^{-4N_D} = N_D \left((\eta_D + 2N_D(1 - \eta_D)) \right) e^{-4N_D}. \end{aligned} \tag{50}$$

Using (49) and (50), one obtains the probabilities for the density operator $\hat{\rho}_A, \hat{\rho}_B$:

$$P_{00}(\hat{\rho}_A) = P_{00}(\hat{\rho}_B) = P_{10}(\hat{\rho}_A) = P_{10}(\hat{\rho}_B) = 4N_D \left((\eta_D + 2N_D(1 - \eta_D)) \right) e^{-4N_D}, \tag{51}$$

$$P_{01}(\hat{\rho}_A) = P_{01}(\hat{\rho}_B) = P_{11}(\hat{\rho}_A) = P_{11}(\hat{\rho}_B) = 2N_D \left((\eta_D + 2N_D(1 - \eta_D)) \right) e^{-4N_D}. \tag{52}$$

Let us calculate the probabilities for the density operator $\hat{\rho}_{Belb}$, which takes different forms for different Alice's coding: $\hat{\rho}_{00}, \hat{\rho}_{01}, \hat{\rho}_{10}, \hat{\rho}_{11}$:

$$\begin{aligned} P_{00}(\hat{\rho}_{00}) &= \left(\frac{1}{2} (\eta_D + N_D(1 - \eta_D))^2 e^{-4N_D} + \frac{1}{2} N_D^2 (1 - \eta_D)^2 e^{-4N_D} \right) + \\ &\left(\frac{1}{2} N_D^2 (1 - \eta_D)^2 e^{-4N_D} + \frac{1}{2} (\eta_D + N_D(1 - \eta_D))^2 e^{-4N_D} \right) = \\ &(\eta_D^2 + 2N_D(1 - \eta_D)(\eta_D + N_D(1 - \eta_D))) e^{-4N_D}, \end{aligned} \tag{53}$$

$$P_{10}(\hat{\rho}_{00}) = 4 \left(\frac{1}{2} (\eta_D + N_D (1 - \eta_D)) (1 - \eta_D) N_D e^{-4N_D} \right) = 2N_D (1 - \eta_D) (\eta_D + N_D (1 - \eta_D)) e^{-4N_D}, \quad (54)$$

$$P_{01}(\hat{\rho}_{00}) = P_{11}(\hat{\rho}_{00}) = \frac{1}{2} \cdot 4 (N_D \left(\eta_D + \frac{1}{2} N_D (1 - \eta_D) \right) (1 - \eta_D) e^{-4N_D} + \frac{1}{2} N_D^2 (1 - \eta_D)^2 e^{-4N_D}) = 2N_D (1 - \eta_D) (\eta_D + N_D (1 - \eta_D)) e^{-4N_D}, \quad (55)$$

$$P_{00}(\hat{\rho}_{10}) = 4 \left(\frac{1}{2} (\eta_D + N_D (1 - \eta_D)) (1 - \eta_D) N_D e^{-4N_D} \right) = 2N_D (1 - \eta_D) (\eta_D + N_D (1 - \eta_D)) e^{-4N_D}, \quad (56)$$

$$P_{10}(\hat{\rho}_{10}) = \left(\frac{1}{2} (\eta_D + N_D (1 - \eta_D))^2 e^{-4N_D} + \frac{1}{2} N_D^2 (1 - \eta_D)^2 e^{-4N_D} \right) + \left(\frac{1}{2} N_D^2 (1 - \eta_D)^2 e^{-4N_D} + \frac{1}{2} (\eta_D + N_D (1 - \eta_D))^2 e^{-4N_D} \right) = (\eta_D^2 + 2N_D (1 - \eta_D) (\eta_D + N_D (1 - \eta_D))) e^{-4N_D}, \quad (57)$$

$$P_{01}(\hat{\rho}_{10}) = P_{11}(\hat{\rho}_{10}) = \frac{1}{2} \cdot 4 (N_D \left(\eta_D + \frac{1}{2} N_D (1 - \eta_D) \right) (1 - \eta_D) e^{-4N_D} + \frac{1}{2} N_D^2 (1 - \eta_D)^2 e^{-4N_D}) = 2N_D (1 - \eta_D) (\eta_D + N_D (1 - \eta_D)) e^{-4N_D}, \quad (58)$$

$$P_{00}(\hat{\rho}_{01}) = P_{00}(\hat{\rho}_{11}) = P_{10}(\hat{\rho}_{01}) = P_{10}(\hat{\rho}_{11}) = 4 \cdot \frac{1}{4} \left((1 - \eta_D) (2\eta_D + N_D (1 - \eta_D)) N_D e^{-4N_D} + N_D^2 (1 - \eta_D)^2 e^{-4N_D} \right) = 2N_D (1 - \eta_D) (\eta_D + N_D (1 - \eta_D)) e^{-4N_D}, \quad (59)$$

$$P_{01}(\hat{\rho}_{01}) = P_{11}(\hat{\rho}_{01}) = P_{01}(\hat{\rho}_{11}) = P_{11}(\hat{\rho}_{11}) = \frac{1}{2} \cdot 4 \cdot \frac{1}{4} ((\eta_D^2 + 2\eta_D N_D (1 - \eta_D) + \frac{1}{2} N_D^2 (1 - \eta_D)^2) e^{-4N_D} + 3 \cdot \frac{1}{2} N_D^2 (1 - \eta_D)^2 e^{-4N_D}) = \frac{1}{2} (\eta_D^2 + 2N_D (1 - \eta_D) (\eta_D + N_D (1 - \eta_D))) e^{-4N_D}. \quad (60)$$

It is necessary to perform a post-selection of obtained results. In fact, it means to make a normalization of obtained values. We calculate sums of probabilities:

$$S_{00|10} = p_{vac} (8N_D^2 e^{-4N_D}) + (p_A + p_B) (16N_D (\eta_D + 2N_D (1 - \eta_D))) e^{-4N_D} + p_{Bell} (8N_D (1 - \eta_D) (\eta_D + N_D (1 - \eta_D)) + \eta_D^2) e^{-4N_D} \quad (61)$$

$$S_{01|11} = p_{vac} (4N_D^2 e^{-4N_D}) + (p_A + p_B) (8N_D (\eta_D + 2N_D (1 - \eta_D))) e^{-4N_D} + p_{Bell} (6N_D (1 - \eta_D) (\eta_D + N_D (1 - \eta_D)) + \eta_D^2) e^{-4N_D} \quad (62)$$

Then, (51)–(62) give one the following values of the probabilities in question:

$$P_{00 \rightarrow 00} = P_{10 \rightarrow 10} = \frac{2p_{vac}N_D^2 + 4(p_A + p_B)(N_D(\eta_D + 2N_D(1-\eta_D))) + p_{Bell}(2N_D(1-\eta_D)(\eta_D + N_D(1-\eta_D))) + 8p_{vac}N_D^2 + 16(p_A + p_B)(N_D(\eta_D + 2N_D(1-\eta_D))) + p_{Bell}(8N_D(1-\eta_D)(\eta_D + N_D(1-\eta_D))) + \eta_D^2}{8p_{vac}N_D^2 + 16(p_A + p_B)(N_D(\eta_D + 2N_D(1-\eta_D))) + p_{Bell}(8N_D(1-\eta_D)(\eta_D + N_D(1-\eta_D))) + \eta_D^2} \quad (63)$$

$$P_{00 \rightarrow 10} = P_{10 \rightarrow 00} = \frac{2p_{vac}N_D^2 + 4(p_A + p_B)(N_D(\eta_D + 2N_D(1-\eta_D))) + p_{Bell}(2N_D(1-\eta_D)(\eta_D + N_D(1-\eta_D)))}{8p_{vac}N_D^2 + 16(p_A + p_B)(N_D(\eta_D + 2N_D(1-\eta_D))) + p_{Bell}(8N_D(1-\eta_D)(\eta_D + N_D(1-\eta_D))) + \eta_D^2} \quad (64)$$

$$P_{01 \rightarrow 00} = P_{11 \rightarrow 00} = P_{01 \rightarrow 10} = P_{11 \rightarrow 10} = \frac{2p_{vac}N_D^2 + 4(p_A + p_B)(N_D(\eta_D + 2N_D(1-\eta_D))) + p_{Bell}(2N_D(1-\eta_D)(\eta_D + N_D(1-\eta_D)))}{8p_{vac}N_D^2 + 16(p_A + p_B)(N_D(\eta_D + 2N_D(1-\eta_D))) + p_{Bell}(8N_D(1-\eta_D)(\eta_D + N_D(1-\eta_D))) + \eta_D^2} \quad (65)$$

$$P_{00 \rightarrow 01} = P_{00 \rightarrow 11} = P_{10 \rightarrow 01} = P_{10 \rightarrow 11} = \frac{p_{vac}N_D^2 + 2(p_A + p_B)(N_D(\eta_D + 2N_D(1-\eta_D))) + p_{Bell}(2N_D(1-\eta_D)(\eta_D + N_D(1-\eta_D)))}{4p_{vac}N_D^2 + 8(p_A + p_B)(N_D(\eta_D + 2N_D(1-\eta_D))) + p_{Bell}(6N_D(1-\eta_D)(\eta_D + N_D(1-\eta_D))) + \eta_D^2} \quad (66)$$

$$P_{01 \rightarrow 01} = P_{11 \rightarrow 11} = P_{01 \rightarrow 11} = P_{11 \rightarrow 01} = \frac{p_{vac}N_D^2 + 2(p_A + p_B)(N_D(\eta_D + 2N_D(1-\eta_D))) + p_{Bell}\left(\frac{1}{2}\eta_D^2 + N_D(1-\eta_D)(\eta_D + N_D(1-\eta_D))\right)}{4p_{vac}N_D^2 + 8(p_A + p_B)(N_D(\eta_D + 2N_D(1-\eta_D))) + p_{Bell}(6N_D(1-\eta_D)(\eta_D + N_D(1-\eta_D))) + \eta_D^2} \quad (67)$$

where $P_{a_1a_2 \rightarrow b_1b_2}$ means that bits a_1a_2 are encoded by Alice and bits b_1b_2 are distinguished by Bob.

These probabilities were calculated numerically. We suppose that the time interval when Alice was coding her qubit is so small, that one can assume that qubits were sent to Bob at the same time and went through the same path. Hence, one can simply set $|T_A|^2 = |T_B|^2 = \eta_{atm}$, where η_{atm} is the fluctuating atmospheric efficiency, which is a random characteristic. In accordance with the (Gumberidze et al. 2016) the efficiency distribution could be described by lognormal distribution in strong turbulence conditions:

$$f(\eta_{atm}) = \frac{1}{\sqrt{2\pi}\sigma\eta_{atm}} \exp\left(-\frac{1}{2}\left(\frac{\ln\eta_{atm} + \bar{\theta}}{\sigma}\right)^2\right), \quad (68)$$

where $\bar{\theta} = -\ln\eta_{atm}$ characterizes the mean atmospheric losses, σ (the variance of $\theta = -\ln\eta_{atm}$) characterizes the atmosphere turbulence. This distribution can be applied only for $\sigma = \bar{\theta}$. We used the data from (Semenov, Vogel 2010) for calculations.

Discussion

So, what is the meaning of Expressions (63)–(67)? Firstly, Expression (67) shows that in one case the transmitted pair of bits is recognized correctly, and in the second it is incorrect, and these cases occur with equal probability. That is, this model has no way to distinguish pairs of bits 01 and 11.

Secondly, for every event that did not save the result (except (67)), the probability is a multiple of N_D . This means that if it is possible to reduce this indicator to zero, then this model will ideally implement the superdense coding algorithm, with the exception of the indistinguishability of bits 01 and 11. This can be seen in the graph below (Figure 4).

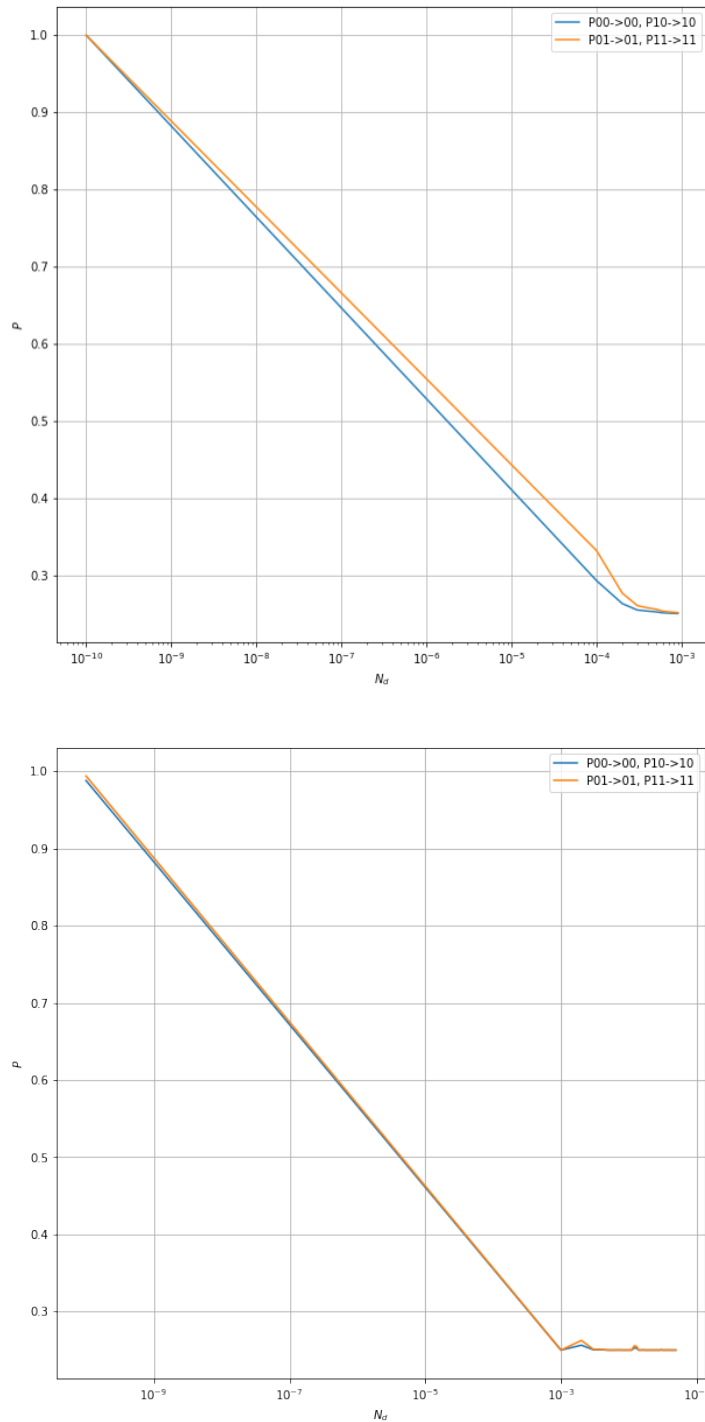


Fig. 4. Probability of correct recognition via the mean value of levels of the dark counts N_D ; the detection efficiency $\eta_D = 0.25$, the mean atmospheric losses are $\bar{\theta} = 7.36$, turbulence parameter: left: $\sigma = 0.1$, right: $\sigma = 2$

To analyze the results, it is important to understand that the minimum probability of correct operation of the algorithm is $1/3$ and $1/6$. Fixing one of the events (35)–(37) on the detectors, we understand which pair of bits was sent. In the worst case, events happen randomly, and as a result, we actually guess the forwarded bits, and the probability that we will guess is $1/3$ for bits $00|10$ and $1/6$ for bits $01|11$.

The graphs in Figures 4 and 5 show the dependencies of correct recognition on the number of dark counts for different values of the turbulence parameter. The values of atmospheric efficiency were generated randomly in accordance with the lognormal probability distribution. Figure 4 shows that adequate results of the algorithm (about 80 per cent recognition of bits $00|10$) are obtained at $N_D \approx 10^{-8}$. But even about $N_D \approx 2 \cdot 10^{-6}$, the probabilities of correct recognition are close to random. We can also see that the

more we increase the value σ , the more different are the results (Figure 5). So when the turbulence instability is higher, the results may be less predictable.

Analyzing the influence of the detectors efficiency η_D , one obtains the following dependence (Fig. 5).

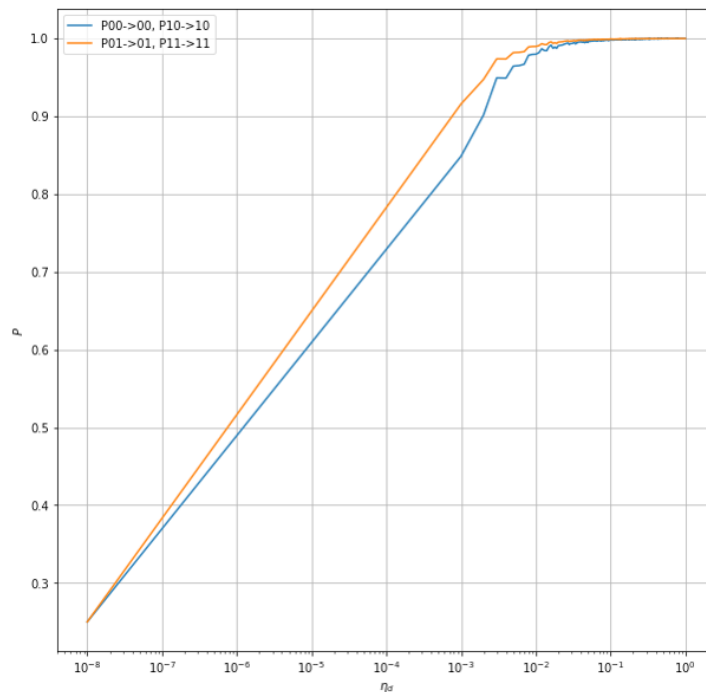


Fig. 5. Probability of correct recognition via the detectors efficiency η_D , $\sigma = 0.1$, $N_D = 10^{-8}$, the mean atmospheric losses are $\bar{\theta} = 7.36$

It follows from the graph that the recognition errors are small enough if detectors efficiency exceeds the value of about 10^{-3} .

Summarizing the results, one can mention that for the suggested theoretical model of a quantum channel for the implementation of the superdense coding quantum algorithm, the most important factors include the turbulence instability, detectors efficiency and the mean level of noise counts caused by the background radiation and the dark counts.

Conflict of interest

The authors declare that there is no conflict of interest, either existing or potential.

Authors contribution

The authors have made an equal contribution to the paper.

References

- Adam, I. A., Yashin, D. A., Kargina, D. A., Nasedkina, B. A. (2022) Comparison of Gaussian and vortex beams in free-space QKD with phase encoding in turbulent atmosphere. *Nanosystems: Physics, Chemistry, Mathematics*, 13 (4), 392–403. <https://doi.org/10.17586/2220-8054-2022-13-4-392-403> (In English)
- Bennett, C. H., Wiesner, S. J. (1992) Communication via one- and two-particle operators on Einstein-Podolsky-Rosen states. *Physical Review Letters*, 69 (20), article 2881. <https://doi.org/10.1103/PhysRevLett.69.2881> (In English)
- Bohmann, M., Semenov, A. A., Sperling, J., Vogel, W. (2016) Gaussian entanglement in the turbulent atmosphere. *Physical Review A*, 94 (1), article 010302(R). <https://doi.org/10.1103/PhysRevA.94.010302> (In English)
- Dong, R., Lassen, M. O., Heersink, J. et al. (2008) Experimental entanglement distillation of mesoscopic quantum states. *Nature Physics*, 4 (12), 919–923. <https://doi.org/10.1038/nphys1112> (In English)

- Elser, D., Bartley, T., Heim, B. et al. (2009) Feasibility of free space quantum key distribution with coherent polarization states. *New Journal of Physics*, 11, article 045014. <https://doi.org/10.1088/1367-2630/11/4/045014> (In English)
- Faleeva, M. P., Popov, I. Y. (2020a) Entanglement transmission through turbulent atmosphere for modes of Gaussian beam. *Quantum Information Processing*, 19 (2), article 72. <https://doi.org/10.1007/s11128-019-2569-y> (In English)
- Faleeva, M. P., Popov, I. Y. (2020b) On quantum bit coding by Gaussian beam modes for the quantum key distribution. *Nanosystems: Physics, Chemistry, Mathematics*, 11 (6), 651–658. <https://doi.org/10.17586/2220-8054-2020-11-6-651-658> (In English)
- Faleeva, M. P., Popov, I. Y. (2022) Singular numbers, entangled qubits transmission through a turbulent atmosphere and teleportation. *Indian Journal of Physics*, 96 (8), 2501–2505. <https://doi.org/10.1007/s12648-021-02143-9> (In English)
- Fedrizzi, A., Ursin, R., Herbst, T. et al. (2009) High-fidelity transmission of entanglement over a high-loss free-space channel. *Nature Physics*, 5, 389–392. <https://doi.org/10.1038/nphys1255> (In English)
- Gilev, P. A., Popov, I. Y. (2019) Quantum image transmission based on linear elements. *Nanosystems: Physics, Chemistry, Mathematics*, 10 (4), 410–414. <https://doi.org/10.17586/2220-8054-2019-10-4-410-414> (In English)
- Gumberidze, M. O., Semenov, A. A., Vasylyev, D., Vogel, W. (2016) Bell nonlocality in the turbulent atmosphere. *Physical Review A*, 94 (5), article 053801. <https://doi.org/10.1103/PhysRevA.94.053801> (In English)
- Heersink, J., Marquardt, Ch., Dong, R. et al. (2006) Distillation of squeezing from non-gaussian quantum states. *Physical Review Letters*, 96 (25), article 253601. <https://doi.org/10.1103/PhysRevLett.96.253601> (In English)
- Herbst, T., Scheidl, T., Fink, M. et al. (2015) Teleportation of entanglement over 143 km. *Proceedings of National Academy of Sciences*, 112 (46), 14202–14205. <https://doi.org/10.1073/pnas.1517007112> (In English)
- Ishimaru, A. (1978) *Wave propagation and scattering in random media. Vol. 1*. New York: Academic Press, 339 p. <https://doi.org/10.1016/B978-0-12-374701-3.X5001-7> (In English)
- Mandel, L., Wolf, E. (1995) *Optical coherence and quantum optics*. Cambridge: Cambridge University Press, 1192 p. (In English)
- Mattle, K., Weinfurter, H., Kwiat, P. G. et al. (1996) Dense coding in experimental quantum communication. *Physical Review Letters*, 76 (25), article 4656. <https://doi.org/10.1103/PhysRevLett.76.4656> (In English)
- Nielsen, M. A., Chuang, I. L. (2010) *Quantum computation and quantum information*. Cambridge: Cambridge University Press, 670 p. (In English)
- Peters, N., Altepeter, J., Jeffrey, E. et al. (2003) Precise creation, characterization, and manipulation of single optical qubits. *Quantum Information Computation*, 3, 503–518. <https://doi.org/10.48550/arXiv.quant-ph/0502177> (In English)
- Schleich, W. P. (2001) *Quantum optics in phase space*. Berlin: WILEY-VCH Verlag, 695 p. <https://doi.org/10.1002/3527602976> (In English)
- Semenov, A. A., Turchin, A. V., Gomonay, H. V. (2008) Detection of quantum light in the presence of noise. *Physical Review A*, 78 (5), article 055803. <https://doi.org/10.1103/PhysRevA.78.055803> (In English)
- Semenov, A. A., Turchin, A. V., Gomonay, H. V. (2009) Erratum: Detection of quantum light in the presence of noise [Phys. Rev. A 78, 055803 (2008)]. *Physical Review A*, 79 (1), article 019902. <https://doi.org/10.1103/PhysRevA.79.019902> (In English)
- Semenov, A. A., Vogel, W. (2009) Quantum light in the turbulent atmosphere. *Physical Review A*, 80 (2), article 021802(R). <https://doi.org/10.1103/PhysRevA.80.021802> (In English)
- Semenov, A. A., Vogel, W. (2010) Entanglement transfer through the turbulent atmosphere. *Physical Review A*, 81 (2), article 023835. <https://doi.org/10.1103/PhysRevA.81.023835> (In English)
- Soderholm, J., Bjork, G., Klimov, A. B., Sanchez-Soto, L. L., Leuchs, G. (2012) Quantum polarization characterization and tomography. *New Journal of Physics*, 14 (11), article 115014. <https://doi.org/10.1088/1367-2630/14/11/115014> (In English)
- Tatarskii, V. I. (1971) *Effect of the turbulent atmosphere on wave propagation*. Jerusalem: Israel Program for Scientific Translations Publ., 488 p. (In English)
- Ursin, R., Tiefenbacher, F., Schmitt-Manderbach, T. et al. (2007) Entanglement-based quantum communication over 144 km. *Nature Physics*, 3 (7), 481–486. <https://doi.org/10.1038/nphys629> (In English)
- Vasylyev, D., Semenov, A. A., Vogel, W. (2016) Atmospheric quantum channels with weak and strong turbulence. *Physical Review Letters*, 117 (9), article 090501. <https://doi.org/10.1103/PhysRevLett.117.090501> (In English)
- Williams, B., Sadlier, R., Humble, T. (2018) Superdense coding for quantum networking environments. *Proceedings. Vol. 10547. Advances in Photonics of Quantum Computing, Memory, and Communication XI*. San Francisco: SPIE OPTO Publ., article 105470B. <https://doi.org/10.1117/12.2295016> (In English)



Check for updates

Physics of Semiconductors. Phase equilibria
and phase transitions

UDC 538.9

EDN XIVVYW

<https://www.doi.org/10.33910/2687-153X-2022-3-4-202-213>

Polarization processes in silver iodide films near the superionic phase transition temperature

A. V. Ilinskiy¹, E. B. Shadrin¹, R. A. Castro Arata², I. O. Popova^{✉1}

¹ Ioffe Physical-Technical Institute, 26 Politekhnicheskaya Str., Saint Petersburg 194021, Russia

² Herzen State Pedagogical University of Russia, 48 Moika Emb., Saint Petersburg 191186, Russia

Authors

Aleksandr V. Ilinskiy, ORCID: e-mail: ilinskiy@mail.ioffe.ru

Evgenii B. Shadrin, ORCID: [0000-0002-1423-2852](https://orcid.org/0000-0002-1423-2852), e-mail: jenjasha@yandex.ru

Rene A. Castro Arata, ORCID: [0000-0002-1902-5801](https://orcid.org/0000-0002-1902-5801), e-mail: recastro@mail.ru

Irina O. Popova, ORCID: [0000-0002-0822-985X](https://orcid.org/0000-0002-0822-985X), e-mail: timof-ira@yandex.ru

For citation: Ilinskiy, A. V., Shadrin, E. B., Castro Arata, R. A., Popova, I. O. (2022) Polarization processes in silver iodide films near the superionic phase transition temperature. *Physics of Complex Systems*, 3 (4), 202–213.

<https://www.doi.org/10.33910/2687-153X-2022-3-4-202-213> EDN XIVVYW

Received 17 September 2022; reviewed 2 October 2022; accepted 2 October 2022.

Funding: The research was supported by the Ministry of Education of the Russian Federation as part of the state-commissioned assignment (Project No. FSZN-2020-0026).

Copyright: © A. V. Ilinskiy, E. B. Shadrin, R. A. Castro Arata, I. O. Popova (2022). Published by Herzen State Pedagogical University of Russia. Open access under [CC BY-NC License 4.0](https://creativecommons.org/licenses/by-nc/4.0/).

Abstract. The article reports the results of dielectric spectroscopy analysis exploring polarization processes in silver iodide nanocrystalline films in the region of thermal superionic phase transition. It also provides calculations of the system's relaxation and energy parameters. The abrupt change of parameters at the transition point is demonstrated by activation energy of semiconductor conduction and commit phases, indicator of the degree of frequency dependence of conductivity, and the maximum value of the function of the tangent of the dielectric loss angle. The article proposes a model of the micro-mechanism of the thermal phase transition from a semiconductor to a superionic state. It is shown that, along with the superionic phase transition, films undergo a percolation phase transition with the formation of a two-dimensional percolation cluster.

Keywords: superionic phase transition, silver iodide, dielectric spectroscopy, polarization processes, relaxation processes

Introduction

Solid-state ionic conductors, which include silver iodide, are being actively studied in connection with the prospects of their application. They are used in energy conservation devices, heavy-duty micro-data storage systems, as part of fiber-optic communication lines, etc. (Fokina et al. 2016; Makiura et al. 2009; Naik, Rabinal 2022; Sidorov et al. 2021).

Along with this, it is still of interest to study the mechanism of the thermal phase transition (PT) from a semiconductor to a superionic state at $T_c = 440$ K (147 °C) (Amrani et al. 2008; Johan et al. 2011), an issue that still remains unexplored.

According to (Vergent'eva et al. 2013), silver iodide exists in three different crystal forms. At $T = 293$ K (20 °C), AgI is a two-phase mixture of a cubic gamma phase with a zinc blende structure (F43m, $a = 6.495$ Å, $Z = 4$) and a hexagonal beta phase with a wurtzite structure (P63mc, $a = 4.592$ Å, $c = 7.510$ Å, $Z = 2$). The predominant phase at $T = 293$ K is the AgI gamma phase with a zinc blende structure (face-centered

cubic structure F43m). However, about 2% β -AgI with a hexagonal wurtzite structure P63mc are also present.

β -AgI becomes a stable phase above 384 K (111 °C). During the thermal phase transition it turns into a body-centered cubic α -AgI at 420 K (147 °C). This phase becomes stable above 420 K and is a superionic phase.

In the high-temperature superionic phase, iodine anions I form cubic cells with a cube edge equal to $a = 5.062 \text{ \AA}$ at 453 K (180 °C) (Wright, Fender 1977). Each Ag^+ cation is able to move along the crystal lattice, occupying 21 possible positions in succession. There are three different types of positions in total. There are 6 tetrahedral, 12 trigonal and 3 octahedral positions in a crystal cell. These three types of positions are crystallographically and energetically nonequivalent. Silver cations occupy such positions with different probabilities.

Analysis of the electron density distribution (Ivanov-Shits, Murin 2000) showed that mobile Ag^+ cations move freely throughout the crystal, except for the zones occupied by immobile Ag^+ and I anions, which stabilize the crystal lattice. This indicates the existence of conducting channels in the alpha phase of the AgI crystal, which interconnect the most probable spatial positions of Ag^+ .

Thus, the physical cause of the superionic PT is the thermal rearrangement of the crystal lattice structure upon reaching the PT temperature. This rearrangement creates the possibility of the appearance of positions free of silver ions. In this case, almost free migration of silver ions through the crystal lattice becomes possible under the action of an external electric field (Gurevich, Kharkats 1987). From this point of view, silver iodide (AgI) is a model system for studying the superionic phase transition.

Thus, it was shown in (Makiura et al. 2009) that silver iodide nanoparticles 11 nm in size coated with poly-N-vinyl-2-pyrrolidone (PVP) exhibit a decrease in the PT temperature to $T_c = 393 \text{ K}$ (120 °C) compared to single crystals, in which $T_c = 420 \text{ K}$ (147 °C). At room temperature, the conductivity of AgI with iodine-coated nanoparticles reaches $1.5 \times 10^{-2} \text{ \Omega}^{-1}\text{cm}^{-1}$. This is a record for ionic conductivity at $T = 293 \text{ K}$ for a binary compound.

The authors of (Vergent'eva et al. 2013) studied the behavior of the conduction property of an AgI-based composite embedded in porous glasses (average pore size about 7 nm) and opal (pore size 40–100 nm). They found that the temperature of the phase transition of nanoparticles in porous glasses and AgI opals decreases by 20 K, and the width of the temperature hysteresis loop of the phase transition doubles compared to free nanoparticles. The temperature dependence of the conductivity in this case has a thermally activated character.

Near the phase transition, the parameters of the function $\sigma(1/T)$ change, which indicates a change in the activation energy of conduction during the superionic phase transition. Thus, in the low temperature phase, the activation energy is 450–470 meV, while in the high temperature phase it is 100 meV.

It was also found that the effect of an anomalous increase in ionic conductivity can be observed when mixing two ionic conductors with the same cation, for example, in AgCl-AgI or AgBr-AgI systems. It was also found that the effect of an anomalous increase in ionic conductivity can be observed when mixing two ionic conductors with the same cation, for example, in AgCl-AgI or AgBr-AgI systems. The reason for this effect is that the common mobile ion, upon transition to the region with a lower chemical potential, increases the number of anion vacancies in the region of the space charge of one of the phases. At the same time, the number of interstitial cations increases in the other phase. This phenomenon is similar to the phenomenon of a sharp increase in ion transport in the near-contact region of two electronic conductors differing in chemical potentials (Ivanov-Shits, Murin 2000).

The above information formed the purpose of this work, which is to use dielectric spectroscopy to study polarization processes in nanocrystalline silver iodide films in the region of thermal superionic phase transition.

Experimental technique

Thin films of silver iodide were synthesized by thermal iodization (at 300 °C) of a layer of metallic silver 180 nm thick and 1 cm^2 in area, which was previously deposited on a glass substrate.

Silver contacts were deposited on the film surface, which ensured the planar geometry of the conductivity study.

The dielectric spectra of the layers under study (temperature-frequency dependence of the complex electrical impedance components) were obtained on a Concept-81 spectrometer (Novocontrol Technologies GmbH) in a wide range of frequencies ($f = 10^0 - 10^6 \text{ Hz}$) and temperatures ($T = 293 - 473 \text{ K}$).

In this case, the values of the real and imaginary parts of the complex impedance of the cell with the measured sample were measured:

$$Z^*(\omega) = R + \frac{1}{i\omega C} = Z' + iZ'' = \frac{U_0}{I^*(\omega)} \quad (1)$$

On this basis, the frequency spectra of the complex permittivity and complex conductivity were calculated:

$$\varepsilon^* = \varepsilon' - i\varepsilon'' = \frac{-i}{\omega Z^*(\omega) C_0} \quad (2)$$

$$\sigma^* = \sigma' - i\sigma'' = \frac{-i}{\omega Z^*(\omega) d} \quad (3)$$

where $C_0 = \frac{\varepsilon_0 S}{d}$ is the capacity of the cell without a sample. The relative error of the experiment did not exceed 5 %.

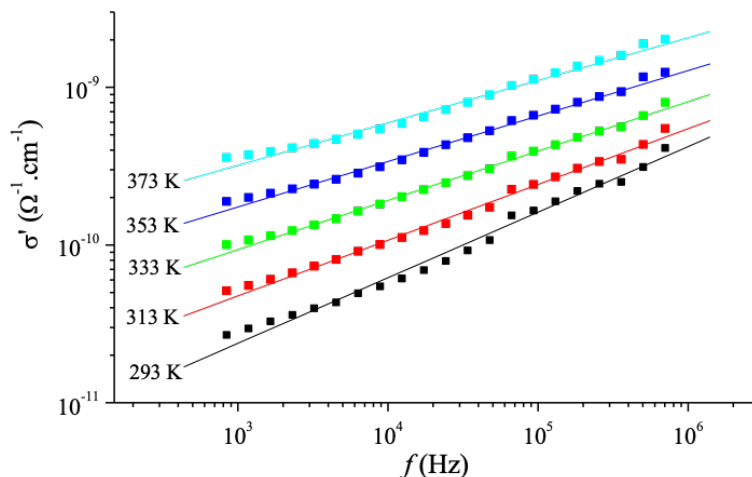
To calculate the values of the relaxation parameters of the system, the obtained dielectric spectra were approximated by the three-parameter Havriliak–Negami function (Kremer, Schonhals 2003). In this case, the computer programs of the Novocontrol Winfit spectrometer were used.

Experimental results with their preliminary analysis

The experiment showed that the frequency dependence of the specific conductivity σ' of thin AgI films increases with increasing frequency of the probing field (Fig. 1). This occurs at all temperatures. It is known (Mott, Davis 1982) that such a dependence of the conductivity on frequency is typical for many crystalline semiconductors and most amorphous semiconductors, for which the frequency dependence of the conductivity obeys the power law of growth:

$$\sigma(\omega) = A\omega^s, \quad (4)$$

where s is the exponent, A is a temperature-dependent constant, $\omega = 2\pi f$ is cyclic frequency.



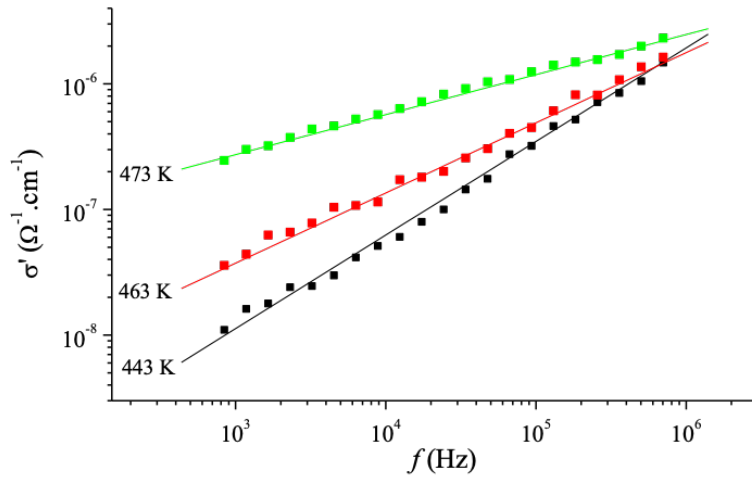


Fig. 1. Frequency dependence of specific conductivity σ' at different temperatures

The presence of Dependence (4) corresponds to the existence of a wide range of relaxators in the system, which have different relaxation times and create different mechanisms of dielectric losses.

The temperature dependence of the exponent s can be used to elucidate the features of the charge transfer mechanisms in the low-frequency range at temperatures of 293–473 K (Castro-Arata et al. 2021; Farid et al. 2005; Ulutas et al. 2013). This circumstance forced us to study the temperature dependence of the exponent s , which is shown in Fig. 2. This figure demonstrates the existence of two temperature regions: region I in the range $T = 293\text{--}433\text{ K}$ and region II at $T = 433\text{--}473\text{ K}$. As noted above, at a temperature of $T = 420\text{ K}$ silver iodide undergoes a structural change with a transition from the beta phase to the alpha phase. It can be argued with a high degree of probability that regions I and II correspond to the state of the system before and after the superionic phase transition, respectively.

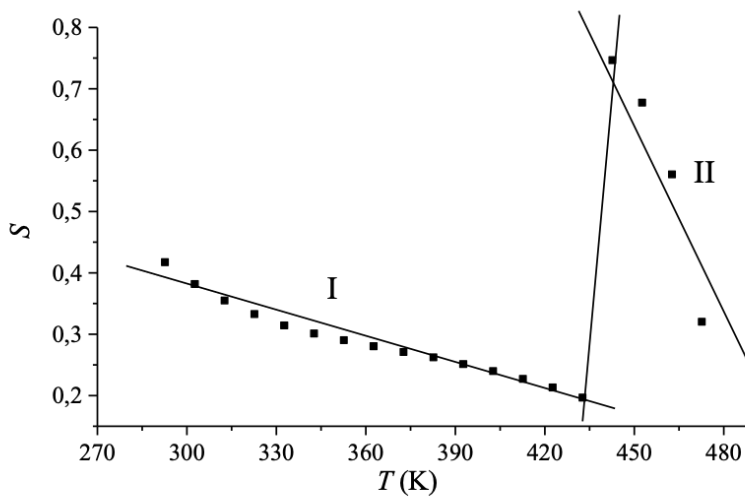


Fig. 2. Temperature dependence of the exponent s of the function $\sigma(\omega)$ for thin films of silver iodide

The found power Dependence (4) of the conductivity on frequency and the change in the value of the parameter s with increasing temperature allow us to assert the existence of a hopping mechanism of conductivity. In this case, charge carriers (ions, electrons) make thermally activated jumps through potential barriers in the structures of the semiconductor system.

The decrease in the exponent s in both phases with increasing temperature indicates the classical case of overcoming the energy barrier by charge carriers, according to the CBH model (correlated barrier hopping model) (Gurevich, Kharkats 1987). In this case, the expression for the conductivity on alternating current at a specific fixed temperature has the form (Makiura et al. 2009):

$$\sigma(\omega) = \frac{\pi^3 N^2 \varepsilon \varepsilon_0 \omega R_\omega^6}{24}, \quad (5)$$

here N is the density of states between which charge carriers jump, R_ω is jump length.

The relationship between the jump length R_ω and the height of the potential barrier is expressed by the relationship:

$$R_\omega = \frac{e^2}{\pi \varepsilon \varepsilon_0} \left[W_M - kT \ln \left(\frac{1}{\omega \tau_0} \right) \right]^{-1}, \quad (6)$$

where τ_0 is the characteristic relaxation time, the reciprocal of the phonon frequency ν_{ph} . On the other hand, the exponent s is related to the barrier height W_M by:

$$s = 1 - \frac{6kT}{W_M}, \quad (7)$$

As was shown in (Amrani et al. 2008), based on the obtained experimental data using Equations (5)–(7), it is possible to calculate the values of the conductivity parameters of the system N , R_ω and W_M at different temperatures. The results of the calculations are presented in Table 1.

Table 1. Values of the charge transfer parameters in thin films of silver iodide before (region I) and after (region II) the superionic phase transition

| T (K) | s | N (m ⁻³) | R_ω (m) | W_M (eV) |
|------------------|------|------------------------|----------------|------------|
| Region I | | | | |
| 293 | 0.41 | 1.08E22 | 2.46E-9 | 0.25 |
| 313 | 0.35 | 2.38E22 | 2.32E-9 | 0.24 |
| 333 | 0.31 | 4.77E22 | 2.17E-9 | 0.25 |
| 353 | 0.29 | 8.82E22 | 2.00E-9 | 0.26 |
| 373 | 0.28 | 1.57E23 | 1.85E-9 | 0.27 |
| Region II | | | | |
| 443 | 0.75 | 1.54E25 | 7.72E-11 | 0.92 |
| 463 | 0.55 | 3.99E27 | 4.27E-11 | 0.53 |
| 473 | 0.32 | 7.46E28 | 3.17E-11 | 0.36 |

Figure 3 shows the temperature dependence of the conductivity of silver iodide films in the coordinates $\ln[\sigma(\omega)] = \zeta(10^3/T)$. It shows that charge transfer is a thermally activated process. The existence of two temperature regions was found, at the temperature boundary between which a change in the slope of the graphs is observed at $T = 428$ K. This coincides to within 2% with $T_c = 420$ K (147 °C) of the super-

ionic phase transition. Before and after the PT, the conduction activation energies are as follows: $E_1 = 0.34$ eV before the transition and $E_2 = 1.63$ eV after the transition, respectively.

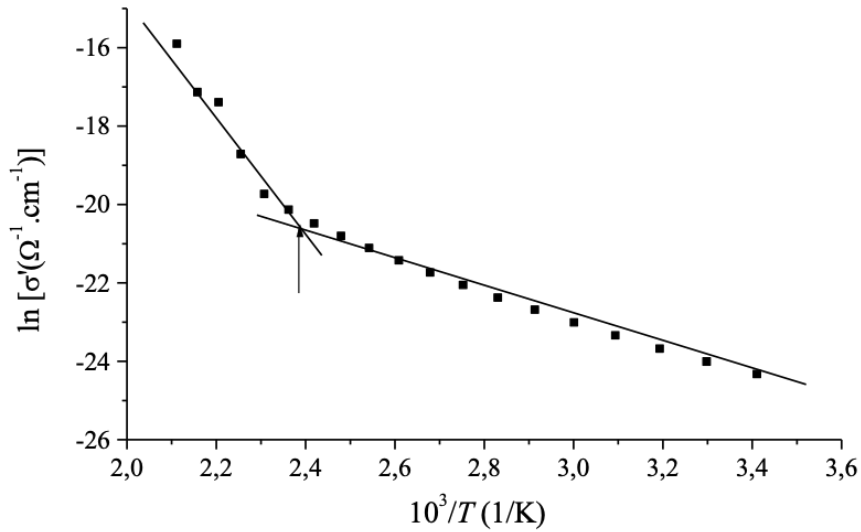


Fig. 3. Temperature dependence of specific conductivity σ' of thin films of silver iodide at frequency $f = 10^3$ Hz

Measurement of the dielectric loss tangent $\text{tg}\delta$ in AgI films at different temperatures (Fig. 4) revealed the existence of a loss maximum, which shifts to high frequencies with increasing temperature. In this case, the absolute value of the maximum of the function $\text{tg}\delta(\omega)$ at a temperature $T_c = 420$ K (this is a temperature of the transition of the AgI film to the superionic state) is halved.

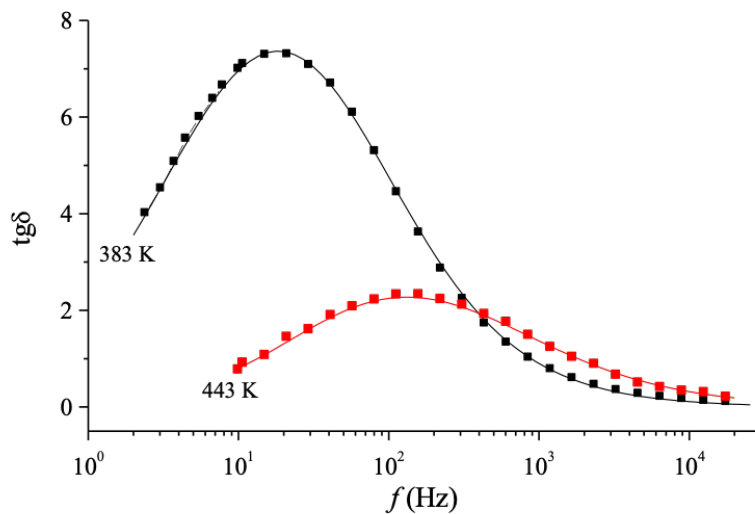


Fig. 4. Frequency dependence of the dielectric loss tangent $\text{tg}\delta = \epsilon''/\epsilon'$ at temperatures of 383 and 443 K. Solid lines are the approximation of the experiment by Function (8) taking into account the Havriliak–Negami Function (9). After the PT is completed, the temperature rises with a jump in the parameters of Function (9): $\tau = 0,08$ s \rightarrow $\tau = 0,009$ s, $\alpha = 0,98 \rightarrow \alpha = 97$, $\beta = 0,97 \rightarrow \beta = 0,93$

As an approximating function in the calculations, the Havriliak–Negami function was used (Volkov et al. 2018) in the form (8).

$$\varepsilon^*(\omega) = \varepsilon_\infty + (\varepsilon_s - \varepsilon_\infty) \int_0^\infty \frac{G(\tau)}{1 + i\omega\tau} d\tau, \tag{8}$$

where ε_s is the permittivity at extremely low frequencies, τ is the relaxation time. This function contains three variable parameters (τ_{HN} , α_{HN} and β_{HN}) for each type of grain and has the form:

$$G(\tau) = \frac{1}{\pi} \times \frac{(\tau/\tau_{HN})^{\beta(1-\alpha)} \sin(\beta\varphi)}{\left[(\tau/\tau_{HN})^{2(1-\alpha)} + 2(\tau/\tau_{HN})^{(1-\alpha)} \cos(\pi[1-\alpha]) + 1 \right]^{\beta/2}}, \tag{9}$$

where

$$\varphi = \arctg \left[\frac{\sin(\pi[1-\alpha])}{(\tau/\tau_{HN}) + \cos(\pi[1-\alpha])} \right].$$

Expression (8) together with expression (9) allow using the Havriliak–Negami function to approximate the frequency dependence function $\text{tg}\delta(\omega)$.

Conversely, empirical data on the frequency dependence of the function $\text{tg}\delta(\omega)$ make it possible to determine the parameters of the distribution function of relaxers from their relaxation times. The computer built into the spectrometer allows the fitting procedure and calculations to be carried out automatically.

Namely, in the first case, the value τ_{HNmax} is fixed, ω is a variable, and the theoretical curve is fitted to the experimental results, as shown in Fig. 4. At the same time, for $f_{max} = 20$ Hz, the values $\alpha_{HN} = 0.98$ ($T = 383$ K) and $\beta_{HN} = 0.97$ ($T = 383$ K) were obtained. For $f_{max} = 200$ Hz, the value $\alpha_{HN} = 0.97$ ($T = 383$ K) and $\beta_{HN} = 0.93$ ($T = 383$ K).

In the second case, the value ω_{max} is fixed in expression (8), and the parameter τ is a variable.

The parameters of the HN function reflect the average position of relaxers on the time scale (τ_{HN}), the degree of spread (α_{HN}), and the inhomogeneity (asymmetry) of the distribution of relaxers (β_{HN}) over relaxation times. The software of modern spectrometers makes it possible, as indicated, to obtain the HN function with coefficients τ_{HN} at their output. α_{HN} and β_{HN} are adjusted to the measurement results.

Table 2. Values of the relaxation parameters of thin films of silver iodide in the temperature region of the phase transition

| Temp. [K] | Tau-Max [s] | Alpha [] | Beta [] |
|-----------|-------------|------------|------------|
| 403 | 3.040e-01 | 1.0000e+00 | 9.4140e-01 |
| 413 | 7.272e-01 | 1.0000e+00 | 9.1930e-01 |
| 423 | 1.847e-01 | 1.0000e+00 | 9.1270e-01 |
| 433 | 2.093e+00 | 1.0000e+00 | 8.7950e-01 |
| 443 | 1.526e-02 | 9.7780e-01 | 8.3950e-01 |
| 453 | 8.530e-02 | 9.8060e-01 | 8.0000e-01 |
| 463 | 2.516e-02 | 9.8970e-01 | 6.7490e-01 |

The values of the relaxation parameters of AgI thin films obtained by approximating the experimental curves with a two-parameter empirical Havriliak–Negami function are presented in Table 2.

The analysis of data in Table 2 allows us to conclude that there are non-Debye mechanisms of dielectric relaxation in the region of the PT from a semiconductor to a superionic conductor. Attention is drawn to the maximum value of the most probable relaxation time located near $T = 433$ K, which is close to $T_c = 420$ K of the superionic phase transition.

As noted, the power-law dependence of the conductivity on frequency is a sign of the existence of a hopping mechanism of charge transfer in the studied frequency and temperature ranges. This corresponds to the presence of a wide range of relaxators in the system, which have different relaxation times and provide different dielectric loss mechanisms.

In this regard, we have studied the behavior of the distribution function of relaxators over relaxation times $G(\tau)$. The value of $G(\tau)$ can be obtained, as indicated, from Expression (8) as a result of solving the inverse problem.

Fig. 5 shows the temperature dependence of the maximum value of the function $G(\tau)_{\max}$, which has a maximum height at a temperature $T = 425$ K. This temperature is also close to the temperature of the superionic phase transition (PT).

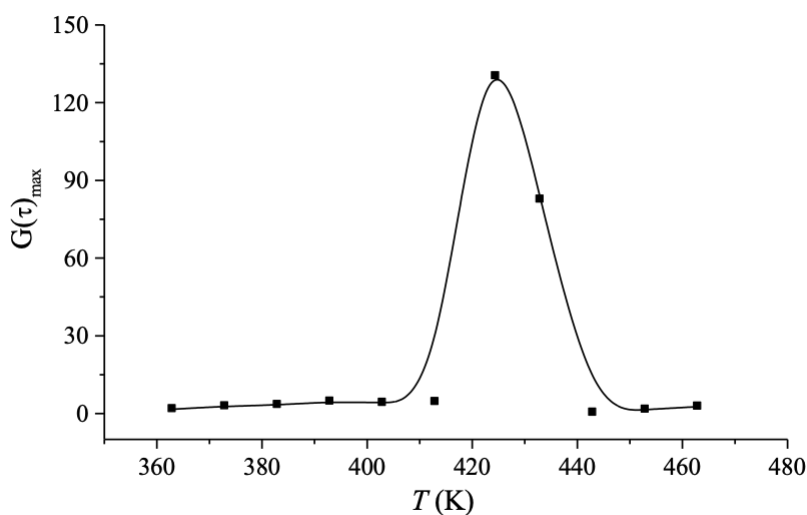


Fig. 5. Temperature dependence of the maximum value of the relaxation time distribution function $G(\tau)_{\max}$ for AgI films

Discussion: A Phenomenological model

The behavior of silver iodide AgI during the thermal phase transition from a semiconductor to a superionic state can be explained by the phenomenological concepts described below.

During the synthesis, the iodination of the metallic silver layer was carried out from the surface of the grains. Therefore, all grains turned out to be covered with a thin layer of crystalline iodine, which has a conductivity an order of magnitude lower than the conductivity of AgI nanocrystallites in the superionic state.

The iodine film played the role of a blocking electrode for the contacts deposited to study the frequency dependence of electrical conductivity in plane geometry. We point out that in the semiconductor state the conductivity of AgI is purely electronic.

When a thermal phase transition to the superionic state occurs as the temperature increases, individual AgI crystallites pass into the state of a superionic conductor at different temperatures. This is due to the martensitic nature of the transition. That is, the deviation from the phase equilibrium temperature necessary for the completion of the phase transition (PT) differs for different grains (Elliott 1987; Kobayashi et al. 2004; Long 1982; Popova et al. 2005).

These differences arise due to the variation in the sizes of crystallites, which are distributed, as shown by AFM studies, in a wide range of values (Popova et al. 2005).

In addition, the amount of deviation required to complete the transition is affected by the elastic energy of adhesion of AgI crystallites to the substrate, the value of which also depends on the size of the crystallites, i. e., on the contact area of the grain with the substrate.

The combination of the described factors leads to a thermal increase in the conductivity of the entire mass of nanocrystallites composing the film according to the percolation law, which is well studied for the case of dc conduction (Farid et al. 2005).

In this case, the single-layer arrangement of grains on the substrate surface corresponds to the simplest case of two-dimensional percolation, if each grain has a conductive contact with only four nearest neighbors. This is indicated by AFM studies. For two-dimensional percolation, it is also necessary that all the grains of the film undergo the same jump in conductivity during the phase transformation. This takes place in the first approximation in the AgI film.

From what has been said, it follows that even in the simplest case of two-dimensional percolation, two phase transitions take place, one of which is a transition in each grain from a low-conducting semiconductor to a high-conducting superionic state.

Another, purely geometric, phase transition is a jump-like transition of the entire mass of film grains to a highly conductive state during the formation of an infinite percolation cluster and is designated as a percolation phase transition.

In AgI, the described case is the case of a square percolation grating with the number of measurements equal to half the number of contacts of each grain (Ivanskoi 2008). This situation is similarly well known for superionic conductors.

It is known (Barman et al. 1995) that in the case of silver sulfide, the primary process that initiates the phase transition to the superionic state is down to two factors: the interaction between the vacancies of Ag⁺ ions and the interaction of the “interstitial silver ion–vacancy” dipoles, which reduce the energy of the ion exit from nanocrystal silver. This is further facilitated by the high Laplacian pressure produced by the high surface tension of the nanocrystals.

A similar situation occurs in silver iodide films, where mobile silver ions can occupy several different positions in the unit cell with different probabilities. They are able to migrate between these positions, that is, move along the conductive channels of the crystal lattice, as described in the introduction.

On the whole, the motion of silver ions in a superionic crystal is complex and combines phonon oscillations of ions at potential energy minima and diffusion hops of silver ions from one equilibrium position to another during hopping conduction (Ivanov-Shits 2007).

A change in the crystal structure of the material as a result of the breaking of chemical bonds during superionic (PT) leads to a change, in addition to the ionic, in the electronic structure of the material and is accompanied by an abrupt change in the electronic part of the conductance (PT) (Barman et al. 1995).

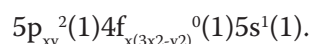
Micromechanism of superionic phase transition in AgI

Silver iodide exists in three different crystalline phases.

At room temperature, the dominant phase is γ -AgI with a zinc blende structure (face-centered cubic structure of F43m symmetry), although 2% of β -AgI with a hexagonal wurtzite structure of P63mc symmetry is present. β -AgI becomes a stable phase above 384 K (111 °C).

Both phases transform into a body-centered cubic α -AgI phase at 420 K (147 °C), which is stable above this temperature and is a superionic phase. Alpha silver iodide is only stable above 147 °C and enters the beta phase when cooled to room temperature.

Hybridization of iodine (I) in the β -AgI lattice is (sp^f):



All three orbitals are located almost in the same plane of the hexagon with a slight bend in the bonds (Pauling 1974) (see Fig. 6). Each hybrid orbital contains one electron.

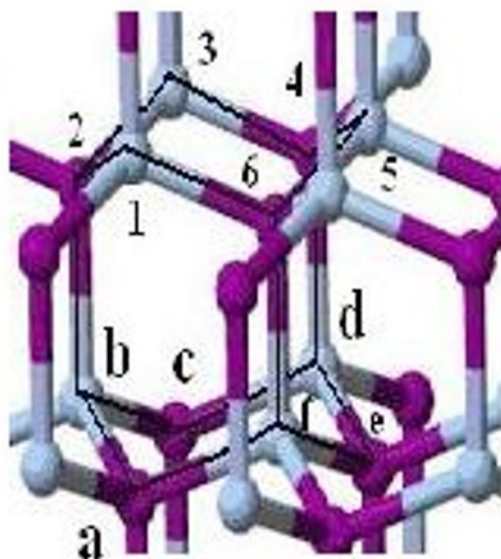


Fig. 6. Fragment of the crystal structure of β -AgI (Binner et al. 2006)

These hybrid orbitals of the Ag and I atoms, containing one electron each, form stable sigma bonds between themselves in the hexagon plane (Fig. 6).

In addition, each iodine (I) atom has two p-orbitals not involved in hybridization: $5p_y^2 5p_z^2$, each of which contains two electrons. Therefore, two of the three bonds of each atom (Ag and I) in the hexagon plane are double: along with the usual sigma bonds 2 p-orbitals $5p_y^2 5p_z^2$ of the I atom not used in hybridization form 2 coordination π -bonds with empty f -orbitals of the Ag atom. This additionally strengthens the bonds of the Ag and I atoms in the hexagon plane (bonds 1–2, 2–3, 3–4, 4–5, and 5–6 in Fig. 6).

The connection of the hexagon planes with each other is carried out due to the coordination sigma bonds between the $4d_{z^2}^2$ orbitals of the Ag atom, containing two electrons each, and the empty $4f_{z^3}^0$ orbitals of the I atom (bonds 2-b, 4-d, and 6-f in Fig. 6). Recall that the energy of coordination bonds is an order of magnitude less than the energy of double bonds 1–2, 2–3, 3–4, 4–5 and 5–6 (Davydov 1973).

It follows from this that the coordination bonds connecting the planes of hexagons are destroyed first of all with an increase in temperature near the point of the superionic phase transition. This leads to a rearrangement of the crystal structure from a hexagonal to a body-centered cubic structure (β -AgI goes over α -AgI).

The body-centered crystal structure that appears above $T_c = 147^\circ\text{C}$ (420 K) after superionic PT has been made retains its integrity due to the usual sigma bonds between iodine ions and silver ions. Each ion is located in the center of a cube made up of ions of the sign opposite to the given ion. The hybrid orbitals needed to create 8 sigma bonds with 16 electrons on them are formed like this. The Ag atom donates 8 $4f^0(7)5s^1$ orbitals for hybridization with one electron on them. Atom I donates 8 orbitals for hybridization $4d_{xy}^2 4d_{xz}^2 4d_{yz}^2 4d_{x^2-y^2}^2 5s^2 5p_x^1 5p_y^2 5p_z^2$ with 15 electrons on them. In total, we have 8 bonds with 16 electrons.

It should be said that, according to the theory, with such a large number of orbitals used in hybridization which inevitably differ in energy, a full-fledged hybridization process is hardly possible (Murrell et al. 1965).

So, most likely, 7 out of 8 bonds are low-energy coordination (donor-acceptor) bonds between the d-orbitals of the Ag^+ ion, containing two electrons each, and the empty f -orbitals of the I- ion. The exceptions are a full-fledged sigma bond between $5p_x^1$, the orbital of the I atom, and $5s^1$, the orbital of the Ag atom.

The presence of low-energy coordination bonds provides a low energy barrier between the positions of ions of adjacent crystal cells. This contributes to the emergence of high mobility in Ag^+ ions in com-

parison with the mobility of I^- , i. e., it provides an effective hopping mechanism of ionic conduction and forms the superionic properties of the material.

The ionic radius of silver ions (0.074 nm) is significantly smaller than that of iodine ions, 0.137 nm, which creates an additional advantage of the drift of metallic Ag^+ ions along the lattice when an external electric field is applied. The drift is carried out along the corresponding ion-conducting channels, as described in the Introduction.

Conclusion

Thus, in this work, the dielectric spectra of thin films of iodized silver AgI have been studied. Dielectric spectroscopy methods have shown that a thermal phase transition from a semiconductor to a superionic state occurs in AgI films at 420 K (147 °C).

The abrupt change of parameters at the transition point is demonstrated by:

- activation energy of semiconductor conduction and commit phases;
- indicator of the degree of frequency dependence of conductivity;
- parameters of the Havriliak-Negami function,
- numerical values of the frequency position and the maximum value of the function of the tangent of the dielectric loss angle.

A model of the micro-mechanism of the thermal phase transition from a semiconductor to a superionic state is proposed.

It is shown that, along with the superionic phase transition, films undergo a percolation phase transition with the formation of a two-dimensional percolation cluster.

Conflict of interest

The authors declare that there is no conflict of interest, either existing or potential.

Author contributions

The authors have made an equal contribution to the preparation of the text.

References

- Amrani, B., Ahmed, R., El Haj Hassan, F., Reshak, A. H. (2008) Structural, electronic and optical properties of AgI under pressure. *Physics Letters A*, 372 (14), 2502–2508. <https://doi.org/10.1016/j.physleta.2007.12.004> (In English)
- Barman, S. R., Shanthi, N., Shukla, A. K., Sama, D. D. (1995) Order-disorder and electronic transitions in $Ag_{2+\sigma}S$ single crystals, studied by photoemission spectroscopy. *Physical Review B*, 53 (7), 3746–3751. <https://doi.org/10.1103/physrevb.53.3746> (In English)
- Binner, J. G. P., Dimitrakis, G., Price, D. M. et al. (2006) Hysteresis in the β – α phase transition in silver iodide. *Journal of Thermal Analysis and Calorimetry*. 84 (2), 409–412. <https://doi.org/10.1007/s10973-005-7154-1> (In English)
- Castro-Arata, R. A., Grabko, G. I., Kononov, A. A. et al. (2021) Perenos zaryada v tonkikh sloyakh stekloobraznoj gibridnoj sistemy $Ge_{28.5}Pb_{14.5}Fe_{0.5}S_{56.5}$ [Charge transfer in thin layers of glassy $Ge_{28.5}Pb_{14.5}Fe_{0.5}S_{56.5}$]. *Fizika i tekhnika poluprovodnikov*, 55 (5), 450–454. <https://doi.org/10.21883/FTP.2021.05.50836.9578> (In Russian)
- Davydov, A. S. (1973) *Kvantovaya mekhanika [Quantum mechanics]*. Moscow: Nauka Publ., 704 p. (In Russian)
- Elliott, S. R. (1987) A.c. conduction in amorphous chalcogenide and pnictide semiconductors. *Advances in Physics*, 36 (2), 135–217. <https://doi.org/10.1080/00018738700101971> (In English)
- Farid, A. M., Atyia, H. E., Hegab, N. A. (2005) AC conductivity and dielectric properties of Sb_2Te_3 thin films. *Vacuum*, 80 (4), 284–294. <https://doi.org/10.1016/j.vacuum.2005.05.003> (In English)
- Fokina, S. V., Borisov, E. N., Tomaev, V. et al. (2016) AgI thin films prepared by laser ablation. *Solid State Ionics*, 297, 64–67. <https://doi.org/10.1016/j.ssi.2016.10.004> (In English)
- Gurevich, Yu. Ya., Kharkats, Yu. I. (1987) Superionnaya provodimost' tverdykh tel [Superionic conductivity of solids]. In: *Itogi nauki i tekhniki. VINITI. Seriya: Khimiya tverdogo tela [Results of science and technology. VINITI. Series: Solid state chemistry]*. Moscow: VINITI Publ., pp. 3–156. (In Russian)

- Ivanov-Shits, A. K. (2007) Computer simulation of superionic conductors: II. Cationic conductors. Review. *Physical Properties of Crystals*, 52 (2), 302–315. <https://doi.org/10.1134/S1063774507020241> (In English)
- Ivanov-Shits, A. K., Murin, I. V. (2000) *Ionika tverdogo tela [Solid State Ionics]*. Saint Petersburg: Saint Petersburg State University Publ., 616 p. (In Russian)
- Ivanskoi, V. A. (2008) Approaches of the percolation theory and the free energy of dislocation clusters. *Technical Physics*, 53 (4), 455–461. <https://doi.org/10.1134/S1063784208040105> (In English)
- Johan, M. R., Tay, S. L., Hawari, N. L., Suan, S. (2011) Phase transition and complex impedance studies of mechano-chemically synthesized AgI-CuI solid solutions *International Journal of Electrochemical Science*, 6, 6235–6243. (In English)
- Kobayashi, M., Ono, S., Tomoyose, T. (2004) Electronic structure and covalency in superionic conductors. *Ionics*, 10 (5–6), 415–420 <https://doi.org/10.1007/BF02378002> (In English)
- Kremer, K., Schonhals, A. (2003) *Broadband dielectric spectroscopy*. Berlin: Springer Publ., 729 p. (In English)
- Long, A. R. (1982). Frequency-dependent loss in amorphous semiconductors. *Advances in Physics*, 31 (5), 553–637. <https://doi.org/10.1080/00018738200101418> (In English)
- Makiura, R., Yonemura, T., Yamada, T. et al. (2009) Size-controlled stabilization of the superionic phase to room temperature in polymer-coated AgI nanoparticles. *Nature Materials*, 8 (6), 476–480. <https://doi.org/10.1038/nmat2449> (In English)
- Mott, N., Davis, E. (1982) *Elektronnyye protsessy v nekrystallicheskih veshchestvakh [Electronic processes in non-crystalline substances]*. 2nd ed. Moscow: Mir Publ., 368 p. (In Russian)
- Murrell, J. N., Kettle, S. F. A., Tedder, J. M. (1965) *Valence theory*. London: John Wiley & Sons Publ., 520 p. (In English)
- Naik, S., Rabinal, M. H. K. (2022) Significance of electrode contact area on memristive parameters of silver iodide. *Materials Science in Semiconductor Processing*, 138, article 106309. <http://dx.doi.org/10.1016/j.mssp.2021.106309> (In English)
- Pauling, L. (1974) *Obshchaya khimiya [General chemistry]*. M.: Mir Publ., 846 p. (In Russian)
- Popova, I. O., Khanin, S. D., Shadrin, E. B. (2005) Sovremennye predstavleniya o fizike fazovogo perekhoda metall-provodnik v oksidakh i khalkogenidakh perekhodnykh metallov i vozmozhnostyakh ego primeneniya [Modern ideas about the physics of the metal-conductor phase transition in transition metal oxides and chalcogenides and the possibilities of its application]. *Izvestia Rossijskogo gosudarstvennogo pedagogicheskogo universiteta im. A. I. Gertsena — Izvestia: Herzen University Journal of Humanities & Sciences*, 5 (13), 128–136. (In Russian)
- Sidorov, A. I., Nashchekin, A. V., Castro, R. A. et al. (2021) Optical and dielectric properties of nanocomposites on base nanoporous glasses with silver and silver iodide nanowires. *Physica B: Condensed Matter*, 603, article 412764. <https://doi.org/10.1016/j.physb.2020.412764> (In English)
- Ulutas, K., Deger, D., Yakut, S. (2013) Thickness dependence of the dielectric properties of thermally evaporated Sb₂Te₃ thin films. *Journal of Physics: Conference Series*, 417 (1), article 012040. <https://doi.org/10.1088/1742-6596/417/1/012040> (In English)
- Vergent'eva, T. Yu., Koroleva, E. Yu., Kurdyukov, D. A. et al. (2013) Behavior of the low-frequency conductivity of silver iodide nanocomposites in the superionic phase transition region. *Physics of the Solid State*, 55 (1), 175–180. <https://doi.org/10.1134/S1063783413010320> (In English)
- Volkov, A. S., Kuposov, G. D., Perfiliev, R. O. (2018) On the Physical meaning of disperse parameters of frequency dependence of dielectric permittivity in the Havriliak–Negami model. *Optics and Spectroscopy*, 125 (3), 379–382. <https://doi.org/10.1134/S0030400X18090242> (In English)
- Wright, A. E., Fender, B. E. F. (1977) The structure of superionic compounds by powder neutron diffraction. I. Cation distribution in α -AgI. *Journal of Physics C: Solid State Physics*, 10 (13), article 2261. <https://doi.org/10.1088/0022-3719/10/13/003> (In English)

Физика конденсированного состояния

ПОЛОЖЕНИЯ ЭКСТРЕМУМОВ ЗОННОГО СПЕКТРА НОСИТЕЛЕЙ ЗАРЯДА В ТОНКИХ ПЛЕНКАХ ВИСМУТА

Демидов Евгений Владимирович

Аннотация. Во многих работах наблюдается рост концентрации носителей заряда в тонких пленках висмута при уменьшении их толщины при низких температурах, получаемый на основе данных об удельном сопротивлении, магнетосопротивлении, коэффициенте Холла и термоЭДС, измеренных в данных пленках. Расчет чаще всего ведется в рамках двузонного приближения в предположении квадратичности закона дисперсии электронов и дырок. Используя данные приближения на основании значений концентрации носителей заряда, можно оценить изменение положения энергетических экстремумов относительно химпотенциала в данных пленках. Данная работа посвящена проведению указанных расчетов и анализу движения экстремумов зонного спектра носителей заряда в пленках висмута при изменении их толщины.

Ключевые слова: тонкие пленки, висмут, явления переноса, концентрация носителей заряда, зонная структура

Для цитирования: Demidov, E. V. (2022) Extrema positions of charge carrier band spectrum in thin bismuth films. *Physics of Complex Systems*, 3 (4), 154–158. <https://www.doi.org/10.33910/2687-153X-2022-3-4-154-158> EDN HZBMJW

МЕХАНИЧЕСКИЕ НАПРЯЖЕНИЯ В ТОНКИХ ПЛЕНКАХ ЦИРКОНАТА-ТИТАНАТА СВИНЦА, СФОРМИРОВАННЫХ НА ПОДЛОЖКАХ, ОТЛИЧАЮЩИХСЯ ТЕМПЕРАТУРНЫМИ КОЭФФИЦИЕНТАМИ ЛИНЕЙНОГО РАСШИРЕНИЯ

Валеева Алсу Равилевна, Каптелов Евгений Юрьевич, Пронин Игорь Петрович, Сенкевич Станислав Викторович, Пронин Владимир Петрович

Аннотация. Рассмотрено влияние линейных и изгибных напряжений на величину внутреннего поля и самополяризации в тонких пленках цирконата-титаната свинца (PZT), сформированных методом высокочастотного магнетронного распыления на подложках кремния и ситалла СТ-50. Состав тонких пленок соответствовал области морфотропной фазовой границы. Предположено, что изгибные напряжения в биморфных структурах «тонкая пленка PZT — подложка» приводят к появлению внутреннего электрического поля, вызванного диффузией заряженных кислородных вакансий (эффект Горского в сегнетоэлектриках).

Ключевые слова: тонкие сегнетоэлектрические пленки, цирконат-титанат свинца, морфотропная фазовая граница, механические напряжения, внутреннее электрическое поле, самополяризация, эффект Горского

Для цитирования: Valeeva, A. R., Kaptelov, E. Yu., Pronin, I. P., Senkevich, S. V., Pronin, V. P. (2022) Mechanical stresses in lead zirconate titanate thin films formed on substrates differing in temperature coefficients of linear expansion. *Physics of Complex Systems*, 3 (4), 159–166. <https://www.doi.org/10.33910/2687-153X-2022-3-4-159-166> EDN IWJDKZ

Теоретическая физика

УПРОЩЕННЫЕ ПРЕДСТАВЛЕНИЯ ВЕРОЯТНОСТЕЙ ИЗЛУЧЕНИЯ ФОТОНА В ПОСТОЯННОМ ВНЕШНЕМ ЭЛЕКТРИЧЕСКОМ ПОЛЕ

Гаврилов Сергей Петрович

Аннотация. В случае сильного внешнего электрического поля существует множество дополнительных каналов процессов, связанных с нарушением стабильности вакуума. Показано, что в зависимости от постановки задачи существует ряд интегральных представлений для вероятностей испускания фотона под действием сильного постоянного электрического поля. Эти представления имеют вид преобразования Фурье от произведения двух веберовских функций параболического цилиндра, являющихся решениями одного и того же дифференциального

уравнения. Для упрощения изучения вероятностей такой природы мы выразили это преобразование Фурье через вырожденную гипергеометрическую функцию.

Ключевые слова: излучение фотона, квантовая электродинамика, сильное внешнее поле, эффект Швингера, преобразование Фурье

Для цитирования: Gavrilov, S. P. (2022) Reduced integral representations for the probabilities of photon emission in a constant external electric field. *Physics of Complex Systems*, 3 (4), 167–175. <https://www.doi.org/10.33910/2687-153X-2022-3-4-167-175> EDN [ORISSK](https://orcid.org/0000-0001-9148-4444)

ЭНТРОПИЯ И РАЗМЕРНОСТЬ ХАОТИЧЕСКОГО АТТРАКТОРА В ЗАВИСИМОСТИ ОТ УПРАВЛЯЮЩИХ ПАРАМЕТРОВ

Ляпцев Александр Викторович

Аннотация. Методом численного эксперимента исследуется зависимость энтропии и размерности хаотического аттрактора от управляющего параметра. Вычисления проводятся для одной из простейших систем, описываемой нелинейными уравнениями динамики, — ротатора, находящегося под воздействием внешнего периодического поля. Особенностью данной системы является чередование регулярных и хаотических решений при изменении управляющего параметра. Численный эксперимент показывает, что при значениях управляющего параметра в диапазонах, где происходит переход от хаотического движения к регулярному движению вследствие перемежаемости, размерность хаотического аттрактора и, как следствие, его энтропия существенно изменяются.

Ключевые слова: нелинейная динамика, странный аттрактор, хаотический аттрактор, плотность вероятности, хаос, прерывистость, вращатель

Для цитирования: Liaptsev, A. V. (2022) Entropy and dimension of a chaotic attractor depending on the control parameter. *Physics of Complex Systems*, 3 (4), 176–185. <https://www.doi.org/10.33910/2687-153X-2022-3-4-176-185> EDN [JFBHQD](https://orcid.org/0000-0001-9148-4444)

ОБ АТМОСФЕРНОЙ РЕАЛИЗАЦИИ КВАНТОВОГО АЛГОРИТМА СВЕРХПЛОТНОГО КОДИРОВАНИЯ

Тимченко Богдан Александрович, Фалеева Мария Петровна, Гилев Павел Андреевич, Блинова Ирина Владимировна, Попов Игорь Юрьевич

Аннотация. Рассмотрены свойства квантового канала связи в свободном пространстве на примере алгоритма сверхплотного кодирования. Изучена теоретическая модель установки, реализующей данный алгоритм, и выявлены основные факторы, влияющие на качество модели. Это коэффициент пропускания атмосферы, эффективность детекторов и среднее значение числа шумовых отсчетов, вызванных фоновым излучением и темновыми отсчетами. Проведен полный расчет модели установки с получением результатов в явном виде. Эти результаты были проанализированы с использованием реалистичных параметров детекторов и атмосферы. Установлено, что наибольшее влияние на результаты оказывают нестабильность атмосферной турбулентности, эффективность детекторов и среднее значение шумовых отсчетов.

Ключевые слова: квантовый канал, плотное кодирование, перепутанность, атмосфера, модель

Для цитирования: Timchenko, B. A., Faleeva, M. P., Gilev, P. A., Blinova, I. V., Popov, I. Yu. (2022) Atmospheric implementation of superdense coding quantum algorithm. *Physics of Complex Systems*, 3 (4), 186–201. <https://www.doi.org/10.33910/2687-153X-2022-3-4-186-201> EDN [KZISPS](https://orcid.org/0000-0001-9148-4444)

Физика полупроводников

ПОЛЯРИЗАЦИОННЫЕ ПРОЦЕССЫ В ПЛЕНКАХ ЙОДИДА СЕРЕБРА ВБЛИЗИ ТЕМПЕРАТУРЫ СУПЕРИОННОГО ФАЗОВОГО ПЕРЕХОДА

Ильинский Александр Валентинович, Шадрин Евгений Борисович, Кастро Арата Рене Александро, Попова Ирина Олеговна

Аннотация. В работе методом диэлектрической спектроскопии изучены особенности поляризационных процессов в нанокристаллических пленках йодида серебра в области термического суперионного фазового перехода и рассчитаны релаксационные и энергетические параметры данной системы. Скачкообразное изменение обнаружено для энергии активации, показателя

степени частотной зависимости, функции тангенса угла диэлектрических потерь. Предложена модель микромеханизма термического фазового перехода «полупроводник — суперионник». Показано, что наряду с суперионным фазовым переходом в пленках имеет место перколяционный фазовый переход с образованием двумерного перколяционного кластера.

Ключевые слова: суперионный фазовый переход, йодид серебра, диэлектрическая спектроскопия, поляризационные процессы, релаксационные процессы

Для цитирования: Ilinskiy, A. V., Shadrin, E. B., Castro Arata, R. A., Popova, I. O. (2022) Polarization processes in silver iodide films near the superionic phase transition temperature. *Physics of Complex Systems*, 3 (4), 202–213. <https://www.doi.org/10.33910/2687-153X-2022-3-4-202-213> EDN XIVVYW